Monthly Notices
of the
ROYAL ASTRONOMICAL SOCIETY

MNRAS **473,** 3454–3489 (2018)
Advance Access publication 2017 September 28

doi:10.1093/mnras/stx2541

Filament formation in wind–cloud interactions– II. Clouds with turbulent density, velocity, and magnetic fields

W. E. Banda-Barragán,[1,2,3]★ C. Federrath,[1] R. M. Crocker[1] and G. V. Bicknell[1]

[1]*Research School of Astronomy and Astrophysics, Australian National University, Canberra, ACT 2611, Australia*
[2]*Observatorio Astronómico de Quito, Escuela Politécnica Nacional, Av. Gran Colombia S/N, Quito 170403, Ecuador*
[3]*Facultad de Ingeniería Civil y Mecánica, Universidad Técnica de Ambato, Av. Los Chasquis y Río Payamino S/N, Ambato 180206, Ecuador*

Accepted 2017 September 26. Received 2017 September 25; in original form 2017 June 13

ABSTRACT

We present a set of numerical experiments designed to systematically investigate how turbulence and magnetic fields influence the morphology, energetics, and dynamics of filaments produced in wind–cloud interactions. We cover 3D, magnetohydrodynamic systems of supersonic winds impacting clouds with turbulent density, velocity, and magnetic fields. We find that lognormal density distributions aid shock propagation through clouds, increasing their velocity dispersion and producing filaments with expanded cross-sections and highly magnetized knots and subfilaments. In self-consistently turbulent scenarios, the ratio of filament to initial cloud magnetic energy densities is ∼1. The effect of Gaussian velocity fields is bound to the turbulence Mach number: Supersonic velocities trigger a rapid cloud expansion; subsonic velocities only have a minor impact. The role of turbulent magnetic fields depends on their tension and is similar to the effect of radiative losses: the stronger the magnetic field or the softer the gas equation of state, the greater the magnetic shielding at wind–filament interfaces and the suppression of Kelvin–Helmholtz instabilities. Overall, we show that including turbulence and magnetic fields is crucial to understanding cold gas entrainment in multiphase winds. While cloud porosity and supersonic turbulence enhance the acceleration of clouds, magnetic shielding protects them from ablation and causes Rayleigh–Taylor-driven subfilamentation. Wind-swept clouds in turbulent models reach distances ∼15–20 times their core radius and acquire bulk speeds ∼0.3–0.4 of the wind speed in one cloud-crushing time, which are three times larger than in non-turbulent models. In all simulations, the ratio of turbulent magnetic to kinetic energy densities asymptotes at ∼0.1–0.4, and convergence of all relevant dynamical properties requires at least 64 cells per cloud radius.

Key words: MHD – turbulence – methods: numerical – ISM: clouds – ISM: magnetic fields – galaxies: starburst.

1 INTRODUCTION

Investigating the dynamics and longevity of wind-swept interstellar clouds is essential to understanding stellar- and supernova-driven, multiphase winds and outflows, as well as the formation and evolution of filaments embedded in them. Wind-swept clouds and filaments have been observed and studied at various scales in the interstellar medium (ISM), such as in the shells of supernova remnants (e.g. see Hester et al. 1996; Koo et al. 2007; Patnaude & Fesen 2009; Shinn et al. 2009; McEntaffer et al. 2013; Nynka et al. 2015 for observations; and Stone & Norman 1992; Melioli, de Gouveia dal Pino & Raga 2005; Melioli et al. 2006; Orlando et al. 2005, 2006, 2008; Leão et al. 2009 for models), in molecular cloud complexes (e.g. see Carlqvist, Gahm & Kristen 2003; Sahai, Morris & Claussen 2012a; Sahai, Güsten & Morris 2012b; Wright et al. 2012; Enokiya et al. 2014; Torii et al. 2014; Benedettini et al. 2015 for observations; and Mellema et al. 2006; Mac Low et al. 2007; Mackey & Lim 2010 for models), in tidally disrupted clouds (e.g. see Gillessen et al. 2012, 2013 for observations; and Burkert et al. 2012; Schartmann et al. 2012, 2015; Ballone et al. 2013, 2016 for models), in the Galactic Centre magnetosphere (e.g. see Yusef-Zadeh, Morris & Chance 1984; Morris & Yusef-Zadeh 1985; Lang et al. 1999; LaRosa et al. 2000, 2004; Yusef-Zadeh, Hewitt & Cotton 2004; Morris, Zhao & Goss 2014 for observations; and Shore & LaRosa 1999; Dahlburg et al. 2002; Sofue, Kigure & Shibata 2005 for models), in large-scale galactic winds, outflows, and fountains (e.g. see Bland & Tully 1988; Shopbell & Bland-Hawthorn 1998; Cecil, Bland-Hawthorn & Veilleux 2002; Crawford et al. 2005; Matsubayashi et al. 2009; McClure-Griffiths

★ E-mail: wlady.bsc@gmail.com

et al. 2012, 2013; Tombesi et al. 2015; Veilleux et al. 2017 for observations; and Strickland & Stevens 2000; Melioli et al. 2008, 2009; Cooper et al. 2008, 2009; Melioli, de Gouveia Dal Pino & Geraissate 2013; Scannapieco 2017 for models), and also in ram-pressure-stripped galaxies (e.g. see Abramson & Kenney 2014; Kenney, Abramson & Bravo-Alfaro 2015 for observations; and Marcolini, Brighenti & D'Ercole 2003; Kronberger et al. 2008; Pfrommer & Dursi 2010; Vijayaraghavan & Ricker 2015 for models).

A crucial question to be answered when studying wind-swept clouds in all the above scenarios is how long a cold and dense cloud is able to survive embedded in a hot and diffuse wind. In particular, if we consider the case of large-scale, multiphase galactic winds, such as the one in the galaxy M82 (e.g. see Strickland, Ponman & Stevens 1997; Lehnert, Heckman & Weaver 1999) or the one in our own Galaxy (e.g. see Sofue & Handa 1984; Bland-Hawthorn & Cohen 2003; Su, Slatyer & Finkbeiner 2010), a key problem is to explain the origin of the populations of high-latitude dense clouds and filaments observed in the star-formation-driven winds of these galaxies (e.g. see Shopbell & Bland-Hawthorn 1998; Greve 2004; Chynoweth et al. 2008 for the wind in M82, and McClure-Griffiths et al. 2012, 2013; Lockman & McClure-Griffiths 2016 for the wind in the Milky Way). Did these structures form at high latitudes as a result of wind gas cooling down to sufficiently low temperatures to trigger radiative instabilities as discussed in Wang (1995), Zhang et al. (2015), and Thompson et al. (2016)? Were these clouds and filaments transported from low to high latitudes by the ram pressure or the radiation pressure of global outflows as discussed in Cooper et al. (2008, 2009); Scannapieco & Brüggen (2015); McCourt et al. (2015); Brüggen & Scannapieco (2016) and in Murray, Quataert & Thompson (2005), Zhang & Thompson (2012), Krumholz & Thompson (2012), and Krumholz & Thompson (2013), respectively? If so, how did these entrained structures survive disruption and ablation to reach latitudes ∼0.4–3 kpc above and below the galactic planes of these galaxies?

As shown in previous numerical studies of shock– and wind–cloud systems, supersonic winds have the ability to disrupt clouds via ram pressure and dynamical instabilities in only a few shock-crossing time-scales (e.g. see Klein, McKee & Colella 1994; Mac Low et al. 1994; Xu & Stone 1995; Jones, Ryu & Tregillis 1996; Gregori et al. 1999, 2000; Fragile et al. 2005; Nakamura et al. 2006; Shin, Stone & Snyder 2008; Pittard et al. 2009; Yirak, Frank & Cunningham 2010; Pittard, Hartquist & Falle 2010; Pittard et al. 2011; Pittard 2011; Johansson & Ziegler 2013; Li, Frank & Blackman 2013; McCourt et al. 2015; Pittard & Parkin 2016; Pittard & Goldsmith 2016; Goldsmith & Pittard 2016; Monceau-Baroux & Keppens 2017). The reader is referred to chapter 2 in Banda-Barragán (2016) for a recent review of the literature on wind–cloud and shock–cloud interactions, and to Goldsmith & Pittard (2017) for a comparative investigation of both processes. In Banda-Barragán et al. (2016) (hereafter Paper I), for instance, we showed that an adiabatic, spherical cloud embedded in a supersonic wind can only reach distances of the order of 3–4 times the cloud's core radius (see fig. 12 in that paper) in one cloud-crushing time, t_{cc}, defined as the time it takes for the initially refracted shock to cross one cloud diameter (see Section 3.4 below for further details). Moreover, previous simulations of shock–cloud interactions showed that the destruction of clouds occurs in only a few cloud-crushing times, typically of the order of $t_{des}/t_{cc} \sim 1.5$–2 in purely adiabatic, hydrodynamic (hereafter HD) models (e.g. see Klein et al. 1994; Poludnenko, Frank & Blackman 2002; Nakamura et al. 2006), or $t_{des}/t_{cc} \sim 4$–6 in models that incorporate radiative cooling (e.g. see Melioli et al. 2005), where the cloud destruction time, t_{des}, is conventionally defined as the time when the mass of the cloud (or of its largest fragment) has dropped by $1/e$ (see section 2.2 of Nakamura et al. 2006). Similarly to radiative cooling, thermal conduction has also been demonstrated to prolong the lifetime of clouds embedded in a hot wind via suppression of dynamical instabilities (e.g. see Orlando et al. 2005; Vieser & Hensler 2007; Orlando et al. 2008; Armillotta et al. 2017).

In all the above cases, however, explaining cloud entrainment has been difficult (e.g. see Zhang et al. 2015; Brüggen & Scannapieco 2016). The modelled wind-swept clouds do survive shredding in scenarios with radiative cooling and thermal conduction to form dense cloudlets and filaments, but their cross-sections become smaller than in purely HD cases as a result of efficient cooling (in radiative clouds) or evaporation (in thermally conducting clouds). Smaller cross-sections mean lower drag forces, so clouds in these models do not reach the high, asymptotic velocities of a few hundred $\mathrm{km\,s^{-1}}$ that are characteristic of the cold phases in multiphase galactic winds (e.g. see Shopbell & Bland-Hawthorn 1998 for M82, and McClure-Griffiths et al. 2013 for our Galaxy). Thus, the nature of high-latitude, dense gas entrained in the aforementioned large-scale, galactic winds is still puzzling from a theoretical point of view (see Chevalier & Clegg 1985; Martin 2005; Veilleux, Cecil & Bland-Hawthorn 2005; McCourt et al. 2016; Krumholz, Kruijssen & Crocker 2017; Heckman & Thompson 2017; Scannapieco 2017 for thorough reviews of galactic winds and/or discussions on wind-launching mechanisms).

Despite this, we show in this paper that two ingredients are key to understanding the prevalence of cold gas in hot winds. The first one is turbulence, previously considered by Cooper et al. (2008, 2009) and Schneider & Robertson (2017), and the second one is magnetic fields, whose importance has been pointed out by Gregori et al. (1999, 2000), Li et al. (2013), McCourt et al. (2015), and Grønnow et al. (2017); and ourselves in Paper I. The results obtained by these studies have been inconclusive so far. On the one hand, the simulations presented by Cooper et al. (2008, 2009) showed that fractal, radiative clouds are fragmented by a global galactic wind to form smaller cloudlets and filaments that acquire velocities of $\sim$100–800 $\mathrm{km\,s^{-1}}$, matching observational measurements of the cold phase velocity in galactic winds and suggesting that entrainment of cloudlets and filaments is actually possible. On the other hand, Schneider & Robertson (2017) found that the entrainment of turbulent clouds is inefficient, owing to the smaller accelerations of their densest cores.

A similar situation occurs in studies with magnetic fields. On the one hand, Li et al. (2013), McCourt et al. (2015), and Grønnow et al. (2017) and ourselves (see Paper I) showed that tangled and transverse (to the direction of streaming) magnetic fields, respectively, effectively suppress Kelvin–Helmholtz (hereafter KH; e.g. see Chandrasekhar 1961; Drazin 1970; Batchelor 2000) instabilities at the sides of wind-swept clouds (via a magnetic shielding effect), thus reducing mixing and prolonging the lifetime of wind-swept clouds. On the other hand, Gregori et al. (1999, 2000), Li et al. (2013), and ourselves (see Paper I) showed that transverse magnetic fields also hasten the growth of Rayleigh–Taylor (hereafter RT; e.g. see Sharp 1984; Drazin 2002; Drazin & Reid 2004) instabilities at the leading edge of the cloud (via a magnetic bumper effect), thus contributing to their break up and subfilamentation. The stronger the magnetic field, the more accentuated the aforementioned affects (e.g. see Shin et al. 2008). In addition, Mac Low et al. (1994), Jones et al. (1996), Miniati et al. (1999a), Miniati, Jones & Ryu (1999b), and ourselves (see Paper I) found that aligned (to the direction of streaming) magnetic fields do not have a significant impact on the

cloud dynamics when compared to purely HD models. Despite the seemingly different results mentioned above, they are all complementary and indicate that magnetic fields have different effects on the morphology and dynamics of clouds, depending on their tension and orientation. They also motivate the study presented here with more realistic models for the clouds as most authors, including ourselves, have considered idealized systems with either spherical clouds and uniform or tangled magnetic fields, or turbulent/fractal clouds without magnetic fields. Thus, in this paper, we reconcile the above results by systematically studying the evolution of initially turbulent clouds embedded in supersonic winds and concentrate on studying both qualitatively and quantitatively the morphology, energetics, and dynamics of these clouds and their ensuing filaments. We show that the inclusion of turbulence and magnetic fields in a self-consistent manner is crucial to understanding cold gas entrainment in multiphase winds.

This paper is organized as follows. In Section 2, we explain the significance of our work in the context of the literature on ISM turbulence. In Section 3, we include a description of the numerical methods, initial and boundary conditions, time-scales, and diagnostics, which we employ in our study. In Section 4, we present our results, including an overall description of filament formation as well as comparisons between different initial configurations in non-turbulent and turbulent clouds. We utilize 3D volume renderings and several diagnostics to illustrate the structure, kinematics, and survival of filaments against dynamical instabilities, as well as the evolution, in the magnetotails, of the different components of the energy density. In Section 6, we summarize our findings and conclusions. At the end of the paper, we include several appendices that contain further details on the methods that we follow in this study and a thorough discussion on the effects of numerical resolution and simulation domain size on the diagnostics presented here.

2 RELEVANCE OF THIS STUDY

In this series of papers, we study wind–cloud interactions and their associated filaments with increasing complexity. In Paper I, we investigated the formation of filamentary structures in systems that included spherical clouds with smoothed density profiles and supersonic winds with uniformly distributed magnetic fields. Here, we investigate wind–cloud systems in which the clouds have lognormal density distributions, Gaussian velocity fields, and turbulent magnetic fields. The significance of this study lies in three main points:

(i) We include magnetic fields as they are ubiquitous in the ISM and should therefore be considered in any realistic models of wind/shock-swept clouds;

(ii) We incorporate turbulence within the clouds (i.e. turbulent distributions for the density, velocity, and magnetic fields) as this is also an intrinsic characteristic of ISM clouds;

(iii) We implement, for the first time, points (i) and (ii) in a systematic and self-consistent manner in the initial conditions of our wind–cloud models.

We explain each of these points below and then pose some questions to be answered throughout this paper.

Magnetic fields and turbulence are fundamental elements of the ISM (see Larson 1981; Padoan, Nordlund & Jones 1997; Mac Low & Klessen 2004; Ferrière 2001, 2007, 2011; Elmegreen & Scalo 2004; Scalo & Elmegreen 2004; McKee & Ostriker 2007). First, magnetic fields have a reciprocal relationship with the gas in which they are frozen. Maxwell stresses act upon the magnetized gas changing its dynamics, whilst the resulting motion of the gas affects the topology of the magnetic field lines via shearing and vortical motions (e.g. see Cowling 1976; Miniati et al. 1999b). As a result, enhancement and annihilation of magnetic energy occur in such environments through dynamo action (e.g. see Subramanian 1999; Brandenburg & Subramanian 2005; Federrath et al. 2014), and reconnection events (e.g. see Lazarian & Vishniac 1999; Lazarian 2014), respectively. Second, turbulence also plays an essential role in shaping the ISM and influencing the processes occurring in it, such as star formation (e.g. see Mac Low & Klessen 2004; Santos-Lima et al. 2010; Santos-Lima, de Gouveia Dal Pino & Lazarian 2012; Federrath & Klessen 2012; Kainulainen, Federrath & Henning 2013; Padoan et al. 2014; Leão et al. 2013; Salim, Federrath & Kewley 2015; Krumholz & Kruijssen 2015), dynamo-regulated growth of magnetic fields (e.g. see Schleicher et al. 2013; Santos-Lima et al. 2014; Schober et al. 2015; Bhat, Subramanian & Brandenburg 2016), and acceleration and diffusion of cosmic rays (e.g. see Yan & Lazarian 2002; Weidl et al. 2015).

Furthermore, clouds in the ISM are intrinsically turbulent as they emerge from the non-isotropic condensation of thermally unstable gas (e.g. see Field 1965; Yamada & Nishi 2001; van Loo et al. 2007; van Loo, Falle & Hartquist 2010; Inoue & Inutsuka 2012; Proga & Waters 2015), or from thin shell instabilities in colliding winds (e.g. see Stevens, Blondin & Pollock 1992; Dgani, Walder & Nussbaumer 1993; Vishniac 1994; Parkin et al. 2011; Calderón et al. 2016). Observational and numerical studies of clumpy media show, for example, that the density profiles inside clouds are best described by lognormal distributions in supersonic, transonic, and subsonic scenarios (e.g. see Vazquez-Semadeni 1994; Passot & Vázquez-Semadeni 1998; Nordlund & Padoan 1999; Federrath, Klessen & Schmidt 2008; Kainulainen et al. 2009; Federrath et al. 2010; Kainulainen, Federrath & Henning 2014; Schneider et al. 2012, 2013, 2016). Similarly, velocity fields inside clouds are best represented by Gaussian random distributions (e.g. see Mouri et al. 2002; Ossenkopf & Mac Low 2002; Federrath 2013). Lastly, numerical studies on compressible isothermal turbulence show that the magnetic field perturbations in such environments are well described by monotonic probability distributions (e.g. see Pietarila Graham, Danilovic & Schüssler 2009; Crutcher et al. 2010). Thus, incorporating turbulent clouds constitutes a substantial improvement with respect to previous studies as: (1) the profiles of the density, velocity, and magnetic fields in turbulent clouds are correlated as a result of the coupling between density, velocity, and magnetic field governed by the MHD equations, and (2) the lognormal or Gaussian distributions in turbulent models are skewed and contain higher order moments, which manifests in the so-called intermittency (see Federrath et al. 2010; Hopkins 2013). These two realistic features of turbulence are absent in artificially generated fractal clouds (e.g. see our group's earlier works with fractal clouds in Cooper et al. 2008, 2009) and other non-uniform density profiles (e.g. see Raga, Steffen & González 2005).

Our study here probes the physics of filament formation in 3D, turbulent wind–cloud interactions at high resolution. The aim of this paper is to study the morphology, kinematics, and magnetic properties of the magnetized filaments that arise as a result of wind-swept turbulent clouds. By examining the impact of turbulence on the interplay between winds and clouds, we address the following questions: (1) Are the mechanisms involved in the formation of filaments universal, i.e. the same for uniform and turbulent (non-uniform) clouds? (2) How does the internal structure of filaments change when turbulence is included in the initial conditions? (3) To what distances and velocities are wind-swept turbulent clouds

ram pressure accelerated by the wind? (4) What are the effects of varying the Mach number of turbulent velocity fields? (5) What are the effects of changing the strength of turbulent magnetic fields? (6) What is the ratio of filament magnetic field to initial magnetic field in the cloud? (7) What kind of energy densities are involved? (8) What is the fate of dense gas within turbulent clouds when entrained in the wind?

3 METHOD

3.1 Simulation code

To perform the simulations reported in this paper, we solve the time-dependent equations of ideal magnetohydrodynamics (hereafter MHD). We utilize the PLUTO4.0 code (see Mignone et al. 2007, 2012) in a 3D Cartesian coordinate system (X_1, X_2, X_3) to solve the following equations for mass, momentum, energy conservation, and magnetic induction:

$$\frac{\partial \rho}{\partial t} + \boldsymbol{\nabla \cdot} [\rho \boldsymbol{v}] = 0, \tag{1}$$

$$\frac{\partial [\rho \boldsymbol{v}]}{\partial t} + \boldsymbol{\nabla \cdot} [\rho \boldsymbol{v}\boldsymbol{v} - \boldsymbol{B}\boldsymbol{B} + \boldsymbol{I}\, P] = 0, \tag{2}$$

$$\frac{\partial E}{\partial t} + \boldsymbol{\nabla \cdot} [(E + P)\, \boldsymbol{v} - \boldsymbol{B}\, (\boldsymbol{v} \cdot \boldsymbol{B})] = 0, \tag{3}$$

$$\frac{\partial \boldsymbol{B}}{\partial t} - \boldsymbol{\nabla \times} (\boldsymbol{v} \times \boldsymbol{B}) = 0, \tag{4}$$

where ρ is the mass density, $\boldsymbol{v}$ is the velocity, $\boldsymbol{B}$ is the magnetic field[1], $P = P_{\rm th} + P_{\rm mag}$ is the total pressure (i.e. thermal plus magnetic: $P_{\rm mag} = \frac{1}{2}|\boldsymbol{B}|^2$), $E = \rho\epsilon + \frac{1}{2}\rho \boldsymbol{v}^2 + \frac{1}{2}|\boldsymbol{B}|^2$ is the total energy density, and ϵ is the specific internal energy. We use an ideal equation of state to close the above system of conservation laws:

$$P_{\rm th} = P_{\rm th}(\rho, \epsilon) = (\gamma - 1)\, \rho\epsilon, \tag{5}$$

where we assume a ratio of the specific heat capacities at constant pressure and volume of $\gamma = \frac{5}{3}$ for adiabatic models and $\gamma = 1.1$ for the quasi-isothermal model (which approximates the effects of radiative cooling as in Klein et al. 1994; Nakamura et al. 2006). Using a softer polytropic index is an effective way of investigating the role of radiative cooling in wind–cloud systems, without having to worry about problems with unresolved cooling length-scales (e.g. see Yirak et al. 2010) or 'runaway' cooling effects (e.g. see Mellema, Kurk & Röttgering 2002; Fragile et al. 2004; Johansson & Ziegler 2013). This approach also allows us to keep our results scale-free and provide a thorough qualitative and quantitive analysis of wind-swept clouds in a general MHD context; this can be insightful for current and future work addressing specific wind–/shock–cloud systems and scales (in specific cooling regimes). Similarly to Paper I, we solve three additional advection equations of the form:

$$\frac{\partial [\rho C_\alpha]}{\partial t} + \boldsymbol{\nabla \cdot} [\rho C_\alpha \boldsymbol{v}] = 0, \tag{6}$$

where C_α represents a set of three Lagrangian scalars used to track the evolution of gas initially contained in the cloud as a whole (when α = cloud/filament), in its core (when α = core/footpoint), and in its envelope (when α = envelope/tail). Initially, we define $C_\alpha = 1$ for the whole cloud, the cloud core, and the cloud envelope, respectively, and $C_\alpha = 0$ everywhere else. This configuration allows us to study the evolution of each component of the cloud separately.

In order to solve the above system of hyperbolic conservation laws and to preserve the solenoidal condition, $\boldsymbol{\nabla \cdot B} = 0$, we configure the PLUTO code to use the HLLD approximate Riemann solver of Miyoshi & Kusano (2005) jointly with the constrained-transport upwind scheme of Gardiner & Stone (2005, 2008). The magnetic vector potential $\boldsymbol{A}$, where $\boldsymbol{B} = \boldsymbol{\nabla \times A}$, is used to initialize the field and the Courant–Friedrichs–Lewy number is $C_{\rm a} = 0.3$ in all cases to achieve numerical stability.

3.2 Initial and boundary conditions

In these simulations, we consider a two-phase ISM composed of a single uniform or turbulent cloud (in a spherical volume) surrounded by a hot, tenuous, supersonic wind. Similarly to Paper I (see fig. 1 there), the cloud is initially immersed in a uniform velocity field, i.e. a wind with Mach numbers:

$$\mathcal{M}_{\rm w} = \frac{|\boldsymbol{v}_{\rm w}|}{c_{\rm w}} = 4.0 \,{\rm or}\, 4.9, \tag{7}$$

depending on whether the model is adiabatic or quasi-isothermal, respectively. In equation (7), $|\boldsymbol{v}_{\rm w}| \equiv v_{\rm w}$ and $c_{\rm w} = \sqrt{\gamma \frac{P_{\rm th}}{\rho_{\rm w}}}$ are the speed and sound speed of the wind, respectively, and $\rho_{\rm w}$ is the density of the wind.

We employ Cartesian (X_1, X_2, X_3) coordinates for all the simulations reported here. The simulation domain consists of a rectangular prism that comes in two different configurations: M (standard, medium domain) covering the spatial range $-3\,r_{\rm c} \leq X_1 \leq 3\,r_{\rm c}$, $-2\,r_{\rm c} \leq X_2 \leq 16\,r_{\rm c}$, and $-3\,r_{\rm c} \leq X_3 \leq 3\,r_{\rm c}$, and S (small domain) covering the spatial range $-2\,r_{\rm c} \leq X_1 \leq 2\,r_{\rm c}$, $-2\,r_{\rm c} \leq X_2 \leq 10\,r_{\rm c}$, and $-2\,r_{\rm c} \leq X_3 \leq 2\,r_{\rm c}$, where $r_{\rm c}$ is the radius of the cloud. In the former configuration, M, the uniform grid resolution is $(N_{\rm X_1} \times N_{\rm X_2} \times N_{\rm X_3}) = (384 \times 1152 \times 384)$, so that 64 cells cover the cloud radius (R_{64}) and 32 cells cover the core radius (defined as $r_{\rm co} = 0.5\, r_{\rm c}$). In the latter configuration, S, the uniform grid resolution is $(N_{\rm X_1} \times N_{\rm X_2} \times N_{\rm X_3}) = (512 \times 1536 \times 512)$, so that 128 cells cover the cloud radius (R_{128}) and 64 cells cover the core radius (defined as $r_{\rm co} = 0.5\, r_{\rm c}$). Models with other resolutions ($R_{16\,-\,128}$) and with a larger domain configuration, L, are also described in Appendices A and B, respectively. The cloud is initially centred in the origin (0, 0, 0) of the simulation domain.

We prescribe diode boundary conditions (i.e. gas outflow is allowed while inflow is prevented) on five sides of the simulation domain and an inflow boundary condition (i.e. an injection zone) on the remaining side. A constant supply of wind material is ensured by setting the injection zone at the ghost zone (of the computational domain) that faces the leading edge of the cloud.

For consistency, clouds with either uniform or turbulent profiles are assigned a spherical density distribution that smoothly decreases away from its centre (see Kornreich & Scalo 2000; Nakamura et al. 2006). The function describing the radial density gradient is:

$$\frac{\rho(r)}{\rho_{\rm w}} = 1 + \frac{\chi - 1}{1 + \left(\frac{2r}{r_{\rm c}}\right)^N}, \tag{8}$$

where N is an integer that determines the steepness of the curve (see Fig. 1), and χ represents the density contrast between wind

[1] Note that the factor $\frac{1}{\sqrt{4\pi}}$ is subsumed into the definition of magnetic field. The same normalization applies henceforth.

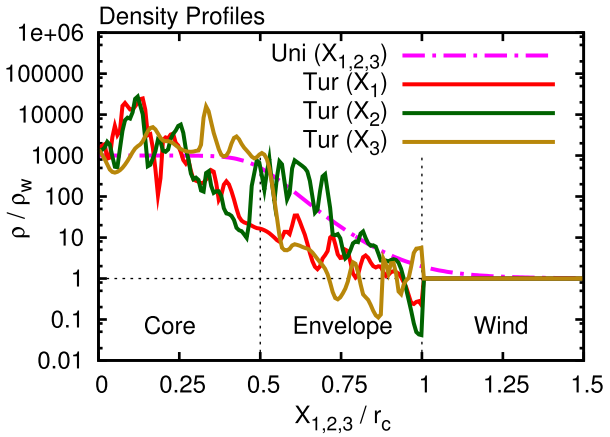

Figure 1. Initial density profiles of a uniform cloud (dash–dotted line) and a turbulent cloud (solid lines) along the X_1, X_2, and X_3 directions. The horizontal axis shows the extent of the cloud core, cloud envelope, and ambient wind material up to $X_{1,2,3}/r_c = 1.5$, and the vertical axis shows the normalized density, ρ/ρ_w, in logarithmic scale.

and cloud material, which is:

$$\chi = \frac{\rho_c}{\rho_w} = 10^3 \tag{9}$$

for all models, where ρ_c is the target density at the centre of the cloud. Since the density profile of equation (8) extends to infinity, we impose a boundary for the cloud by selecting $N = 10$ and a cut-off radius, r_{cut}. In our model with a uniform cloud, we truncate the density function at $r_{cut} = 1.58\,r_c$, at which point $\rho(r_{cut}) = 1.01\,\rho_w$, and we define the boundary of the cloud at $r_{boundary} = 1.0\,r_c$, at which point $\rho(r_c) = 2.0\,\rho_w$. This ensures a smooth transition into the background gas. In our models with turbulent clouds, we define $r_{cut} = r_{boundary} = 1.0\,r_c$ for all configurations. Density gradients, similar to that described by equation (8), are expected in e.g. ISM atomic and molecular clouds, in which dense cores are surrounded by warm, low-density envelopes (e.g. Wolfire, Tielens & Hollenbach 1990; Carral et al. 1994; Higdon, Lingenfelter & Rothschild 2009). All the clouds in our models are in thermal pressure equilibrium with the ambient medium at the beginning of the calculations.

Despite the smooth density transition between cloud and wind material achieved with equation (8), spherically symmetric clouds with uniform densities are only ideal approximations. In reality, we know that ISM clumps are turbulent and have density profiles described by lognormal distributions (e.g. see Padoan & Nordlund 1999; Williams 1999; Warhaft 2000; Heiles 2004; Brunt, Heyer & Mac Low 2009; Price, Federrath & Brunt 2011; Hennebelle & Falgarone 2012; Konstandin et al. 2012; Molina et al. 2012; Federrath & Banerjee 2015; Nolan, Federrath & Sutherland 2015; Schneider et al. 2015 and references in Section 2). Therefore, in order to initialize our simulations with more physical density profiles for the clumps, we take a 256^3-sized data cube from a simulation snapshot of isothermal turbulence (see model 21 in table 2 of Federrath & Klessen 2012), and interpolate its density structure into our simulation domain. The probability density function (hereafter PDF) of the turbulent clouds studied in this paper is presented in Appendix C.

Before proceeding with this interpolation, we first taper the turbulent density profile in the data cube with the function given in equation (8), and mask regions in the cube outside a spherical volume of radius r_c. The ensuing turbulent cloud is then interpolated into our simulation region and placed at the grid origin (0,0,0). As a final step, before initializing the simulations, we scale the mean density of the turbulent cloud in order to match it to the initial mean density of the uniform clouds reported in Paper I and below. As a result, all models start off with clouds of the same initial mass and average density, $[\rho_{cloud}]$. This also means that the density PDF from the source simulation remains the same in our models (except for minor changes introduced in the masking process).

To prescribe the initial turbulent velocity field for the clouds, we use the velocity components from the aforementioned snapshot of model 21 in Federrath & Klessen (2012) and scale the initial velocity dispersion by selecting an rms Mach number:

$$\mathcal{M}_{tu} = \frac{|\boldsymbol{\delta v}_{cloud}|}{c_{cloud}} = 7.2,\ 8.9,\ \text{or}\ 0.33, \tag{10}$$

representative of adiabatic, supersonically turbulent clouds; self-consistent[2], quasi-isothermal, supersonically turbulent clouds; or adiabatic, subsonically turbulent clouds, respectively. In equation (10), $|\boldsymbol{\delta v}_{cloud}| \equiv \delta v_{cloud}$ and $c_{cloud} = \sqrt{\gamma \frac{P_{th}}{\rho_c}}$ are the initial velocity dispersion and initial sound speed of the cloud, respectively. The supersonic setups are representative of molecular (e.g. see Larson 1981) or cold, atomic (e.g. see Heiles & Troland 2003) clouds, while the subsonic setups are more appropriate for warm, atomic (e.g. see Saury et al. 2014) or partially ionized (e.g. see Redfield & Linsky 2004; Gaensler et al. 2011) clouds in the ISM.

This study comprises nine models in total, for which we adopt a naming convention WWW-YYY-ZZZ for the models with the M configuration and Www-Yyy-Zzz for the models with the S configuration, such that WWW and Www describe the type of density field (i.e. UNI=Uni=Uniform and TUR=Tur=Turbulent), YYY and Yyy describe the type of turbulent velocity field (i.e. 0=Null, Sub=Subsonic and SUP=Sup=Supersonic), and ZZZ and Zzz describe the type of turbulent magnetic field (i.e. 0=Null, Bwk=Weak $\boldsymbol{B}$ field, and BST=Bst=Strong $\boldsymbol{B}$ field). Our nine models are split into two sets of numerical MHD simulations (see Table 1). The first set has three models that utilize the M configuration mentioned above. Model UNI-0-0 includes a uniform (i.e. non-turbulent) cloud embedded in a uniform magnetic field, while models TUR-SUP-BST and TUR-SUP-BST-ISO (where ISO stands for quasi-isothermal) include turbulent clouds with self-consistent density, velocity, and magnetic field profiles. The second set has six models that utilize the S configuration. Model Uni-0-0 includes a uniform cloud and serves as a comparison between filament formation mechanisms in models with and without turbulence. Model Tur-0-0 is our control run and includes a turbulent cloud with the lognormal density PDF mentioned above (see equation C1 in Appendix C). Models Tur-Sub-0 and Tur-Sup-0 include a turbulent cloud with the same density PDF of model Tur-0-0, plus the Gaussian velocity field mentioned above with subsonic and supersonic Mach numbers, respectively, as described by equation (10).

In five of the models mentioned above (UNI-0-0, Uni-0-0, Tur-0-0, Tur-Sub-0, and Tur-Sup-0), we add an oblique magnetic field, uniformly distributed over the entire simulation domain (similar to our setup in Paper I), using the following equation:

$$\boldsymbol{B} = \boldsymbol{B}_{ob} = \boldsymbol{B}_1 + \boldsymbol{B}_2 + \boldsymbol{B}_3, \tag{11}$$

[2] The Mach number and the density distribution in our supersonically turbulent simulations are self-consistent, i.e. they are consistent with the relation between the density standard deviation (σ), the turbulence forcing parameter b, and the rms Mach number, namely $\sigma = b\mathcal{M}_{tu}$, (e.g. see Federrath & Klessen 2012). This is not the case for the subsonic cases as we keep the density distribution the same, but scale the Mach number down. We will explore the correct scaling for such models in future work.

Table 1. Simulation parameters for different MHD models. In column 1, we provide the model names. In columns 2 and 3, we indicate the computational domain configurations (i.e. model identifiers or IDs and sizes) and resolutions, respectively. Note that the model identifiers (M1–3 and S4–9) are also used in the panels with the 3D renderings presented in Section 4. In column 4, we describe the type of density profile that is initialized in each cloud model. In columns 5–7, we provide the polytropic index, the Mach number of the wind, and the wind–cloud density contrast, respectively. In columns 8 and 9, we provide details on the configuration and sonic Mach number, respectively, of the initial velocity field in the clouds. In columns 10–12, we describe the initial topology, the plasma beta of the uniform component, and the mean plasma beta of the turbulent component, respectively, of the initial magnetic field in the cloud. The magnetic field in the wind is uniform (with an oblique topology) and has a plasma beta of $\beta_{ob} = 100$ in all cases.

(1) Model	(2) ID & Domain	(3) Resolution	(4) Density field	(5) γ	(6) $\mathcal{M}_w$	(7) χ	(8) Velocity field	(9) $\mathcal{M}_{tu}$	(10) Magnetic field	(11) β_{ob}	(12) $[\beta_{tu}]$
UNI-0-0	M1 $\equiv (6 \times 18 \times 6)\, r_c$	R_{64}	Uniform	1.667	4	10^3	Null	–	Uniform Oblique	100	–
TUR-SUP-BST	M2 $\equiv (6 \times 18 \times 6)\, r_c$	R_{64}	Turbulent	1.667	4	10^3	Turbulent	7.2	Oblique + Turbulent	100	0.04
TUR-SUP-BST-ISO	M3 $\equiv (6 \times 18 \times 6)\, r_c$	R_{64}	Turbulent	1.100	4.9	10^3	Turbulent	8.9	Oblique + Turbulent	100	0.04
Uni-0-0	S4 $\equiv (4 \times 12 \times 4)\, r_c$	R_{128}	Uniform	1.667	4	10^3	Null	–	Uniform Oblique	100	–
Tur-0-0	S5 $\equiv (4 \times 12 \times 4)\, r_c$	R_{128}	Turbulent	1.667	4	10^3	Null	–	Uniform Oblique	100	–
Tur-Sub-0	S6 $\equiv (4 \times 12 \times 4)\, r_c$	R_{128}	Turbulent	1.667	4	10^3	Turbulent	0.33	Uniform Oblique	100	–
Tur-Sup-0	S7 $\equiv (4 \times 12 \times 4)\, r_c$	R_{128}	Turbulent	1.667	4	10^3	Turbulent	8.9	Uniform Oblique	100	–
Tur-Sub-Bwk	S8 $\equiv (4 \times 12 \times 4)\, r_c$	R_{128}	Turbulent	1.667	4	10^3	Turbulent	0.33	Oblique + Turbulent	100	4
Tur-Sub-Bst	S9 $\equiv (4 \times 12 \times 4)\, r_c$	R_{128}	Turbulent	1.667	4	10^3	Turbulent	0.33	Oblique + Turbulent	100	0.04

in which the 3D magnetic field has components along X_1, X_2, and X_3 of identical magnitude:

$$|\boldsymbol{B_1}| = |\boldsymbol{B_2}| = |\boldsymbol{B_3}| = \sqrt{\frac{2P_{th}}{3\beta_{ob}}} \tag{12}$$

where the plasma beta, β_{ob} is a dimensionless number that relates the thermal pressure, P_{th}, to the magnetic pressure in the oblique field, $P_{mag,ob} = \frac{1}{2}|\boldsymbol{B}|^2 = \frac{1}{2}|\boldsymbol{B}_{ob}|^2$, and is given by:

$$\beta_{ob} = \frac{P_{th}}{P_{mag,ob}} = \frac{P_{th}}{\frac{1}{2}|\boldsymbol{B_{ob}}|^2} = 100, \tag{13}$$

in all of our models. In order to isolate the effects of a tangled, turbulent magnetic field on the formation of filaments, models TUR-SUP-BST, TUR-SUP-BST-ISO, Tur-Sub-Bwk, and Tur-Sub-Bst include turbulent clouds with the density PDF and Gaussian velocity fields (with supersonic Mach numbers in the first two cases and subsonic Mach numbers in the other two cases), plus a two-component magnetic field given by:

$$\boldsymbol{B} = \boldsymbol{B_{ob}} + \boldsymbol{B_{tu}} = (\boldsymbol{B_1} + \boldsymbol{B_2} + \boldsymbol{B_3}) + \boldsymbol{B_{tu}}, \tag{14}$$

i.e. the total magnetic field in the cloud is the sum of a 3D uniform magnetic field obliquely oriented with respect to the wind direction with components given by equation (12), and a turbulent magnetic field extracted from model 21 of Federrath & Klessen (2012) with a turbulent plasma beta defined by:

$$\beta_{tu} = \frac{P_{th}}{P_{mag,tu}} = \frac{P_{th}}{\frac{1}{2}|\boldsymbol{B_{tu}}|^2} = 0.04; \text{ or } 4, \tag{15}$$

for strong- and weak-field simulations, respectively (the reader is referred to panel C of fig. 7.6 in Banda-Barragán 2016 for a 3D streamline plot of the initial topology of the turbulent magnetic field in the simulation domain). In models TUR-SUP-BST, TUR-SUP-BST-ISO, and Tur-Sub-Bst, the initial turbulent magnetic field is scaled so that its average plasma beta is $[\beta_{tu}] = 0.04$ (i.e. the magnetic field is strong and consistent with the magnetic distribution in the initial turbulence data cube from Federrath & Klessen 2012), while in model Tur-Sub-Bwk, the initial turbulent magnetic field is scaled so that its average plasma beta is $[\beta_{tu}] = 4$ (i.e. the magnetic field is weak).

Note that the initial magnetic field in the wind is $\boldsymbol{B_{ob}}$ in all cases, so if the magnetic fields given in equation (14) were directly interpolated into the simulation grids of models TUR-SUP-BST, TUR-SUP-BST-ISO, Tur-Sub-Bst, and Tur-Sub-Bwk, the solenoidal property would be violated at the boundaries of the clouds (due to truncation). In order to ensure that the initial magnetic fields in these models are solenoidal (i.e. that $\nabla \cdot \boldsymbol{B} = 0$), we clean the divergence errors before initializing these simulations. We follow the hyperbolic, divergence-cleaning algorithm introduced by Dedner et al. (2002) and implemented by Mignone, Tzeferacos & Bodo (2010) to perform this operation (see Appendix D for further details). Once the magnetic fields for models TUR-SUP-BST, TUR-SUP-BST-ISO, Tur-Sub-Bst, and Tur-Sub-Bwk satisfy the divergence-free constraint and have the desired value of $[\beta_{tu}]$, we interpolate them into our simulation domains and update them numerically with the system of equations described in Section 3.1.

3.3 Diagnostics

Similarly to Paper I, we use the following global diagnostics to study the formation and evolution of filaments in our simulations:

(i) The volume-averaged value of a variable $\mathcal{F}$ is denoted by square brackets as follows:

$$[\mathcal{F}_\alpha] = \frac{\int \mathcal{F} C_\alpha \mathrm{d}V}{V_{cl}} = \frac{\int \mathcal{F} C_\alpha \mathrm{d}V}{\int C_\alpha \mathrm{d}V}, \tag{16}$$

where V is the volume, C_α are the advected scalars defined in Section 3.1, and V_{cl} is the total cloud volume. Using equation (16), we define functions describing the average density, $[\rho_\alpha]$; the average plasma beta, $[\beta_\alpha]$; the average magnetic field, $[B_{j,\alpha}]$; and its rms along each axis, $[B^2_{j,\alpha}]^{\frac{1}{2}}$. The subscript j = 1, 2, and 3 specifies the direction along X_1, X_2, and X_3, respectively.

(ii) The mass-weighted volume average of the variable $\mathcal{G}$ is denoted by angle brackets as follows:

$$\langle \mathcal{G}_\alpha \rangle = \frac{\int \mathcal{G}\rho C_\alpha \mathrm{d}V}{M_{cl}} = \frac{\int \mathcal{G}\rho C_\alpha \mathrm{d}V}{\int \rho C_\alpha \mathrm{d}V}, \tag{17}$$

where V and C_α are as defined above, and M_{cl} is the total cloud mass. Using equation (17), we define the average filament/cloud extension, $\langle X_{j,\alpha} \rangle$; its rms along each axis, $\langle X^2_{j,\alpha} \rangle^{\frac{1}{2}}$; the average velocity, $\langle v_{j,\alpha} \rangle$; and its rms along each axis, $\langle v^2_{j,\alpha} \rangle^{\frac{1}{2}}$. In order to retain the scalability of our results, these quantities are normalized with respect to their initial values. Velocity measurements are the

exemption to this as they are normalized with respect to the wind speed, $v_{\rm w}$.

(A)[3] Using the above definitions, we estimate the length-to-width and width-to-width aspect ratio of filaments along j = 2 and 3, respectively, as follows:

$$\xi_{{\rm j},\alpha} = \frac{\iota_{{\rm j},\alpha}}{\iota_{1,\alpha}}, \tag{18}$$

where $\iota_{{\rm j},\,\alpha}$ are the effective radii (see Klein et al. 1994) along each axis (j = 1, 2, and 3):

$$\iota_{{\rm j},\alpha} = \left[5\left(\langle X^2_{{\rm j},\alpha}\rangle - \langle X_{{\rm j},\alpha}\rangle^2\right)\right]^{\frac{1}{2}}. \tag{19}$$

(B, H) From equation (19), we define the lateral width/expansion (along X_1) and the displacement of the centre of mass of filaments (along the streaming axis, X_2) as $\iota_{1,\,\alpha}$ and $\langle X_{2,\,\alpha}\rangle$, respectively.

(C) In a similar way, we define the total (for j = 1, 2, and 3) and transverse (for j = 1 and 3) velocity dispersion as follows:

$$\delta_{{\rm v}_\alpha} \equiv |\boldsymbol{\delta}_{\mathbf{v}_\alpha}| = \sqrt{\sum_{\rm j} \delta^2_{{\rm v}_{{\rm j},\alpha}}}, \tag{20}$$

where the corresponding dispersion of the j-component of the velocity (see Mac Low et al. 1994), $\delta_{{\rm v}_{{\rm j},\alpha}}$, reads

$$\delta_{{\rm v}_{{\rm j},\alpha}} = \left(\langle v^2_{{\rm j},\alpha}\rangle - \langle v_{{\rm j},\alpha}\rangle^2\right)^{\frac{1}{2}}. \tag{21}$$

(I) From equation (21), we define the bulk velocity of filaments as $\langle v_{2,\,\alpha}\rangle$. The temporal behaviour of this parameter is used to study the acceleration of the cloud.

(D) Using equation (16), we also measure the mean vorticity $[\omega_\alpha]$ of the gas in the filaments, where $\omega_\alpha = |\boldsymbol{\omega}_\alpha| = |\boldsymbol{\nabla} \times \boldsymbol{v}_{\boldsymbol{\alpha}}|$, and the averaged value is normalized with respect to its initial value (i.e. $[\omega_{\alpha,\,0}]$).

In order to quantify the kinetic energy densities in filament material, we decompose the total velocity field into mean, $\overline{v_{{\rm j},\alpha}} \equiv \langle v_{{\rm j},\alpha}\rangle$; and turbulent, $v'_{{\rm j},\alpha}$, components, i.e. $\boldsymbol{v}_{\boldsymbol{\alpha}} = \overline{\boldsymbol{v}_{\boldsymbol{\alpha}}} + \boldsymbol{v}'_{\boldsymbol{\alpha}}$ (see Kuncic & Bicknell 2004; Davidson 2004; Parkin 2014 for thorough discussions on statistical averaging in problems involving MHD turbulence). Thus, the corresponding turbulent kinetic energy density reads:

$$E'_{{\rm k},\alpha} = \frac{1}{2}\rho|\boldsymbol{v}'_{\boldsymbol{\alpha}}|^2. \tag{22}$$

(E) Using equation (22), we define the averaged turbulent kinetic energy density of filaments as $[E'_{{\rm k},\alpha}]$.

Similarly, to study the magnetic energy densities in filament material we decompose the total magnetic field into mean, $\overline{B_{{\rm j},\alpha}} \equiv [B_{{\rm j},\alpha}]$; and turbulent, $B'_{{\rm j},\alpha}$ components, i.e. $\boldsymbol{B}_{\boldsymbol{\alpha}} = \overline{\boldsymbol{B}_{\boldsymbol{\alpha}}} + \boldsymbol{B}'_{\boldsymbol{\alpha}}$. Thus, we define the turbulent magnetic energy density,

$$E'_{{\rm m},\alpha} = \frac{1}{2}|\boldsymbol{B}'_{\boldsymbol{\alpha}}|^2, \tag{23}$$

in filament material. Note that we normalize the above energy densities with respect to the wind kinetic energy density, $E_{{\rm k,w}} = \frac{1}{2}\rho_{\rm w} v^2_{\rm w}$.

(F, G) Using equation (23), we calculate two parameters: the averaged turbulent magnetic energy density as $[E'_{{\rm m},\alpha}]$, and the ratio between turbulent magnetic and turbulent kinetic energy densities, i.e. $[E'_{{\rm m},\alpha}]/[E'_{{\rm k},\alpha}]$.

Note that a summary of all the diagnostics described above is presented in Table 2.

[3] Note that the notation used for the list of diagnostics introduced in this section has been chosen so that it matches the notation used for the panels of the figures presented in Section 4. This facilitates the identification of different parameters, their mathematical definitions, and their respective plots (see Table 2).

Table 2. Summary of the diagnostics described in Section 3.3, which we employ to investigate the morphology, energetics, and dynamics of filaments produced in wind–cloud interactions. In column 1, we provide the diagnostic identifier (ID) using the letters A–I, which we also use to label the plots presented in Section 4. In columns 2 and 3, we list the symbol and definition of each diagnostic.

(1) ID	(2) Diagnostic	(3) Description
A	$\xi_{2,\,\alpha}$	Length-to-width aspect ratio
B	$\iota_{1,\,\alpha}$	Lateral width
C	$\delta_{{\rm v}_\alpha}$	Transverse velocity dispersion
D	$[\omega_\alpha]$	Mean vorticity
E	$[E'_{{\rm k},\alpha}]$	Averaged turbulent kinetic energy density
F	$[E'_{{\rm m},\alpha}]$	Averaged turbulent magnetic energy density
G	$[E'_{{\rm m},\alpha}]/[E'_{{\rm k},\alpha}]$	Ratio between turbulent energy densities
H	$\langle X_{2,\,\alpha}\rangle$	Displacement of the centre of mass
I	$\langle v_{2,\,\alpha}\rangle$	Bulk speed in the direction of streaming

3.4 Reference time-scales

The relevant dynamical time-scales in our simulations are:

(i) The cloud-crushing time (see Jones, Kang & Tregillis 1994; Jones et al. 1996),

$$t_{\rm cc} = \frac{2r_{\rm c}}{v_{\rm s}} = \left(\frac{\rho_{\rm c}}{\rho_{\rm w}}\right)^{\frac{1}{2}} \frac{2r_{\rm c}}{\mathcal{M}_{\rm w} c_{\rm w}} = \chi^{\frac{1}{2}} \frac{2r_{\rm c}}{\mathcal{M}_{\rm w} c_{\rm w}}, \tag{24}$$

where $v_{\rm s} = \mathcal{M}_{\rm w} c_{\rm w} \chi^{-\frac{1}{2}}$ is the approximate speed of the internal shock travelling through the cloud after the initial collision with the wind. In order to maintain scalability, all the time-scales reported in this paper are normalized with respect to the cloud-crushing time.

(ii) The simulation time, which in our case is:

$$t_{\rm sim} = 1.25\, t_{\rm cc}. \tag{25}$$

(iii) The wind-passage time:

$$t_{\rm wp} = \frac{2r_{\rm c}}{v_{\rm w}} = \frac{1}{\chi^{\frac{1}{2}}}\, t_{\rm cc} = 0.032\, t_{\rm cc}. \tag{26}$$

(iv) The turbulence-crossing time:

$$t_{\rm tu} = \frac{2r_{\rm c}}{\delta v_{\rm cloud}} = \frac{2r_{\rm c}}{\mathcal{M}_{\rm tu} c_{\rm cloud}} \tag{27}$$

(v) The KH instability growth time (see Chandrasekhar 1961):

$$\frac{t_{\rm KH}}{t_{\rm cc}} \simeq \left[\frac{\rho'_{\rm c}\rho'_{\rm w} k^2_{\rm KH}}{(\rho'_{\rm c}+\rho'_{\rm w})^2}(v'_{\rm w}-v'_{\rm c})^2 - \frac{2B'^2 k^2_{\rm KH}}{(\rho'_{\rm c}+\rho'_{\rm w})}\right]^{-\frac{1}{2}} \frac{\mathcal{M}_{\rm w} c_{\rm w}}{2r_{\rm c}\chi^{\frac{1}{2}}}, \tag{28}$$

where $k_{\rm KH} = \frac{2\pi}{\lambda_{\rm KH}}$ is the wavenumber of the KH perturbations and the primed quantities of the physical variables correspond to their values at the location of shear layers.

(vi) The RT instability growth time (see Chandrasekhar 1961):

$$\frac{t_{\rm RT}}{t_{\rm cc}} \simeq \left[\left(\frac{\rho'_{\rm c}-\rho'_{\rm w}}{\rho'_{\rm c}+\rho'_{\rm w}}\right) a k_{\rm RT} - \frac{2B'^2 k^2_{\rm RT}}{(\rho'_{\rm c}+\rho'_{\rm w})}\right]^{-\frac{1}{2}} \frac{\mathcal{M}_{\rm w} c_{\rm w}}{2r_{\rm c}\chi^{\frac{1}{2}}}, \tag{29}$$

where $k_{\rm RT} = \frac{2\pi}{\lambda_{\rm RT}}$ is the wavenumber of the RT perturbations, a is the local, effective acceleration of dense gas, and the primed quantities

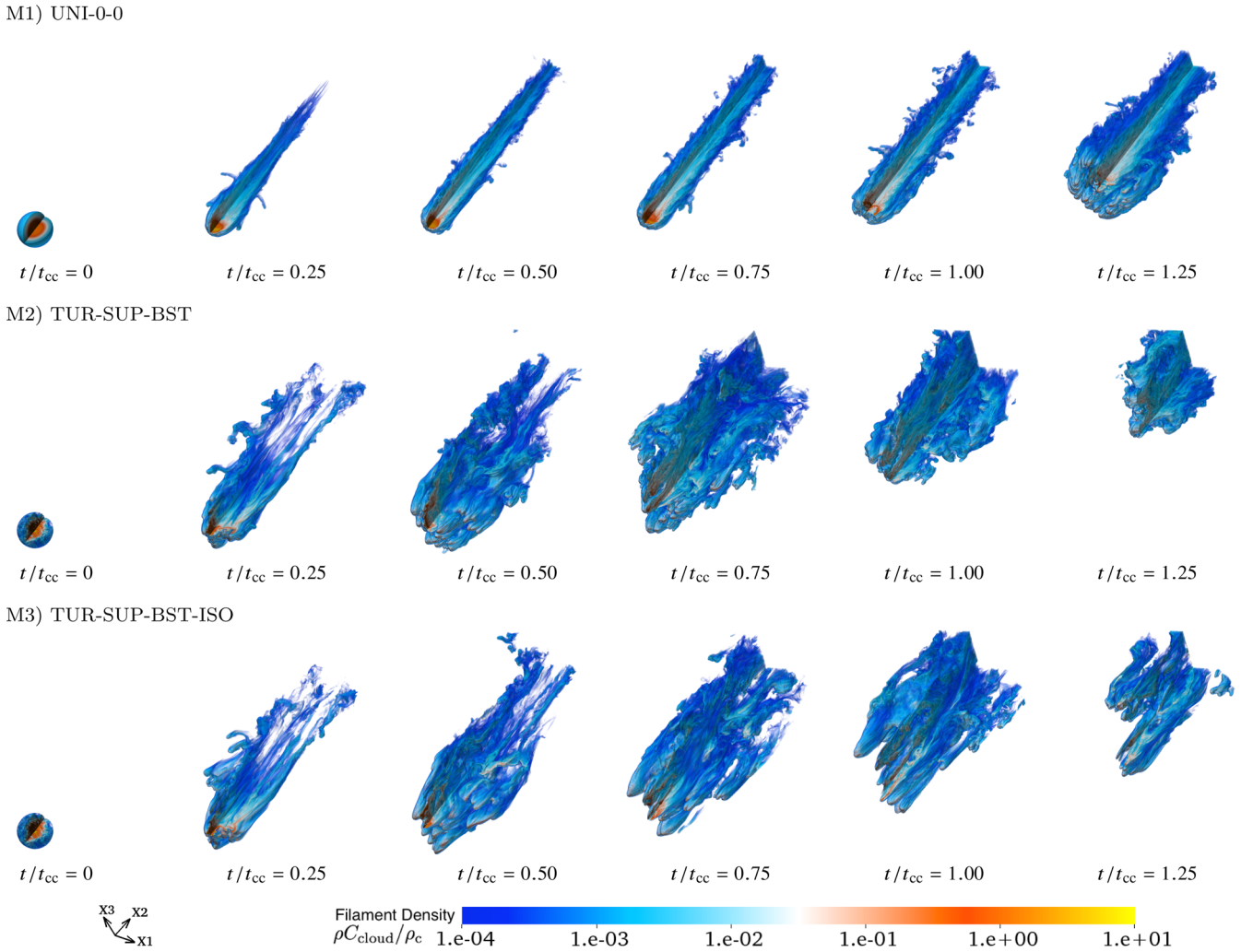

Figure 2. 3D volume renderings of the logarithm of the mass density in filaments (ρC_{cloud}) normalized with respect to the initial cloud density, ρ_c, for $0 \leq t/t_{cc} \leq 1.25$. Panel M1 shows the evolution of an adiabatic, uniform cloud immersed in an oblique magnetic field (UNI-0-0). Panels M2 and M3 show the evolution of turbulent clouds with lognormal density distributions, Gaussian velocity fields, and turbulent magnetic fields with two equations of state: adiabatic (TUR-SUP-BST) and quasi-isothermal (TUR-SUP-BST-ISO), respectively. Note how the inclusion of turbulent clouds leads to the formation of filaments with larger cross-sectional areas, more complex density substructures, and higher displacements in the direction of streaming (i.e. higher accelerations) than the one arising from a uniform cloud. Using a quasi-isothermal (radiative) polytropic index produces less vortices at wind–filament interfaces, leading to the formation of a more laminar filamentary tail. Movies showing the full-time evolution of the models presented here are available online at https://goo.gl/iXgJYk.

of the physical variables correspond to their values at the leading edge of the cloud. Both the KH and RT time-scales in equations (28) and (29), respectively, correspond to the incompressible regime, so they should only be considered as indicative for the highly compressible models considered in this series of papers.

To ensure that sequential snapshots adequately capture details of the evolution of filamentary tails, simulation outputs are written at intervals of $\Delta t = 8.2 \times 10^{-3}\, t_{cc}$.

4 RESULTS

We split this section into two parts. In the first part (Section 4.1), we contrast the overall process of filament formation in uniform and turbulent environments by examining the morphological properties of these structures in three models with the M domain configuration, i.e. with R_{64}, (see Table 1). In this section, we also present a summary of the properties and kinematics of filaments and wind-swept clouds in different models and discuss the entrainment of these structures in supersonic winds. In the second part (Section 4.2), we analyse the effects of turning on and off different profiles for the turbulent density, velocity, and magnetic field distributions of six different models with the S domain configuration, i.e. with R_{128}, (see Table 1). In this section, we systematically investigate models with turbulent clouds and compare the morphological, kinematic, and magnetic properties of the resulting filaments with their non-turbulent counterpart.

4.1 Filament formation and structure in clouds with turbulent density, velocity, and magnetic fields

In this section, we compare the global evolution of wind–cloud systems with uniform and turbulent clouds as they are swept up by a low-density, supersonic wind to form filaments. Figs 2–4 show the time evolution of the mass density, kinetic energy density, and magnetic energy density, respectively, of filament gas in three models,

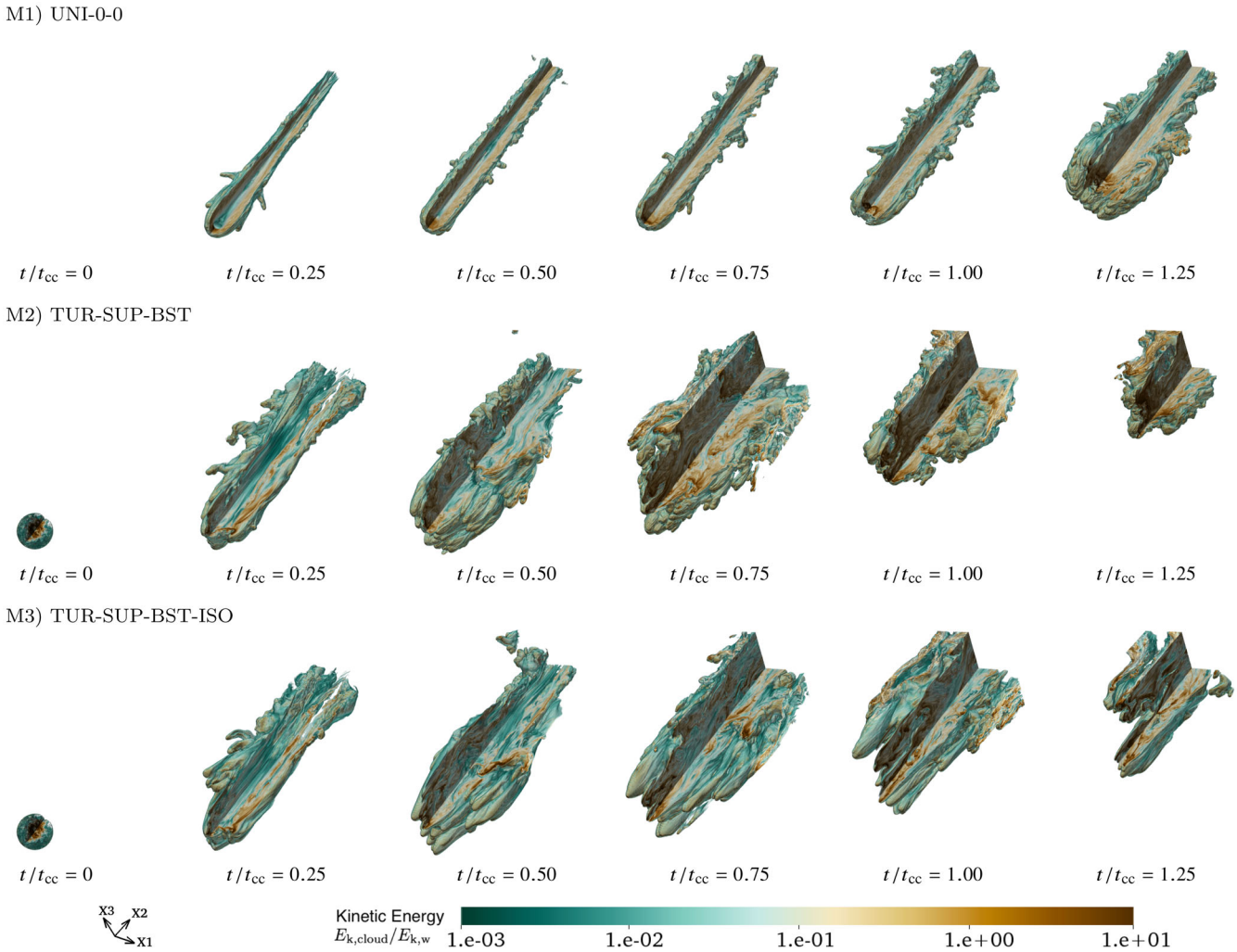

Figure 3. Same as Fig. 2, but here we present 3D volume renderings of the logarithm of the kinetic energy density in filaments ($E_{k,cloud}$) normalized with respect to the wind kinetic energy density, $E_{k,w}$, for $0 \leq t/t_{cc} \leq 1.25$. Panel M1 shows the evolution of a uniform cloud immersed in an oblique magnetic field (UNI-0-0) with an initially-null, internal velocity field. Panels M2 and M3 show the evolution of turbulent clouds with lognormal density distributions, Gaussian velocity fields, and turbulent magnetic fields in adiabatic (TUR-SUP-BST) and quasi-isothermal (TUR-SUP-BST-ISO) cases, respectively. The inclusion of turbulence aids cloud expansion and results in the formation of high-kinetic-energy knots and subfilaments in the interior of the main filamentary tails. The expansion caused by the initial Gaussian velocity field increases the cross-sectional area of the clouds, accelerating them to the point where some parcels of high-density gas have the same kinetic energy of the external wind (see regions in light brown colour). Both turbulent models have higher kinetic energies than the uniform model, but the inclusion of a softer equation of state (see model M3) leads to a more confined, slower turbulent filament than in model M2. Movies showing the full-time evolution of the models presented here are available online at https://goo.gl/iXgJYk.

UNI-0-0, TUR-SUP-BST, and TUR-SUP-BST-ISO, at six different times, namely $t/t_{cc} = 0$, 0.25, 0.5, 0.75, 1.0, and 1.25. All these parameters have been multiplied by the tracer C_{cloud}, so that only filament gas is displayed in the snapshots of these figures. In addition, a quarter of the volume in the rendered images has been clipped to show the internal structure of the clouds and filaments in detail.

The aforementioned figures confirm our previous results presented in Paper I. They show that: (i) a filament can be seen as constituted by two main substructures, namely a tail and a footpoint, and (ii) the formation of filaments is a universal process characterized by four evolutionary phases: (1) A tail formation phase, in which material, mainly removed from the envelope of the cloud (in time-scales of the order of $t/t_{wp} \sim 2$–5; i.e. $t/t_{cc} \sim 0.06$–0.16), is transported downstream to form an elongated tail; (2) A tail erosion phase in which the wind shapes the newly formed tail on time-scales that depend on how fast KH instabilities (e.g. see Murray et al. 1993; Jones et al. 1994; Frank et al. 1996; Ryu, Jones & Frank 2000; Lecoanet et al. 2016) grow at the wind–filament interface; (3) A footpoint dispersion phase in which dense nuclei in the footpoint of the turbulent cloud are disrupted by RT instabilities (e.g. see Nittmann, Falle & Gaskell 1982; Jun, Norman & Stone 1995; Stone & Gardiner 2007), producing subfilamentation; and (4) A free-floating phase in which the filamentary structure loses some coherence and becomes entrained in the wind (see section 4 in Paper I for a full description of the dynamics and time-scales involved in the formation of filaments).

Despite the universality of the global process, Figs 2–4 also show that the disruption process of non-turbulent and turbulent clouds results in filaments with different morphologies. We discuss those differences qualitatively in Sections 4.1.1 and 4.1.2, and quantitatively in Sections 4.1.3 and 4.1.4 below. Note also that if radiative

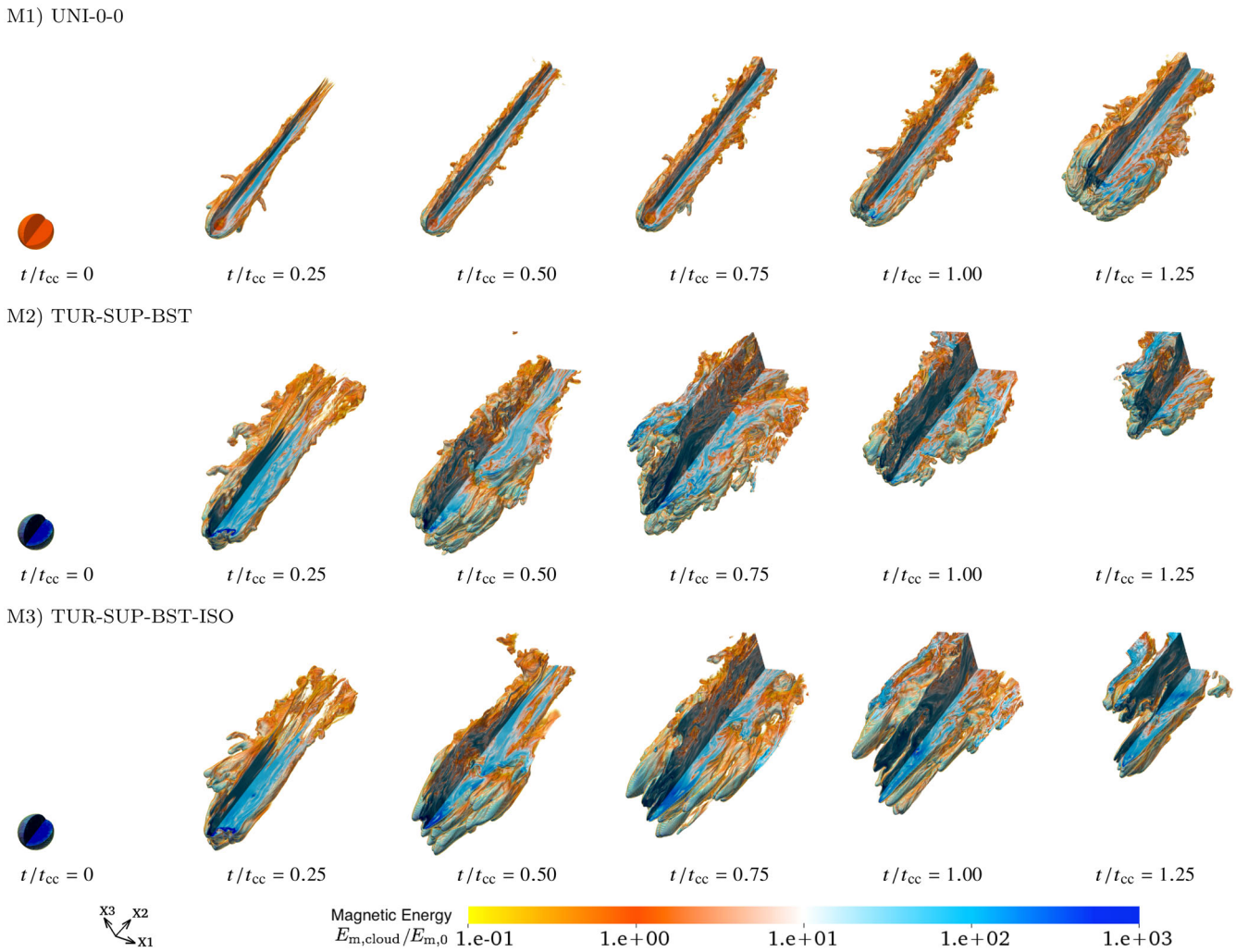

Figure 4. Same as Figs 2 and 3, but here we present 3D volume renderings of the logarithm of the magnetic energy density in filaments ($E_{m,cloud}$) normalized with respect to the initial magnetic energy density in the wind, $E_{m,0}$, for $0 \leq t/t_{cc} \leq 1.25$. Panel M1 shows the evolution of a uniform cloud immersed in a purely oblique magnetic field (UNI-0-0). Panels M2 and M3 show the evolution of turbulent clouds with lognormal density distributions, Gaussian velocity fields, and turbulent magnetic fields in adiabatic (TUR-SUP-BST) and quasi-isothermal (TUR-SUP-BST-ISO) cases, respectively. We note that a fraction of the initially strong magnetic energy in the turbulent magnetic field included in models TUR-SUP-BST and TUR-SUP-BST-ISO dissipates in a few tenths of t_{cc}. After this transient effect, i.e. for times $t/t_{cc} \geq 0.25$, knots and subfilaments remain strongly magnetized with magnetic energy densities as high as those in their progenitor clouds (see Appendix E for a quantitative comparison of the magnetic energy enhancement in different models), thus aiding cloud survival by reducing the disruptive effects of dynamical instabilities. In the radiative case, model TUR-SUP-BST-ISO, this effect is more significant than in the adiabatic model, owing to the extra compression caused by the softer polytropic index used in this model. Movies showing the full-time evolution of the models presented here are available online at https://goo.gl/iXgJYk.

cooling were included when studying specific wind–cloud systems, the time-scales of these phases would change according to their respective cooling time-scales, but not the basic processes that lead to cloud disruption and concomitant filament formation (e.g. see Cooper et al. 2008, 2009).

4.1.1 Uniform versus turbulent cloud models

Here, we compare the filamentary tails in models with uniform clouds versus those in models with turbulent clouds from a qualitative perspective. Contrasting Panel M1 of Fig. 2 with the other two panels (Panels M2 and M3 of Fig. 2) reveals that turbulent clouds produce filaments that are less confined and have more chaotic and sinuous tails than the one arising from a uniform cloud. While the single nucleus in the core of the uniform cloud prevents the wind from rapidly flowing through core material at early stages, the presence of multiple high-density nuclei, surrounded by a low-density internucleus medium, permits a faster percolation of the wind through the footpoints in the turbulent cloud models (in agreement with Cooper et al. 2009; Schneider & Robertson 2017). Thus, the wind in turbulent models removes internucleus material from the clouds and produces a collection of low- and high-density knots and subfilaments along the tail.

Figs 3 and 4 also show the effect mentioned above. For example, Panel M1 of Fig. 3 shows that the gas with high kinetic energy density is confined to the interior of the filament in model UNI-0-0, while Panels M2 and M3 show that the kinetic profile of the gas in the filament is much more anisotropic in models TUR-SUP-BST, and TUR-SUP-BST-ISO than in the uniform case, with various high-kinetic-energy–density knots and subfilaments threading the

tail. The presence of parcels of gas with kinetic energy densities similar to or higher than the kinetic energy density of the wind in the snapshots of Panels M2 and M3 Fig. 3 for times $t/t_{cc} \geq 0.75$ also implies that filaments emerging from turbulent clouds become more easily entrained in a supersonic wind than their uniform counterpart.

In a similar fashion, the snapshots of the magnetic energy density in Panels M2 and M3 of Fig. 4 indicate the presence of several wind-entrained, magnetized subfilaments and cloudlets with more distorted morphologies in the filamentary tails arising from turbulent clouds than in the one emerging from the uniform cloud. The observed difference in the magnetic morphology of filaments can be explained as follows. In the uniform model, UNI-0-0, the regions of high magnetic energy density are confined to the leading edge of the cloud (where the field lines pile up and are stretched by the passage of the wind) and to the rear side of the cloud (where converging shocks advect field lines and fold them to form a current sheet behind the cloud; see section 5.5 in Paper I for a thorough discussion). In this model, a turbulent magnetized tail only appears after the cloud breaks up at $t/t_{cc} = 1.0$. On the other hand, in the turbulent scenarios, TUR-SUP-BST and TUR-SUP-BST-ISO, the presence of the internal, turbulent magnetic field plays two crucial roles in the dynamics of the wind-swept clouds from the very beginning of the simulation: (1) it helps stabilize the cloud against turbulence- and wind-driven expansion and stripping (after an initial, transient phase of turbulence dissipation), and (2) it keeps the filament gas strongly magnetized at all times, thus preventing KH instabilities (arising at wind–cloud interfaces) from quickly disrupting the cloud/filament (in agreement to what was found by McCourt et al. 2015 for tangled, internal magnetic fields). In fact, the reference time-scales for the growth of KH instabilities (see equation 28) in models UNI-0-0, TUR-SUP-BST, and TUR-SUP-BST-ISO are in the ratio $t_{KH,M1}$: $t_{KH,M2}$: $t_{KH,M3} = 1$: 1.5: 1.8, indicating that suppression of long-wavelength ($\lambda_{KH} \sim 1\, r_c$) modes of this instability occurs in models with turbulent clouds. Thus, unlike Cooper et al. (2008, 2009) and Schneider & Robertson (2017), who found that fractal/turbulent clouds are fragmented or disrupted faster than uniform clouds in non-MHD scenarios, we find here that the cloud-crushing time of equation (24) continues to be a good estimate for the overall 'break-up' time of turbulent filaments as their main structures remain coherent for the entire simulation time-scale ($1\, t_{sim}$; see equation 25), owing to the protective effects of internal, turbulent magnetic fields.

Note also that Panels M2 and M3 of Fig. 4 indicate that the knots and subfilaments formed in turbulent models are as strongly magnetized as their progenitor clouds, thus implying that the magnetic field strength in the filament is similar to the initial magnetic field strength in the cloud in models where self-consistent, strong, turbulent magnetic fields are added to the clouds. Indeed, a quantitative analysis of the magnetic energy enhancement presented in Appendix E reveals that the ratio of magnetic energy (and magnetic field strength) in the filament to that in the initial cloud remains nearly constant $\sim$1 over the entire evolution of these simulations. The constancy of this ratio in these models has important implications for astrophysical filaments as it indicates that ISM filaments have the same magnetic field strength as their progenitor clouds. This result is potentially important for the understanding of the formation and evolution of the radio filaments observed in the Galactic Centre as they have been suggested to have magnetic field strengths of the order of the strengths estimated in molecular clouds (e.g. see Roberts 1999; Bicknell & Li 2001).

Another difference between uniform and turbulent cloud models is that the dispersion of the filament footpoints is anisotropic in turbulent scenarios and occurs at the locations of the densest nuclei in the mass distribution of the cloud. Each of these dense regions inside the cloud undergoes a break-up phase of its own, and this occurs faster for more diffuse regions than for denser regions. Consequently, dense regions in the cloud survive longer than diffuse regions and the break-up phase of turbulent clouds is not a drastic, abrupt event in which the structure of a single nucleus is disrupted as in the uniform case (see e.g. the snapshot of model UNI-0-0 at $t/t_{cc} = 1.0$). It is rather a slow, steady process in which several nuclei inside the turbulent cloud are eroded by RT instabilities at distinct locations in the cloud and on different time-scales (see e.g. the snapshot of model TUR-SUP-BST at $t/t_{cc} = 1.0$). The reference time-scales for the growth of RT instabilities (see equation 29) in models UNI-0-0, TUR-SUP-BST, and TUR-SUP-BST-ISO are in the ratio $t_{RT,M1}$: $t_{RT,M2}$: $t_{RT,M3} = 1$: 0.7: 0.9, indicating RT-driven subfilamentation occurs faster in models with turbulent clouds and confirming that strong magnetic fields hasten the growth of long-wavelength ($\lambda_{RT} \sim 1\, r_c$) modes of this instability (in agreement with the results presented in Gregori et al. 1999, 2000; and in section 5.5.1 in Paper I).

Overall, we find in this section that the intrinsic porosity of turbulent clouds facilitates their lateral expansion (increasing their cross-sectional area) and makes them susceptible to a greater ram-pressure force than the one acting upon the uniform cloud. This enhanced drag force pushes these turbulent clouds (regardless of whether or not they are radiative) farther away from their original position than in the uniform scenario during the same time-scale (see e.g. the snapshots at $t/t_{cc} \geq 1.0$). Even though a higher drag force and a more expanded cross-section would mean that turbulent clouds are more prone to the disruptive effects of ablation and dynamical instabilities, we do not find evidence of turbulent clouds being disrupted faster than the uniform cloud as reported in previous HD studies. The reason is that the strong, turbulent magnetic fields, that we self-consistently included in our models, stabilize the clouds against the wind ram pressure and turbulence and keeps dense gas clumped together, thus preventing cloud material from rapidly mixing with wind material via small-scale KH instabilities. This signifies that self-consistently including turbulence in the initial conditions of wind-swept clouds has the effect of increasing cloud acceleration, without affecting cloud shredding and the overall coherence of the resulting filaments. This result is crucial as it shows that the process of entrainment of cold, dense gas into hot, low-density winds is viable (see Section 4.1.4 for further details on the dynamics of filaments and Section 4.2 for further discussion on the protective effects of magnetic fields).

4.1.2 Effects of radiative losses

Panels M2 and M3 of Figs 2–4 can also be compared with one another. The snapshots in these panels show that softening the gas equation of the state to $\gamma = 1.1$ in model TUR-SUP-BST-ISO (in order to mimic the effects of radiative cooling) has three effects on the resulting filaments: (1) it suppresses small-scale KH instability modes at the sides of the cloud, leading to the emergence of a more laminar filament (also seen in model MHD-Ob-I in Paper I); (2) it produces a tail with a collection of linear subfilaments anchored to denser and slower nuclei; and (3) it aids the survival of the filament by preserving its core gas denser and more strongly magnetized than in the adiabatic ($\gamma = \frac{5}{3}$), turbulent model, TUR-SUP-BST. These effects are caused by the increased compression to which the cloud gas is subjected in model TUR-SUP-BST-ISO (see also section 5.3 in Klein et al. 1994 and section 4.5 in

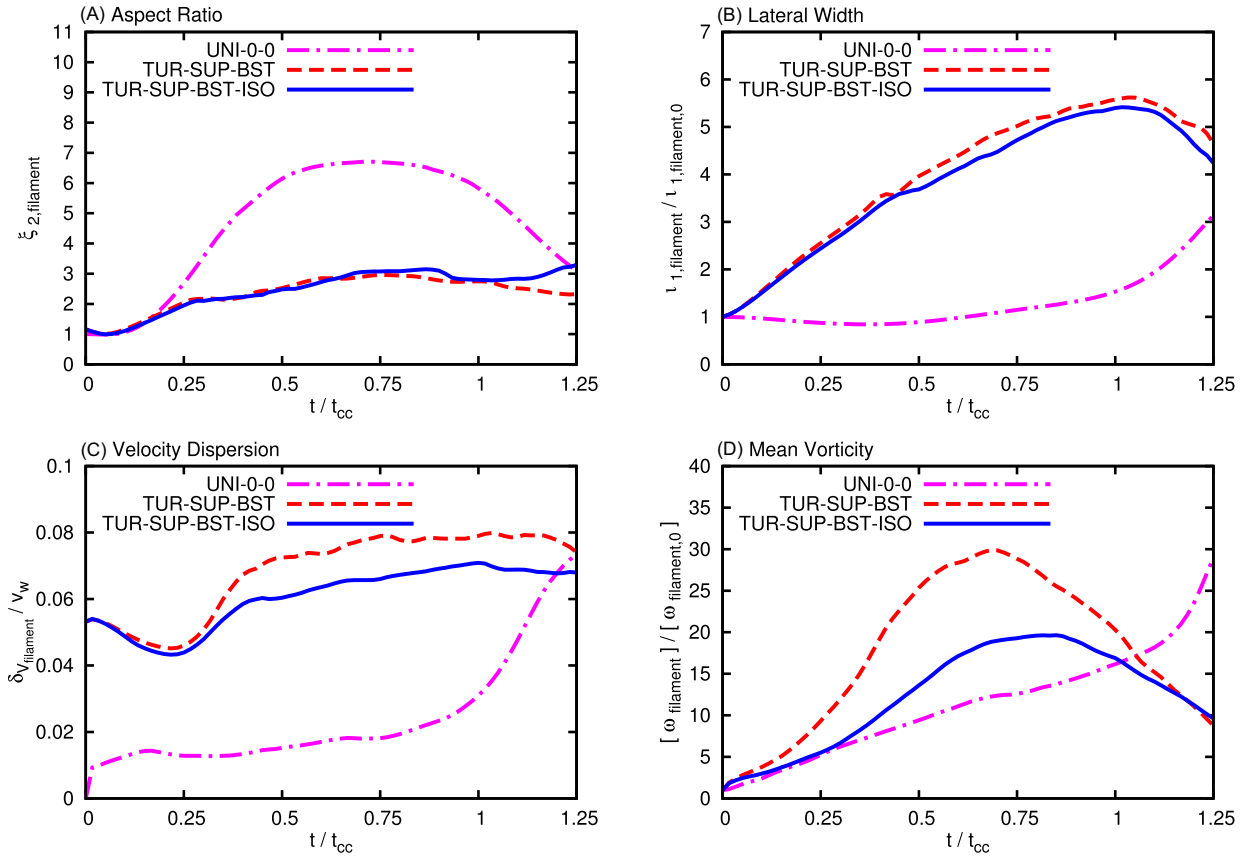

Figure 5. Time evolution of four diagnostics: the aspect ratio (Panel A), the lateral width (Panel B), the transverse velocity dispersion (Panel C), and the mean vorticity enhancement (Panel D), in models UNI-0-0 (dash–dotted line), TUR-SUP-BST (dashed line), and TUR-SUP-BST-ISO (solid line). We find that: (i) turbulence leads to the formation of filaments with greater lateral widths, higher velocity dispersions, and more pronounced vorticity enhancements than the idealized uniform cloud; and (ii) the inclusion of a softer polytropic index to mimic radiative losses in model TUR-SUP-BST-ISO suppresses KH instabilities, thus reducing the lateral elongation, velocity dispersion, and vorticity of the resulting filament.

Nakamura et al. 2006). The higher density contrast at wind–cloud interfaces delays the emergence of small-scale KH instabilities and protects dense regions in the cloud from disruption, thus slowing it down and prolonging its lifetime. The reference time-scales for the growth of KH instabilities (see equation 28) in models TUR-SUP-BST and TUR-SUP-BST-ISO are in the ratio $t_{\rm KH,\,M2}$: $t_{\rm KH,\,M3} = 1$: 1.2, indicating that the emergence of long-wavelength ($\lambda_{\rm KH} \sim 1\,r_{\rm c}$) modes of this instability is delayed in the quasi-isothermal model.

Based on the above results, we find that the ability of a cool, dense cloud to radiate thermal energy away is another crucial element to its survival as entrained structures in a hot, supersonic wind. In adiabatic scenarios, KH instabilities have a pronounced impact on the morphology and lifetime of filaments as the thermally driven expansion accelerates gas mixing and increases the degree of mass stripping and turbulence in the downstream flow. In the radiative scenario, on the other hand, the cloud can cool via thermal radiation, which keeps its gas dense and cold and inhibits KH instabilities at fluid interfaces. As opposed to models of quasi-isothermal, uniform clouds, which produce a single, laminar filament (see fig. 10 in Paper I), in case of turbulent cloud models, the presence of multiple high-density nuclei in their cores result in the formation of tails with several subfilaments along them (each of these subfilaments is supported by one of these nuclei). Subfilamentation of wind-swept clouds is an RT instability-driven process in both uniform and turbulent clouds. We showed in the previous section that this process is more efficient in turbulent cloud models, owing to the porous nature of turbulent density structures, but the extra compression of the gas in model TUR-SUP-BST-ISO slows the cloud down and delays the emergence of RT instability modes. Indeed, the reference time-scales for the growth of long-wavelength ($\lambda_{\rm RT} \sim 1\,r_{\rm c}$) RT instabilities (see equation 29) in models TUR-SUP-BST and TUR-SUP-BST-ISO are in the ratio $t_{\rm RT,\,M2}$: $t_{\rm RT,\,M3} = 1$: 1.4, which is similar to the 1: 1.6 ratio obtained for the adiabatic and quasi-isothermal models of wind-swept uniform clouds discussed in section 5.5.2 in Paper I.

Overall, we find that the ability of the cloud to radiate in model TUR-SUP-BST-ISO effectively suppresses KH instabilities at wind–filament interfaces, thus aiding cloud survival and making its entrainment into the hot, supersonic wind even more feasible than in the turbulent, adiabatic model, TUR-SUP-BST. These findings are in agreement with the conclusions presented in previous studies of radiative wind/shock-swept clouds for different cooling regimes (e.g. see Mellema et al. 2002; Fragile et al. 2004; Melioli et al. 2005; Cooper et al. 2009; Scannapieco & Brüggen 2015).

4.1.3 Filament morphology and energetics

Here, we discuss the role of turbulence on the morphology and energetics of wind-swept clouds (filaments) from a quantitative point of view. Fig. 5 presents the time evolution of four parameters calcu-

lated for cloud/filament material (i.e. using the scalar $C_{\rm cloud}$). Panels A and B show the evolution of two geometrical quantities, namely the aspect ratios (see equation 18) and lateral widths of filaments (see equation 19), respectively. These panels indicate that both turbulent clouds (in models TUR-SUP-BST and TUR-SUP-BST-ISO) have lower aspect ratios than the uniform cloud (in model UNI-0-0) as a result of them being more laterally elongated by a combination of shock- and turbulence-triggered expansion. This behaviour bears out the qualitative analysis presented in the preceding sections: the wind is able to travel across cloud material more easily when its gas is turbulent than when it is uniform, causing the clouds to quickly expand. Note that: (i) the change in the slope of the lateral width curve in model UNI-0-0 is due to the cloud break up via RT instabilities, while (ii) the decline seen in the lateral width of the filaments in models TUR-SUP-BST and TUR-SUP-BST-ISO for times $t/t_{\rm cc} > 1.1$ responds to cloud material starting to leave the computational domain through the sides of it (see Appendix B for a discussion on the effects of the computational domain size on our diagnostics).

Panels C and D of Fig. 5 show the evolution of the transverse velocity dispersions (see equation 20) and mean vorticity enhancements (from equation 16) of filament gas. These panels show two effects: (i) turbulent clouds (in models TUR-SUP-BST and TUR-SUP-BST-ISO) generate filaments with higher velocity dispersions and higher mean vorticities than the uniform cloud (in model UNI-0-0), and (ii) the inclusion of a softer equation of state (with $\gamma = 1.1$) in model TUR-SUP-BST-ISO results in a reduction of the velocity dispersion and small-scale vorticity in filament gas, when compared to its adiabatic counterpart in model TUR-SUP-BST. Regarding the former effect, Panel C shows that clouds with an initially turbulent velocity field remain turbulent throughout the simulation with $\delta_{\rm v_{filament}}/v_{\rm w} = 0.05$–$0.08$, while the uniform cloud has $\delta_{\rm v_{filament}}/v_{\rm w} \sim 0.02$ and only develops a similarly turbulent tail after its core has been disrupted by RT instabilities for $t/t_{\rm cc} \geq 1.0$. The decline seen in the velocity dispersions of the turbulent models for $t/t_{\rm cc} < 0.3$ is due to the initial, transient dissipation of the supersonic turbulence in shocks inside these clouds. Regarding the latter effect, Panels C and D show that the ability of a cloud to radiate energy away is crucial for its survival in a supersonic wind as it suppresses the disruptive effects of KH instabilities by inhibiting the deposit of small-scale vortices at wind–filament interfaces, thus reducing both the velocity dispersions and mean vorticities of filament gas. This is in agreement with our qualitative analysis presented in Section 4.1.2 and also with previous work of radiative clouds interacting with winds/shocks by e.g. Fragile et al. (2005), Orlando et al. (2005), Raga et al. (2007), and Cooper et al. (2009).

The turbulence energetics of our models of wind-swept clouds is another important aspect to be analysed in this section. Panels E, F, and G of Fig. 6 show the evolution of three parameters, namely the average turbulent kinetic energy density (see equation 22), the average turbulent magnetic energy density (see equation 23), and the ratio of these two energy densities, respectively. These panels reveal four effects: (i) turbulent clouds in models TUR-SUP-BST and TUR-SUP-BST-ISO experience a short (transient) period ($0 \leq t/t_{\rm cc} \leq 0.15$) of rapid dissipation of the initially supersonic turbulence prescribed for them; (ii) this dissipation is slightly less significant when the radiative, turbulent cloud in model TUR-SUP-BST-ISO is considered; (iii) the cloud gas in the uniform model UNI-0-0 experiences the opposite effect, becoming turbulent very quickly (also over short time-scales: $0 \leq t/t_{\rm cc} \leq 0.15$); and (iv) after the curves become flat (for times $t/t_{\rm cc} \geq 0.15$), the ratios of turbulent magnetic to turbulent kinetic energy densities remain nearly constant in all models.

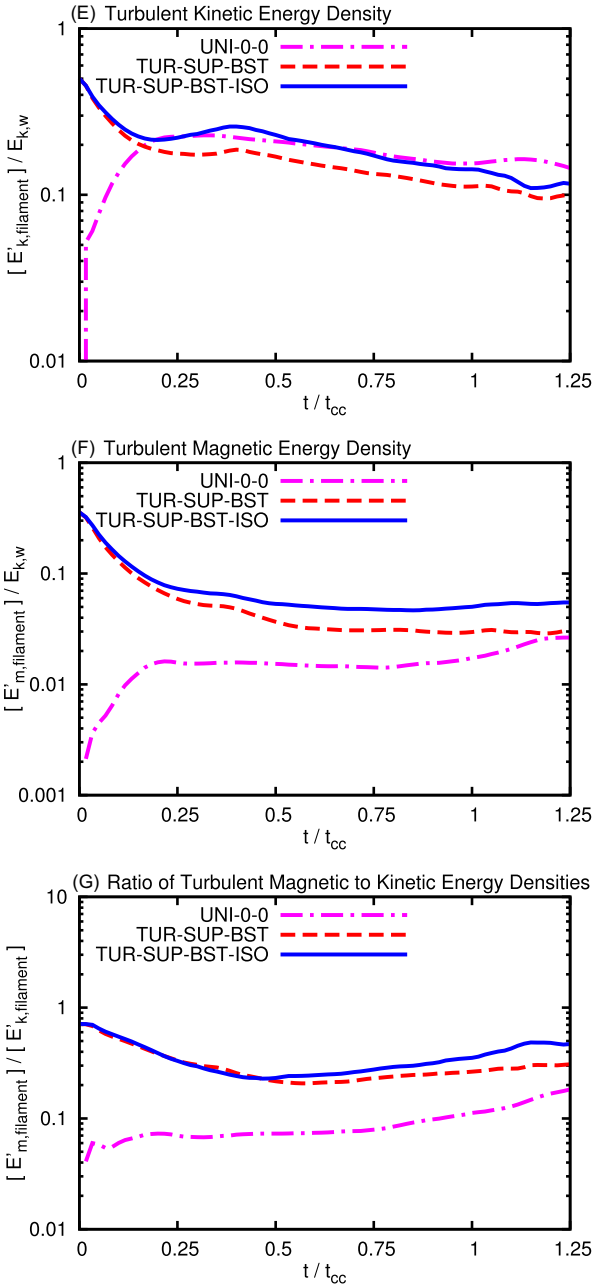

Figure 6. Same as Fig. 5, but here Panels E and F show the average turbulent kinetic and magnetic energy densities, respectively, and Panel G shows the ratio of the two energy densities. We find that: (i) while turbulent clouds undergo a transient period of rapid dissipation of their supersonic turbulence (in shocks), their uniform counterpart becomes turbulent at the beginning of the interaction, and (ii) the ratios of turbulent magnetic to turbulent kinetic energy densities indicate subequipartition and remain nearly constant with values of $[E'_{\rm m,filament}]/[E'_{\rm k,filament}] = 0.1$–$0.4$ in all models.

In order to explain the aforementioned effects, let us discuss the curves presented in Panels E and F of Fig. 6. In both cases, we find a similar time evolution. We observe a decline of the energy densities of turbulence in the filaments of models TUR-SUP-BST and TUR-SUP-BST-ISO. This energy dissipation continues until

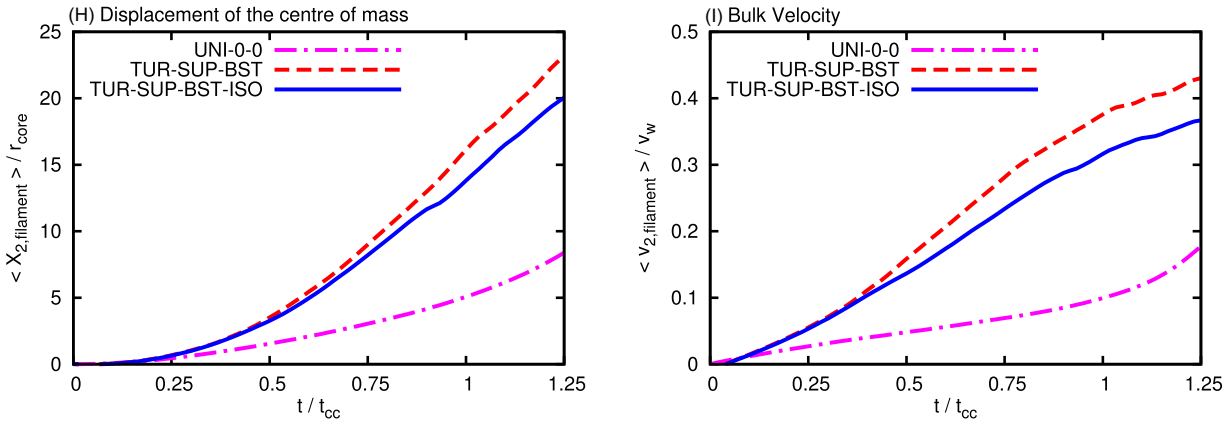

Figure 7. Same as Figs 5 and 6, but here we show the displacement of the centre of mass (Panel H) and the bulk velocity (in the direction of streaming) of wind-swept clouds (filaments) entrained in the wind (Panel I). We find that the cloud with an initially uniform density is 3–4 times slower and travel distances ∼3 times shorter than its turbulent counterparts (at $t/t_{cc} = 1.0$), implying that the self-consistent inclusion of both turbulence and magnetic fields is crucial for the full understanding of the dynamics and entrainment of cold, wind-swept clouds and filaments into hot, supersonic winds.

$t/t_{cc} = 0.15$, when the ram pressure of the external wind equates the pressures (thermal plus magnetic) inside the cloud, and induces the initial expansion of the cloud (see Panel B of Fig. 5). After this time, both the turbulent kinetic and turbulent magnetic energy densities remain nearly constant around $[E'_{k,filament}]/E_{k,w} \sim 0.1$–$0.2$ and $[E'_{m,filament}]/E_{k,w} \sim 0.03$–$0.05$, respectively, until the end of the simulations. The inclusion of a softer polytropic index (i.e. of radiative cooling) in model TUR-SUP-BST-ISO prevents cloud gas from being overheated and keeps the gas dense and strongly magnetized, thus reducing its turbulent dissipation and quenching its expansion (see Panel B of Fig. 5). As a result, the radiative filament in this model exhibits turbulent kinetic and turbulent magnetic energy densities ∼30 per cent and ∼60 per cent higher, respectively, than the adiabatic filament in model TUR-SUP-BST (despite being more collimated than it) at all times. In the case of the filament arising from the non-turbulent cloud model, UNI-0-0, Panels E and F of Fig. 6 show that the energy densities increase very rapidly at the beginning of the interaction (until $t/t_{cc} \sim 0.2$) as a result of the cloud gas being shock-heated and exposed to small-scale instabilities. After this time, both turbulent energy densities also remain nearly constant around $[E'_{k,filament}]/E_{k,w} \sim 0.15$ and $[E'_{m,filament}]/E_{k,w} \sim 0.02$, respectively, until $t/t_{cc} = 1.0$, when the RT instability-driven break up of the spherical cloud tangles the magnetic field (note e.g. how the turbulent magnetic energy densities in models UNI-0-0 and TUR-SUP-BST approach $[E'_{m,filament}]/E_{k,w} \sim 0.03$ towards the end of the evolution).

Overall, we find that the ratio of turbulent magnetic to turbulent kinetic energy densities in the filaments considered in this section remain nearly constant throughout the evolution of both uniform and turbulent cloud models, with values in the range $[E'_{m,filament}]/[E'_{k,filament}] = 0.1$–$0.4$. Filaments arising from uniform clouds favour the lower limit of this range, while turbulent filaments favour the upper limit (owing to their enhanced magnetic energy density). This result has important implications for observations as it indicates that the magnetic field in wind-swept clouds and filaments is in subequipartition with respect to the turbulent kinetic energy density, suggesting that this property can be used to constrain the magnetic field strength of wind-swept ISM clouds and filaments from their observed kinetic properties.

4.1.4 Dynamics and entrainment of wind-swept clouds

As mentioned above, turbulent clouds are more easily expanded by shocks and turbulence than uniform clouds, but does this affect the bulk dynamics of the resulting filaments? Do turbulent clouds move faster than uniform clouds to reach larger distances when immersed in a supersonic wind? Recent studies of fractal or turbulent clouds show that turbulent clouds are more easily disrupted by dynamical instabilities than uniform clouds (e.g. see Cooper et al. 2009; Schneider & Robertson 2017), implying that interstellar clouds (either spherical or turbulent) are unlikely to be ram pressure accelerated for long times before being fully disrupted (e.g. see Zhang et al. 2015; Thompson et al. 2016). However, these models did not consider the effects of tangled or turbulent magnetic fields threading the clouds, which have been demonstrated to provide support to spherical, wind-swept clouds by reducing the mixing of cloud material with ambient gas and thus prolonging their lifetime (e.g. see McCourt et al. 2015, Paper I). Here, we use Fig. 7 to discuss a broader view of the dynamics of clouds than previous models by investigating the motion of clouds and filaments that self-consistently incorporate turbulence and magnetic fields. We show that both turbulence and magnetic fields play significant roles in accelerating clouds and prolonging their lifetimes.

Fig. 7 shows the displacement of the centre of mass (Panel H) and the bulk velocity (Panel I) of filaments in models UNI-0-0, TUR-SUP-BST, and TUR-SUP-BST-ISO as a function of time. Panel H indicates the distances travelled by each filament as measured by $\langle X_{2,filament} \rangle$, normalized with respect to the initial radius of the cloud core, r_{core} (from equation 17). We see that the wind transports turbulent clouds/filaments over distances equivalent to $\langle X_{2,filament} \rangle / r_{core} \sim 14$–$16$, in the direction of streaming (measured at $t/t_{cc} = 1.0$). These distances are 2–3 times as large as the distances to which uniform clouds are transported over the same time-scale (i.e. $\langle X_{2,filament} \rangle / r_{core} \sim 6$ at $t/t_{cc} = 1.0$), implying that the inclusion of turbulence aids cloud acceleration. The main driver of the cloud dynamics is the supersonic wind in all models, but self-consistent, turbulent clouds undergo higher accelerations than their uniform counterpart as a result of their larger cross-sectional areas (see Section 4.1.3). As mentioned earlier, the presence of internal, turbulent magnetic fields in models TUR-SUP-BST and TUR-SUP-BST-ISO

is crucial as it forms an effective magnetic shield (in agreement with Jones et al. 1996; Miniati et al. 1999b, Paper I) that prevents their enhanced accelerations from disrupting the cloud by suppressing KH instabilities at wind–cloud interfaces.

To confirm the above result, we also investigate the range of velocities that are characteristic of the wind-embedded filaments at $t/t_{cc} = 1.0$. We use our definition of the mass-weighted bulk velocity, i.e. $\langle v_{2,\rm filament}\rangle$, normalized with respect to the wind speed, v_w (from equation 17), to study the bulk motion of filaments in the direction of streaming. Panel I of Fig. 7 provides these measurements and shows that the bulk speed in turbulent models has values $\langle v_{2,\rm filament}\rangle/v_w \sim 0.32$–$0.37$ at $t/t_{cc} = 1.0$, which are 3–4 times larger than the bulk speed acquired by the uniform cloud, $\langle v_{2,\rm filament}\rangle/v_w \sim 0.1$, over the same time-scale. The bulk speed in the uniform scenario, UNI-0-0, only increases after the RT-instability-driven break up of its footpoint at $t/t_{cc} = 1.0$ as a result of the rapid growth of its cross-sectional area. Despite this, the cloud/filament in the uniform scenario is always slower than its turbulent counterparts, confirming that the inclusion of turbulence and self-consistent magnetic fields favours the entrainment of cold, dense, high-speed gas into hot, diffuse, supersonic winds. Note that our simulations show that dense clouds and their associated filamentary tails can be effectively advected by a global, supersonic wind to reach larger distances, provided that realistic levels of turbulence and magnetic fields are included self-consistently.

As mentioned in Section 4.1.1, turbulent clouds favour the formation of smaller subfilaments and cloudlets along their filamentary tails. These substructures are not destroyed in one cloud-crushing time, but they also become entrained in the wind and quickly accelerate after $t/t_{cc} = 1.0$. Panels H and I of Fig. 7 show that these wind-entrained structures reach distances $\langle X_{2,\rm filament}\rangle/r_{\rm core} \sim 20$–$24$ and attain bulk speeds $\langle v_{2,\rm filament}\rangle/v_w \sim 0.36$–$0.42$, respectively, in turbulent models. By contrast, the uniform (non-turbulent) cloud only reaches distances of $\langle X_{2,\rm filament}\rangle/r_{\rm core} \sim 8$ and bulk speeds of $\langle v_{2,\rm filament}\rangle/v_w \sim 0.18$ at $t/t_{cc} = 1.25$. These results are crucial for our understanding of the transport of dense material from low to high latitudes in galactic winds and outflows (e.g. see Strickland et al. Sofue & Handa 1984; 1997; Lehnert et al. 1999; Bland-Hawthorn & Cohen 2003; Su et al. 2010), but our current setups do not allow us to follow the full evolution of these substructures for times longer than 1 $t_{\rm sim}$. Thus, future numerical work, including larger simulation domains is warranted to investigate the fate of these substructures.

4.2 Disentangling the relative contributions of turbulent density, velocity, and magnetic fields

In the previous sections, we compared the evolution of filaments emerging from a uniform cloud and from self-consistent, turbulent cloud models with the aim of understanding the effects of turbulence and magnetic fields on the morphology, energetics, and dynamics of filaments. However, self-consistent models do not allow us to differentiate between the roles of the different components of turbulence. Thus, the relative effects of turbulent density profiles, turbulent velocity fields, and turbulent magnetic fields need to be disentangled by exploring their effects on clouds separately. In this section, we discuss the qualitative and quantitative effects of systematically adding turbulent density, velocity, and magnetic field distributions to the initial clouds on the evolution of several diagnostics. We use wind–cloud models with higher resolutions, i.e. R_{128}, (in smaller computational domains) to perform this comparison. In Section 4.2.1, we discuss qualitative aspects, whilst in Sections 4.2.2–4.2.4, we discuss the implications of adding turbulence to cloud models on the formation and evolution of filaments in a quantitative manner.

4.2.1 *On the morphology of filaments*

In this section, we describe the magnetic structure of filaments in different models. The 3D volume renderings of Fig. 8 show the time evolution, for $0 \leq t/t_{cc} \leq 1.25$, of the normalized magnetic energy density of wind-swept clouds in six different models with the S domain configuration (see Table 1). The reference time-scales for the growth of KH instabilities (see equation 28) and RT instabilities (see equation 29) at wind-filament interfaces in models Uni-0-0, Tur-0-0, Tur-Sub-0, Tur-Sup-0, Tur-Sub-Bwk, and Tur-Sub-Bst are in the ratios $t_{\rm KH,\,S4}$: $t_{\rm KH,\,S5}$: $t_{\rm KH,\,S6}$: $t_{\rm KH,\,S7}$: $t_{\rm KH,\,S8}$: $t_{\rm KH,\,S9}$ = 1: 0.9: 0.9: 0.6: 1.1: 1.5 and $t_{\rm RT,\,S4}$: $t_{\rm RT,\,S5}$: $t_{\rm RT,\,S6}$: $t_{\rm RT,\,S7}$: $t_{\rm RT,\,S8}$: $t_{\rm RT,\,S9}$ = 1: 1: 1: 0.4: 0.9: 0.8, respectively, for $\lambda_{\rm KH} = \lambda_{\rm RT} \sim 1\,r_c$. These calculations indicate that the inclusion of different turbulence profiles in the clouds leads to varying levels of suppression or enhancement of dynamical instabilities and thus to morphological differences in the resulting filaments. We discuss these differences below.

Panel S4 of Fig. 8 shows the magnetic structure of the filament in model Uni-0-0. In this model, a uniform, spherical cloud is uniformly magnetized at the beginning of the simulation (same as model UNI-0-0, but in a smaller computational domain). As a result of compression, and folding and stretching of magnetic field lines, respectively, two regions of high magnetic energy are identified at $t/t_{cc} = 0.25$: the first one is located at the front end of the filament footpoint, while the second one extends along the tail embedding an obliquely oriented current sheet (same as in model UNI-0-0). The magnetic energy in the core of the cloud remains unchanged at this time, but as the late expansion (for $t/t_{cc} \geq 0.5$) of the core takes place, its magnetic energy is progressively amplified $\sim 10^2$–10^3 times (see section 5.5 of Paper I for further details). At $t/t_{cc} = 1.0$, the footpoint is dispersed and the magnetic field at the leading edge of the cloud becomes turbulent with small-scale vortical motions dominating at later times.

Panel S5 of Fig. 8 shows the evolution of the magnetic energy density in model Tur-0-0. In this model the wind strikes a static cloud with a turbulent density distribution, initially immersed in a uniformly magnetized medium. After the filamentary tail forms downstream, both the footpoint and the tail of the filament are affected by shock-triggered turbulence and vortical motions. As a result, the structure of this filament is more chaotic than the one in model Uni-0-0. In model Tur-0-0, the magnetic field lines fold and stretch around the most massive nuclei in the cloud's core. Since the distribution of these nuclei is anisotropic, the magnetotail becomes inhomogeneous. This results in the magnetic field being locally enhanced in regions sheltered by or in between dense nuclei in the core (see the snapshots for $0.25 \leq t/t_{cc} \leq 1.00$), while remaining unchanged at other locations. Thus, models Uni-0-0 and Tur-0-0 produce filaments that are structurally different: a uniform cloud favours the formation of a filament with a single current sheet, while a turbulent cloud produces a filamentary tail filled with several highly magnetized knots and subfilaments (at which $E_{\rm m,cloud}/E_{\rm m_0} \sim 10^2$–$10^3$). Similar structures have been found in purely HD and MHD simulations of shocks interacting with inhomogeneous media, i.e. systems that have more than one cloud (e.g. see Poludnenko et al. 2002; Pittard et al. 2005; Raga et al. 2009; Alūzas et al. 2012, 2014; Rybakin, Smirnov & Goryachev 2016).

Panel S6 of Fig. 8 shows the magnetic structure of the filament in model Tur-Sub-0. In this model, the cloud is initialized with the

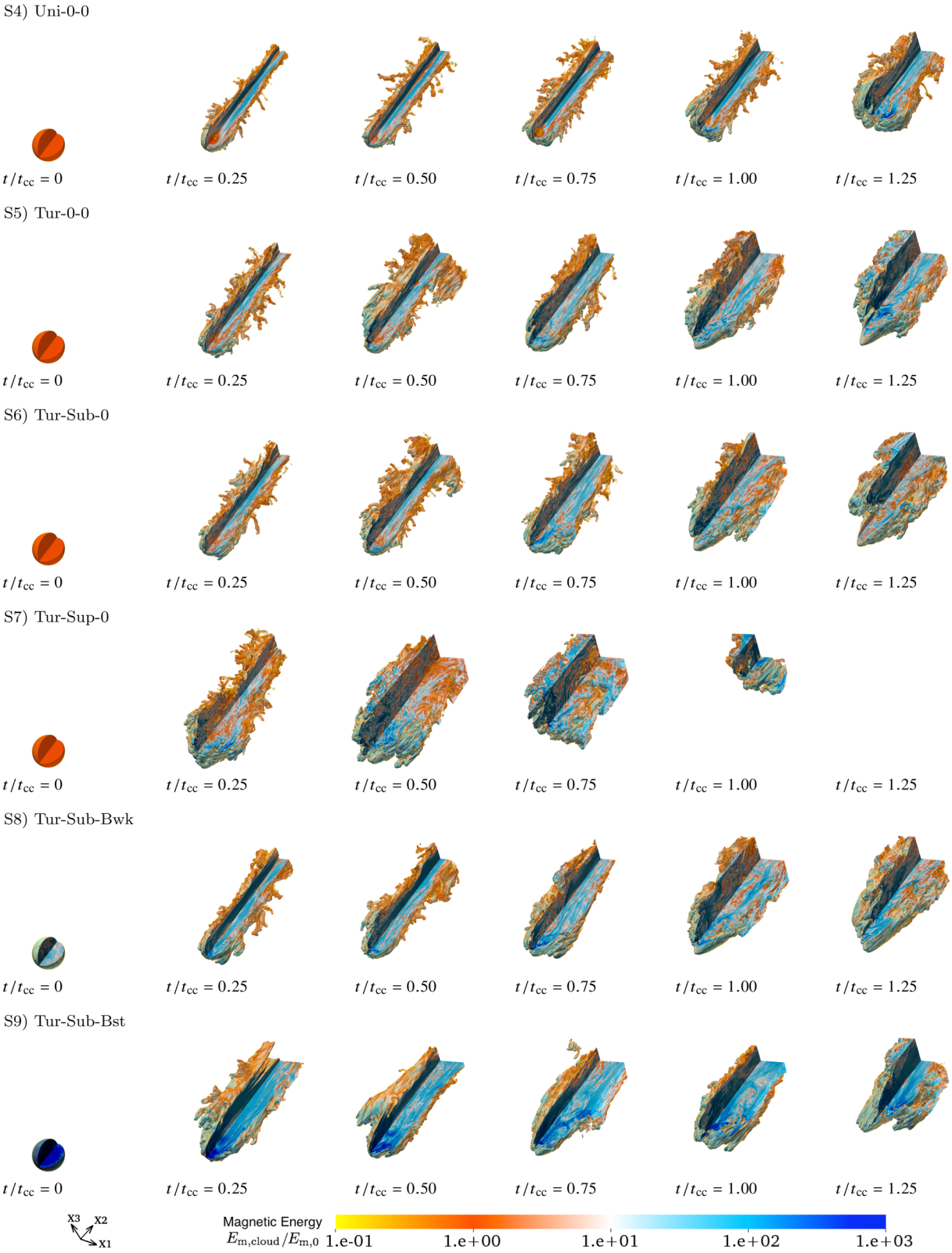

Figure 8. Same as Fig. 4, but here we present the evolution of the normalized magnetic energy density in six models with the S domain configuration for $0 \leq t/t_{cc} \leq 1.25$. Panels S4 and S5 show clouds with uniform (Uni-0-0) and turbulent (Tur-0-0) densities (but without turbulent velocity or magnetic fields), respectively. Panels S6 and S7 show turbulent clouds with turbulent, subsonic (Tur-Sub-0) and supersonic (Tur-Sup-0) velocity fields, respectively. In models S4–S7, the clouds are immersed in a uniform, oblique magnetic field. Panels S8 and S9 present turbulent clouds with weak (Tur-Sub-Bwk) and strong (Tur-Sub-Bst) turbulent magnetic fields, plus turbulent density and velocity fields. Movies of these renderings are available online at https://goo.gl/iXgJYk.

same density distribution used for model Tur-0-0, plus a subsonic, Gaussian velocity field (with a Mach number of $\mathcal{M}_{\rm tu} = 0.33$). We find no qualitative difference in the magnetic structure of filaments in models Tur-0-0 and Tur-Sub-0 throughout the entire evolution. Both models, Tur-0-0 and Tur-Sub-0, produce filaments with non-uniform structures characterized by the presence of strongly magnetized knots and subfilaments along their tails. This implies that a subsonically turbulent velocity field does not provide a sufficiently high (extra) kinetic energy density to the cloud to have significant effects on the morphology and dynamics of the resulting filament. This result is expected from analytical estimates of the ratio of the turbulence-crossing and the cloud-crushing time-scales, i.e. $t_{\rm tu}/t_{\rm cc} \sim 12$, which indicates that a subsonically turbulent velocity field with $\mathcal{M}_{\rm tu} = 0.33$ would need $\sim$12 cloud-crushing times to have a dynamical impact on the cloud (see equation 27).

Panel S7 of Fig. 8 shows the evolution of the magnetic energy in model Tur-Sup-0. This model is started with the same density PDF and magnetic field configuration previously assigned to the above models, plus a supersonic, turbulent velocity field with Mach number of $\mathcal{M}_{\rm tu} = 8.9$ (consistent with the original Mach number of the cloud extracted from Federrath & Klessen 2012; see Section 3.2). The turbulence-crossing time (see equation 27) for this model is of the order of $t_{\rm tu}/t_{\rm cc} \sim 0.4$, i.e. turbulence is dynamically important for this system. The cloud in this model expands quickly from the very beginning of the interaction as a result of internal turbulent motions. This increases the effective cross-section upon which the ram-pressure force acts and the cloud becomes prone to longer wavelength, highly disruptive unstable modes. Both the KH and RT instabilities grow faster in this model than in any of the other turbulent cloud models, e.g. the growth time-scales of KH and RT modes with $\lambda_{\rm KH} = \lambda_{\rm RT} \sim 1\, r_{\rm c}$ are in the ratios $t_{\rm KH,\,S5}$: $t_{\rm KH,\,S7} = 1$: 0.7 and $t_{\rm RT,\,S5}$: $t_{\rm RT,\,S7} = 1$: 0.4, respectively, in models Tur-0-0 and Tur-Sup-0. This signifies that the supersonic cloud is dispersed, mixed with the wind, and disrupted faster than in the turbulent models discussed above. In fact, we find that the cloud break up occurs on time-scales of the order of the turbulence-crossing time-scale rather than in the typical $t/t_{\rm cc} \sim 1.0$. After the break up, the cloud expands beyond the boundaries of the computational domain, making the bow shock at its leading edge vanish and biasing the qualitative results to low-velocity-dispersion gas. Since the cloud moves very quickly out of the computational domain, we stop this simulation shortly after $t/t_{\rm cc} = 1.0$.

Panel S8 of Fig. 8 shows the evolution of the magnetic energy density in model Tur-Sub-Bwk, in which a weak, turbulent magnetic field (with $[\beta_{\rm tu}] = 4$) is added to the initial cloud, alongside the turbulent density and velocity fields of the previous models. In this simulation, we observe a filament with a similar structure to the ones emerging from models Tur-0-0 and Tur-Sub-0, but its interior harbours a larger number of strongly magnetized subfilaments and a more laminar magnetotail (see the snapshots for $0.25 \leq t/t_{\rm cc} \leq 0.75$). The magnetic field strength of the knots and subfilaments in this model is also higher than in the cases without turbulent magnetic fields, owing to the stretching of magnetic field lines anchored to regions of high density (dense nuclei) in the footpoint. By the end of the evolution, vortical motions dominate and the filament in model Tur-Sub-Bst resembles the others in models Tur-0-0 and Tur-Sub-0, displaying knots and subfilaments with similar magnetic field strengths ($E_{\rm m,cloud}/E_{\rm m_0} \sim 10^2$–$10^3$). The principal effect of the weak, turbulent magnetic field in this model is to mildly protect the cloud/filament from KH instabilities emerging at wind–cloud interfaces as revealed by the enhanced laminarity of its filament with respect to those in models Tur-0-0 and Tur-Sub-0. Indeed, the reference growth time-scales of KH instabilities with $\lambda_{\rm KH} \sim 1\, r_{\rm c}$ are in the ratio $t_{\rm KH,\,S6}$: $t_{\rm KH,\,S8} = 1$: 1.2 in models Tur-Sub-0 and Tur-Sub-Bwk.

Panel S9 of Fig. 8 shows the morphology of the filament in model Tur-Sub-Bst. The cloud in this model is initialized with a strong, turbulent magnetic field (with $[\beta_{\rm tu}] = 0.04$) on top of the turbulent density and velocity fields used in the above models. The previously mentioned effects of a turbulent magnetic field on the morphology of the cloud are also seen in this model. The tail of this filament is inhabited by magnetized knots and subfilaments with higher magnetic energies ($E_{\rm m,cloud}/E_{\rm m_0} \sim 10^3$–$10^4$) and it is more laminar than in the weak-field case (model Tur-Sub-Bwk). The higher magnetic pressure produces two effects: (i) it further shields the magnetotail, suppressing KH instabilities at wind–filament boundaries (the reference time-scales for the growth of KH instabilities with $\lambda_{\rm KH} \sim 1\, r_{\rm c}$ are in the ratio $t_{\rm KH,\,S6}$: $t_{\rm KH,\,S9} = 1$: 1.6 in models Tur-Sub-0 and Tur-Sub-Bst); and (ii) it enhances the growth of RT instabilities at the leading edge of the cloud (the reference time-scales for the growth of RT instabilities with $\lambda_{\rm RT} \sim 1\, r_{\rm c}$ are in the ratio $t_{\rm RT,\,S6}$: $t_{\rm RT,\,S9} = 1$: 0.9 in models Tur-Sub-0 and Tur-Sub-Bst), in agreement with previous MHD studies, e.g. Jones et al. 1996; Miniati et al. 1999a; Gregori et al. 1999, 2000, Paper I. In fact, after $t/t_{\rm cc} = 0.75$, small-scale RT bubbles penetrate the front end of the cloud and push material laterally, thus forming a series of subfilaments along the tail.

Overall, the panels of Fig. 8 reveal an important property of interstellar filaments that are produced by wind–cloud interactions. In agreement with our result in Section 4.1.1 for the turbulent models TUR-SUP-BST and TUR-SUP-BST-ISO, the 3D renderings in Panel S9 of Fig. 8 (for model Tur-Sub-Bst) show that several knots and subfilaments have magnetic energy densities similar to that in the initial cloud, confirming that the inclusion of realistic, strong magnetic fields into the initial cloud results in a filament with similarly strong magnetic fields (see Appendix E for further details). In addition, the above results also highlight the importance of including self-consistent turbulent magnetic fields when considering supersonic clouds as they prevent the cloud from being rapidly shredded, while it expands and clumps into smaller knots and subfilaments (see Appendices F and G for details on mixing fractions and clumping factors, respectively, in these models). The turbulent destruction of clouds has been studied in both inviscid, turbulent models (e.g. see Cooper et al. 2009; Schneider & Robertson 2017) and subgrid turbulent viscosity models (e.g. see Pittard et al. 2009, 2010, 2011; Pittard & Parkin 2016; Goodson et al. 2017) of wind–/shock–cloud systems. In agreement with the conclusions drawn from these studies, our results here show that turbulence by itself may potentially have the ability to disrupt a cloud by increasing the mixing of cloud and wind material via hastened dynamical instabilities. Thus, magnetic fields should be a crucial ingredient of any realistic wind–cloud system as they help maintain the stability of wind–cloud interfaces and delay cloud/filament disruption (as we also pointed out in Section 4.1).

4.2.2 *On the lateral width, velocity dispersion, and vorticity*

In this and subsequent sections, we describe the above models by examining the evolution of different diagnostics in the tails (using the scalar $C_{\rm envelope}$) and footpoints (using the scalar $C_{\rm core}$) of filaments, separately. Fig. 9 shows the time evolution of three parameters: the lateral width (Panels B1 and B2), velocity dispersion (Panels C1 and C2), and mean vorticity enhancement (Panels D1 and D2), for tail (left-hand side column) and footpoint (right-hand side column) material, respectively.

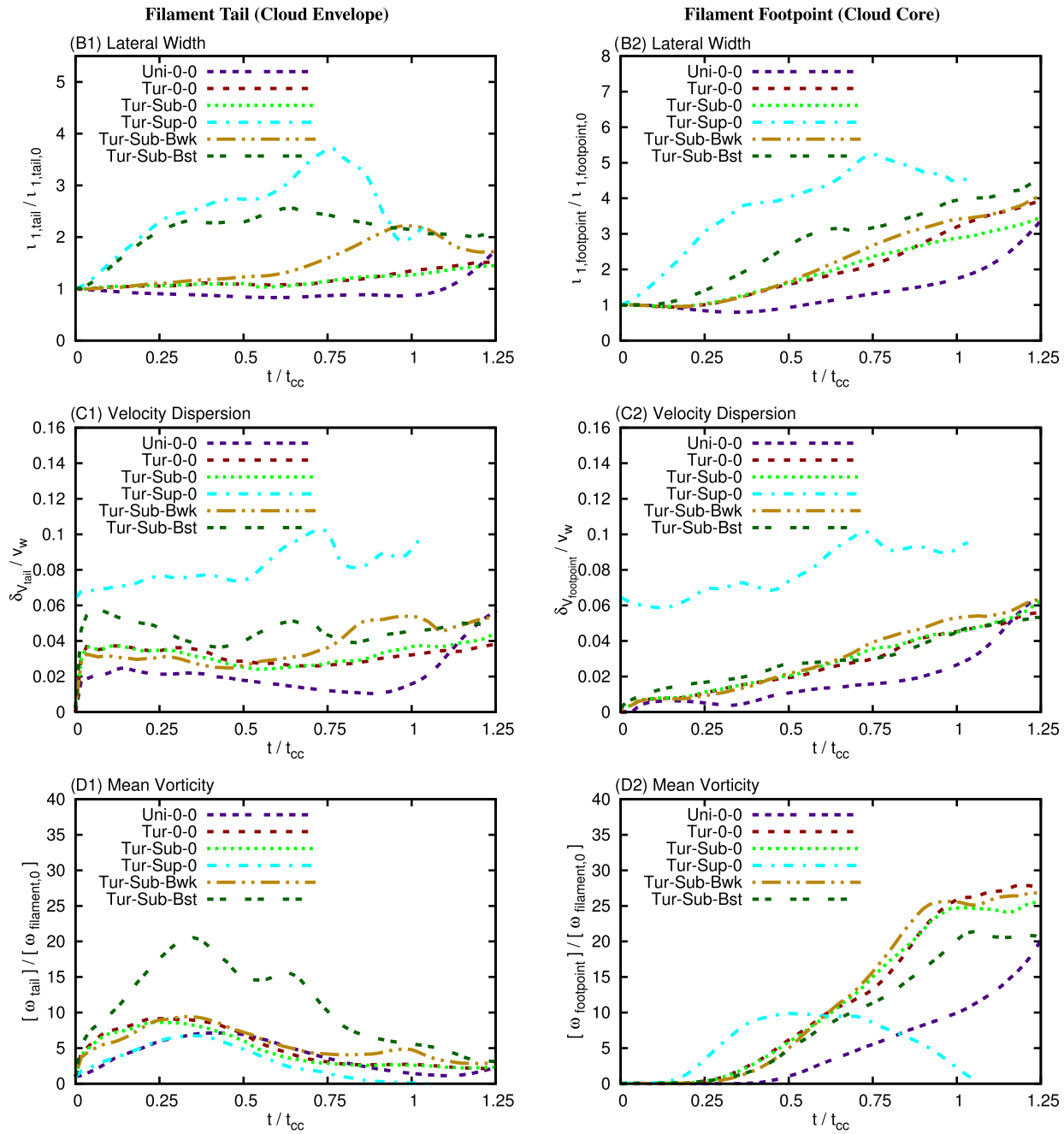

Figure 9. Time evolution of three diagnostics in the tails (left-hand side column) and footpoints (right-hand side column) of filaments in six models with the S configuration (see Table 1). Panels B1 and B2 show the lateral widths, Panels C1 and C2 show the transverse velocity dispersions, and Panels D1 and D2 show the mean vorticity enhancements, in models Uni-0-0 (four-dashed line), Tur-0-0 (long-dashed line), Tur-Sub-0 (dotted line), Tur-Sup-0 (short dash–dotted line), Tur-Sub-Bwk (long-dash-two-dotted line), and Tur-Sub-Bst (two-dashed line). We find that turbulent cloud models produce filaments with greater lateral elongations, higher velocity dispersions, and higher vorticity enhancements than the uniform cloud model. The largest effect on these diagnostics is produced by supersonic velocity fields, followed by strong magnetic fields, and then by turbulent density distributions.

These diagnostics reveal that turbulent models produce filaments with greater lateral elongations, higher velocity dispersions, and higher relative vorticities than the uniform model. In order of significance, we observe that supersonic velocity fields (see model Tur-Sup-0) cause the most pronounced effect, owing to the fast expansion of cloud gas triggered by the thermal energy injected into the cloud via turbulence dissipation (which mainly occurs in internal shocks). Lateral widths are 3–4 times larger than in models Uni-0-0 and Tur-0-0, with values of $\iota_{1,\,\mathrm{tail}}/\iota_{1,\,\mathrm{tail},\,0} \sim 3$ and $\iota_{1,\,\mathrm{footpoint}}/\iota_{1,\,\mathrm{footpoint},\,0} \sim 4$–5 being characteristic of the tail (Panel B1) and footpoint (Panel B2), respectively, of the filament in model Tur-Sup-0. Similar ratios between the velocity dispersions in models Tur-Sup-0 and Tur-0-0 are observed in Panels C1 and C2, in which the supersonically turbulent velocity field produces transverse velocity dispersions $\delta_{v_{\mathrm{tail}}}/v_{\mathrm{w}} \sim \delta_{v_{\mathrm{footpoint}}}/v_{\mathrm{w}} \sim 0.06$–$0.08$ in both the tail and footpoint of the filament. Since the cloud in this model is

already supersonically turbulent at the beginning of the simulation, little additional vorticity is deposited in both the tail and footpoint of its filament, as indicated by the evolution of the mean vorticity enhancement in Panels D1 and D2. Note that the unbound, turbulence-triggered cloud expansion causes a large fraction of cloud material in model Tur-Sup-0 to leave the computational domain through its sides after $t/t_{cc} = 0.4$. By $t/t_{cc} = 1.0$, ∼80 per cent of the cloud has left the simulation domain, so we stop the simulation at that point. In addition, we find that the inclusion of a subsonically turbulent velocity field (see model Tur-Sub-0) does not produce any significant effect on the lateral width, velocity dispersion, and mean vorticity enhancement of the filament, in agreement with our qualitative analysis in the previous section. The subsonic turbulence in model Tur-Sub-0 also decays, but dissipation in this case occurs in small-scale eddies on the viscous scale.

The second largest effect on the above diagnostics is caused by turbulent magnetic fields. The stronger the magnetic field (i.e. the larger the magnetic pressure) in the cloud, the greater the magnetically driven expansion of filament gas. This is revealed by the curves of models Tur-Sub-0, Tur-Sub-Bwk, and Tur-Sub-Bst of Panels B1 and B2 of Fig. 9, which show that lateral widths become systematically larger as we increase the strength of the initial magnetic field threading the cloud. In the weak-field model, Tur-Sub-Bwk, magnetically driven expansion becomes important for $t/t_{cc} \geq 0.5$, producing lateral elongations up to ∼80 per cent (in the tail) and ∼25 per cent (in the footpoint) larger than in model Tur-Sub-0. In the strong-field model, Tur-Sub-Bst, the effect is more significant and occurs from the beginning of the interaction, producing lateral elongations ∼160 per cent (in the tail) and ∼50 per cent (in the footpoint) larger than in model Tur-Sub-0. Panel B2 also shows that the footpoint disruption of turbulent filaments occurs in a steadier manner than in their uniform counterpart (where an abrupt break up takes place at $t/t_{cc} = 1.0$). In case of velocity dispersions (Panels C1 and C2) and mean vorticity enhancements (Panels D1 and D2), we find that increasing the strength of the initially turbulent magnetic field produces different effects on the tails and footpoints of filaments. In the tails turbulent magnetic fields lead to velocity dispersions up to ∼60 per cent (in the weak-field case) and ∼80 per cent (in the strong-field case) higher than in model Tur-Sub-0; as well as to mean vorticity enhancements up to ∼100 per cent (in the weak-field case) and ∼180 per cent (in the strong-field case) greater than in model Tur-Sub-0. In the footpoints, on the other hand, there is no clear trend with increasing magnetic field strength. In the weak-field case both the velocity dispersions and vorticity enhancements are higher than in model Tur-Sub-0, whilst in the strong-field case both diagnostics decrease. We attribute this behaviour to the shielding effects that strong magnetic fields have on the footpoint of this filament, via suppression of gas mixing and enhancement of the clumping of cloud gas into dense knots and subfilaments (see a discussion on mixing fractions and clumping factors in Appendices F and G). These appendices show that the stronger the internal, turbulent magnetic field in the cloud, the lower the mixing fractions and the higher the clumping factors (in agreement with McCourt et al. 2015; cf. fig. 2 in that paper).

The third largest effect on the aforementioned diagnostics is produced by turbulent density distributions as they allow a faster percolation of wind-driven shocks through the porous medium of filaments. By comparing model Uni-0-0 with any of the turbulent models in Fig. 9, we find that the inclusion of turbulent density profiles in the initial conditions of clouds produces a rapid development of vortical motions inside the clouds, which result in the formation of highly turbulent, less confined filaments downstream (e.g. compare the curves of models Uni-0-0 and Tur-0-0 on the left-hand side panels for the tails and on the right-hand side panels for the footpoints of filaments in Fig. 9). Panels B1 and B2 show that the turbulent cloud of model Tur-0-0 produces a filament with tail elongations ∼20 per cent and footpoint elongations ∼70 per cent greater than in model Uni-0-0, whose cloud only expands after its break up at $t/t_{cc} = 1.0$. In addition, Panels C1 and C2 show that the turbulent cloud of model Tur-0-0 exhibits velocity dispersions ∼100 per cent larger than their uniform counterpart (model Uni-0-0) in both the tail and footpoint of the filament throughout the simulation. The values of all models only approach each other at the end of the simulation, when the abrupt break up of the uniform cloud leads to a more turbulent velocity distribution in this model. Panels D1 and D2 show a similar behaviour. Mean vorticity enhancements in the turbulent cloud of model Tur-0-0 are twice as high as in the uniform case, Uni-0-0, during most of the evolution in both tail and footpoint material.

4.2.3 *On the energy densities of the filaments*

Here, we examine how the different contributors to the total energy density in filaments evolve in different models. Fig. 10 shows the average energy densities, normalized with respect to the kinetic energy density of the wind, $E_{k,w}$, in tail (left-hand side column) and footpoint (right-hand side column) material separately.

Panels E1 and E2 of Fig. 10 indicate that the turbulent kinetic energy density in the tails and footpoints of turbulent filaments rises more rapidly than that of the uniform model. After the rapid increase observed in all models, the curves of the turbulent kinetic energy density flatten for $t/t_{cc} \geq 0.2$ and steadily decrease to reach $[E'_{k,tail}]/E_{k,w} \sim 0.1$ and $[E'_{k,footpoint}]/E_{k,w} \sim 0.2$ of the initial wind kinetic energy density in tail and footpoint material, respectively. Even when a supersonically turbulent velocity field is incorporated (see model Tur-Sup-0), the early-stage dissipation of turbulence into thermal energy that this cloud experiences leads to kinetic energy densities $[E'_{k,tail}]/E_{k,w} \sim [E'_{k,footpoint}]/E_{k,w} \sim 0.1$ in both the tail and footpoint of the filament. Panels E1 and E2 of Fig. 10 also show that the inclusion of a strong, turbulent magnetic field in the initial conditions (see model Tur-Sub-Bst) leads to the formation of a more laminar tail with lower kinetic energy densities, owing to the higher densities produced by magnetic confinement of cloud/filament gas. This is in agreement with our qualitative analysis reported in Sections 4.1.1 and 4.2.1, in which we showed that strong magnetic fields produce a denser, more clumped, more strongly magnetized, and less mixed filamentary tail than models with null or weak turbulent magnetic fields.

Panels F1 and F2 of Fig. 10 show that the turbulent magnetic energy density in both tail and footpoint material converges as time progresses in all models, regardless of the initial conditions. Models that are started without turbulent magnetic fields (i.e. models Uni-0-0, Tur-0-0, Tur-Sub-0, and Tur-Sup-0) develop turbulent magnetic field components on short time-scales ($t/t_{cc} < 0.1$) as a result of vortical motions rapidly arising in the interior of the cloud via wind-driven shock heating and dynamical instabilities. Except for the delay observed in model Uni-0-0 in Panel F2, the curves of models Uni-0-0, Tur-0-0, Tur-Sub-0, and Tur-Sup-0 evolve similarly to converge to $[E'_{m,tail}]/E_{k,w} \sim [E'_{m,footpoint}]/E_{k,w} \sim 0.02$–$0.03$ of the initial wind kinetic energy density in both tail and footpoint material. On the other hand, models that are started with turbulent magnetic fields (Tur-Sub-Bwk and Tur-Sub-Bst) show evidence of turbulence dissipation. In case of the tails (see Panel F1), dissipation of turbulent magnetic energy into thermal energy

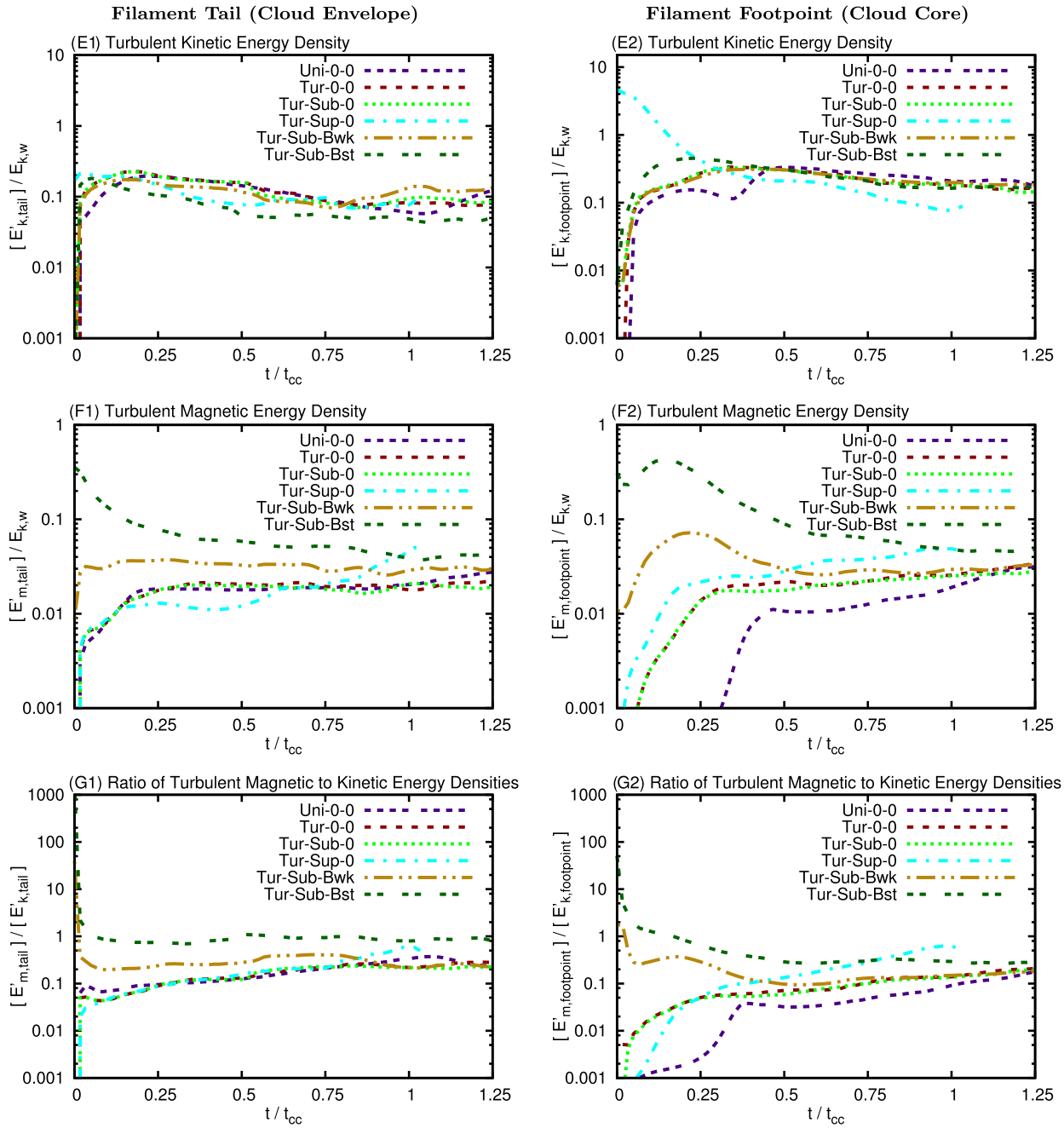

Figure 10. Same as Fig. 9, but here Panels E1 and E2 show the turbulent kinetic energy density, Panels F1 and F2 show the turbulent magnetic energy density, and Panels G1 and G2 show the evolution of the ratio of turbulent magnetic to turbulent kinetic energy densities, in the tails (left-hand side column) and footpoints (right-hand side column) of filaments. We find that: (a) regardless of the model, as the simulations progress, the ratio of turbulent magnetic to turbulent kinetic energy densities becomes constant in all models with $[E'_{\mathrm{m},\alpha}]/[E'_{\mathrm{k},\alpha}] \sim 0.25$–$0.75$, confirming subequipartition, and (b) strong magnetic fields produce magnetically confined filaments.

occurs from the very beginning of the simulations, while in case of the footpoints (see Panel F2), dissipation is delayed by the initial compression of field lines in the cores of these clouds, leading to a transient enhancement of their turbulent magnetic energy density. At the end of the simulation, however, the magnetic energy densities of the footpoints in models Tur-Sup-Bwk and Tur-Sup-Bst also approach $[E'_{\mathrm{m,tail}}]/E_{\mathrm{k,w}} \sim [E'_{\mathrm{m,footpoint}}]/E_{\mathrm{k,w}} \sim 0.03$–$0.04$. Overall, Panels F1 and F2 of Fig. 10 show that weakly magnetized filaments reach magnetic saturation as a result of the turbulent twisting, stretching, and folding of the magnetic field lines being stopped by large Lorentz forces, while in strongly magnetized filaments these forces are already large at the beginning of the interaction, so they lead to dissipation of magnetic energy into thermal energy and consequently to cloud expansion.

We also find that the effects of turbulent magnetic fields on the formation and evolution of filaments are more dependent on the

strength than on the topology of the initial, turbulent magnetic fields. In Banda-Barragán (2016), we showed that the presence of a very weak, turbulent magnetic field (with $[\beta_{\rm tu}] = 100$) inside the cloud has little impact on the evolution of the turbulent energy densities in the resulting filament, and here we show that systematically increasing the strength of the turbulent magnetic field to $[\beta_{\rm tu}] = 4$ first (in model Tur-Sub-Bwk) and then to $[\beta_{\rm tu}] = 0.04$ (in model Tur-Sub-Bst) with the same topology leads to increasing shielding effects on the cloud and higher turbulent energy densities. The stronger the initially turbulent magnetic field, the longer its dissipation timescale and the higher its impact on the dynamics and energetics of the clouds and filaments. For example, in core material (Panel F2), we find that the turbulent magnetic energy densities of models Tur-0-0, Tur-Sub-0, and Tur-Sub-Bwk converge to $[E'_{\rm m,footpoint}]/E_{\rm k,w} \sim 0.03$ at $t/t_{\rm cc} \sim 0.4$. This is much earlier than the time it takes for the turbulent magnetic energy to dissipate in model Tur-Sub-Bst, which only approaches the magnetic energy densities of models Tur-0-0 and Tur-Sub-0 at the end of the interaction (i.e. for $t/t_{\rm cc} \geq 1$). Thus, our models indicate that the tangling of the initially turbulent magnetic field lines in the cloud is insufficient to modify the kinetic and magnetic properties of the filament by itself. The fast growth of vortical motions in models with solely the oblique, uniform magnetic field (e.g. models Tur-0-0 and Tur-Sub-0), rapidly leads to the formation of a turbulent field with similar energy densities to the magnetic field prescribed for model Tur-Sub-Bwk after $t/t_{\rm cc} > 0.4$. The evolution of model Tur-Sub-Bst shows, on the other hand, that if the initial turbulent magnetic field is also strong, the additional magnetic pressure provided to the cloud produces a filament with less turbulent motions and higher magnetic fluctuations (strongly magnetized subfilaments and knots) than its counterparts.

Based on the above results, we investigate now the evolution of the ratio of turbulent magnetic to turbulent kinetic energy densities in both the tails and footpoints of filaments (see Panels G1 and G2 of Fig. 10, respectively). This is an important quantity in observations of magnetic clouds and filaments in the ISM, where the kinetic properties of these structures are measured from e.g. emission/absorption line profiles, but the strength of the total magnetic field is unknown or poorly constrained. Overall, Panels G1 and G2 show similar trends for both tails and filaments, with ratios of turbulent magnetic to turbulent kinetic energy densities converging to values $[E'_{{\rm m},\alpha}]/[E'_{{\rm k},\alpha}] \sim 0.25$–$0.75$ in all models after $t/t_{\rm cc} = 0.4$. This is similar to the range found in our models with the M configuration, i.e. $[E'_{{\rm m},\alpha}]/[E'_{{\rm k},\alpha}] \sim 0.1$–$0.4$ (see Section 4.1.3). Models with supersonically turbulent velocity and/or strong, turbulent magnetic fields favour the upper limits of these ranges, while models with uniform clouds favour the lower limits. The overall result, however, indicates that wind-swept clouds always evolve into stages at which the turbulent magnetic energy density is in subequipartition with respect to the turbulent kinetic energy density, regardless of the initial conditions.

4.2.4 On the cloud/filament dynamics

As mentioned above, turbulent clouds are more easily expanded by turbulence dissipation and shock heating than uniform clouds. In Section 4.1.4, we showed that this causes turbulent clouds to accelerate more rapidly than uniform clouds, owing to their larger cross-sectional areas. Here, we complement our previous conclusions by investigating the role of different turbulent densities, velocities, and magnetic fields on the dynamics of clouds, separately. Fig. 11 shows the displacement of the centre of mass (Panels H1 and H2) and the bulk velocity (Panel I1 and I2) of tails (left-hand side column) and footpoints (right-hand side column) in different models as a function of time. These panels indicate that the inclusion of turbulence radically changes our expectations on the dynamics of wind-swept clouds. In agreement with our results presented in Section 4.2.2, we find here that supersonically turbulent velocity fields produce the largest effect on the displacement of the centre of mass and the bulk speed of clouds/filaments. The fast expansion experienced by this cloud leads to an increased cross-sectional area and consequently to an enhanced drag force, which accelerates the cloud to higher velocities and allows it to reach farther distances than in other models. Both the tail and footpoint of the filament in model Tur-Sup-0 travel distances three times larger than in model Uni-0-0 and 50 per cent larger than in model Tur-Sub-Bst (see Panels H1 and H2), and acquire bulk speeds five times greater than in any other model.

The second largest effect on the parameters of Fig. 11 is produced by strong, turbulent magnetic fields as they also have the ability to expand the cross-sectional area of the cloud (see Section 4.2.2). In model Tur-Sub-Bst, both the tail and footpoint of the filament travel distances 30 per cent larger than in model Uni-0-0 and 20 per cent larger than in model Tur-0-0 (see Panels H1 and H2), and acquire bulk speeds 50 per cent–70 per cent greater than in model Uni-0-0 and $10-20$ per cent greater than in model Tur-0-0 (see Panels I1 and I2). The third largest effect on the dynamics of filaments is produced by turbulent density distributions, which allow wind-driven shocks to move more easily through cloud material, thus expanding it more than in the uniform cloud model. In model Tur-0-0, both the tail and footpoint of the filament travel distances 30 per cent larger than in model Uni-0-0 (see Panels H1 and H2), and acquire bulk speeds 60 per cent greater than in model Uni-0-0 (see Panels I1 and I2). Note also that the inclusion of a subsonically turbulent velocity field (in model Tur-Sub-0) and of a weak, turbulent magnetic field (in model Tur-Sub-Bwk) does not produce significant effects on the filament dynamics.

Overall, the above results and the ones presented in previous sections show that self-consistently adding turbulence to wind–cloud systems enhances cloud acceleration without hastening its disruption. Since the main driver of the cloud dynamics is the supersonic wind, the turbulence-driven increase of the cross-sectional area in turbulent cloud models results in a higher effective drag force on these clouds. Thus, in turbulent models the wind is able to transport cold, dense clouds/filaments over distances at least twice as large as the distance travelled by uniform clouds. These entrained structures also travel at least 50 per cent faster than uniform clouds.

5 CAVEATS AND LIMITATIONS

An important note regarding the self-consistency of the turbulent models presented in this paper is that in all models (but one, i.e. model TUR-SUP-BST-ISO, which is fully self-consistent), we take the original distributions of density, velocity, and magnetic fields from Federrath & Klessen (2012), but (1) we use an adiabatic index of $\gamma = \frac{5}{3}$ (as opposed to an isothermal index; see model TUR-SUP-BST), and (2) we re-scale the mean values of the distributions to pre-defined target values (see models Tur-0-0, Tur-Sub-0, Tur-Sup-0, Tur-Sub-Bwk, and Tur-Sub-Bst), specifically chosen so that we can compare them with the results presented in Paper I and conduct a systematic study over different turbulence parameters. Hence, the adiabatic turbulent models described in this paper do preserve the original distribution function of these fields, but they are only partially self-consistent (e.g. scaling the turbulent velocity field to a different target Mach number would result in changes in the density

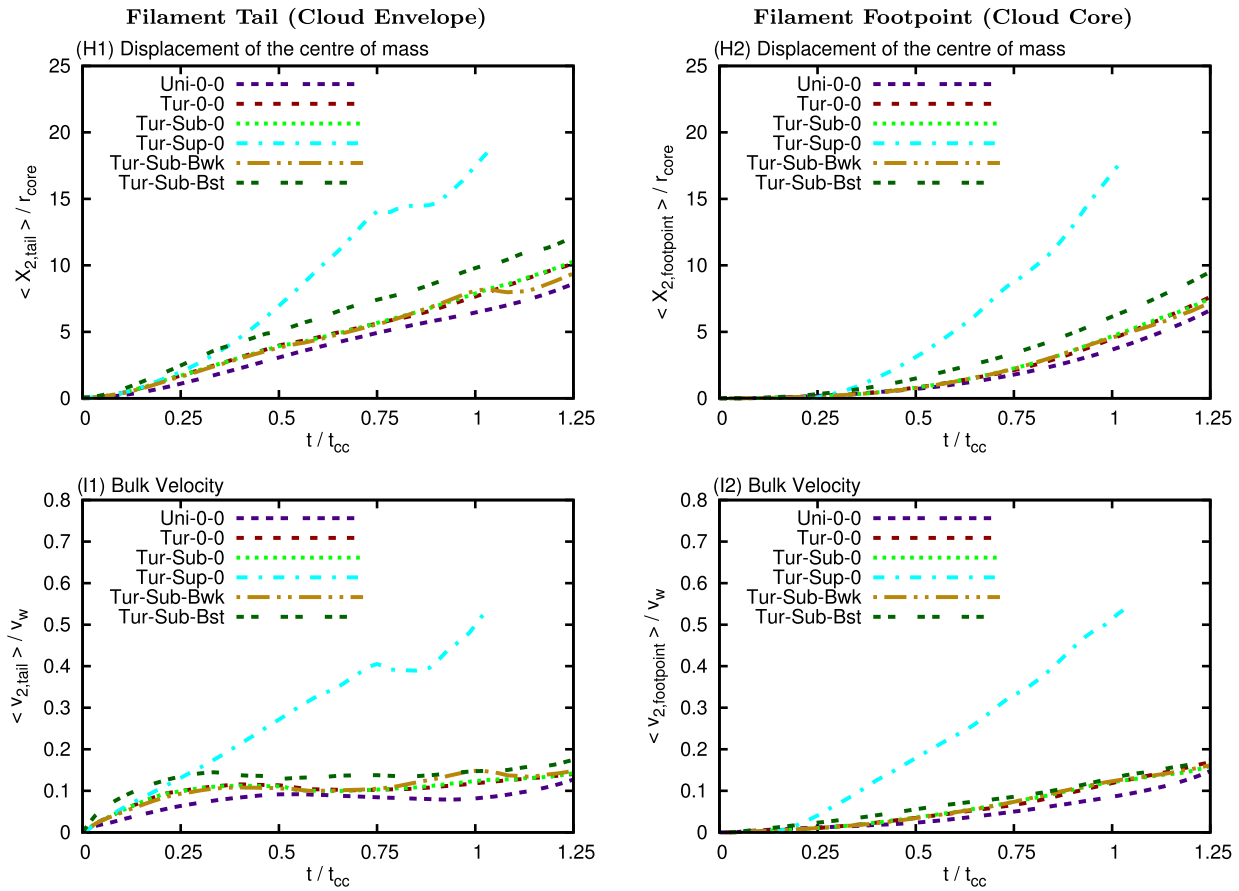

Figure 11. Same as Figs 9 and 10, but here Panels H1 and H2 show the displacement of the centre of mass and Panels I1 and I2 show the bulk velocity (in the direction of streaming) of the tails (left-hand side column) and footpoints (right-hand side column) of wind-swept clouds (filaments) entrained in the wind. We find that turbulence and magnetic fields alter the dynamics of filaments. Supersonic velocity fields produce the largest effect, followed by strong magnetic fields, and then by turbulent density distributions, owing to enhanced cross-sectional areas in all cases.

and magnetic field distributions as well, and this is not accounted for in the adiabatic models presented here). Despite this, the turbulent simulations presented in this paper: (1) are more realistic than any previous model used to describe wind–cloud systems in the ISM, (2) are designed so that they can be used to study a wide parameter space and analyse how different turbulence parameters for the cloud affect the dynamics and morphology of filaments, and (3) form the basis for more sophisticated models (currently in preparation) of fully radiative, self-consistent, turbulent clouds being swept up by supersonic winds.

6 SUMMARY AND CONCLUDING REMARKS

We have presented a detailed numerical study of the formation of filamentary structures arising from the interplay between supersonic winds and turbulent clouds in the ISM. We have expanded our previous work (see Paper I) by incorporating clouds with turbulent density, velocity, and magnetic fields. The aim of this work is to investigate how the inclusion of turbulence affects the formation, morphology, and dynamics of filaments, and in particular how the strength and topology of the magnetic field in and around wind-swept clouds changes when the magnetic field in the cloud is self-contained and turbulent. We summarize the main conclusions of our study below:

(i) Our results show that the mechanism by which turbulent clouds are disrupted to form filaments is a universal process. Filaments are composed of two substructures, namely tails and footpoints, which evolve in a similar fashion in both uniform and turbulent cloud models. The evolution of wind-swept clouds involves four phases: (1) A tail formation phase in which material, stripped from the sides and the interior of the cloud, is transported to the rear side of the cloud to form an elongated tail, (2) A tail erosion phase in which KH instabilities at the wind–filament interface continuously re-shape the morphology of the tail, (3) A footpoint dispersion phase characterized by dense regions in the cloud being disrupted by RT unstable modes; and (4) A free-floating phase in which subfilaments and cloudlets become entrained in the wind. Movies showing the full-time evolution of the models presented in Figs 2, 3, 4, and 8 are available online[4].

(ii) The inclusion of turbulence in the initial conditions for the clouds produces several effects on the morphology, energetics, and dynamics of the resulting filaments. Turbulent clouds result in the formation of filaments with lower aspect (length-to-width) ratios, larger lateral widths ($\iota_{1,\mathrm{filament}}/\iota_{1,\mathrm{filament},0} \sim 5$), higher

[4] https://goo.gl/iXgJYk

transverse velocity dispersions ($\delta_{v_{\rm filament}}/v_{\rm w} \sim 0.06$), and higher vorticity enhancements than those arising from uniform clouds. The evolution of the turbulent energy densities also differs in turbulent and uniform cloud models. While turbulent clouds undergo a short period ($t/t_{\rm cc} < 0.2$) of dissipation of their turbulent energy into thermal energy, a uniform cloud experiences the opposite effect, rapidly becoming turbulent over similar time-scales (i.e. for $t/t_{\rm cc} < 0.2$). After this time, both the kinetic and magnetic energy densities in all models saturate until the end of the evolution and maintain a fixed ratio of $[E'_{\rm m,filament}]/[E'_{\rm k,filament}] \sim 0.1$–$0.4$. This indicates that the magnetic energy density in wind-swept clouds is in subequipartition with respect to the turbulent kinetic energy density. The near universality of $[E'_{\rm m}]/[E'_{\rm k}]$ found here may be used to infer magnetic field strengths from measuring the line widths of wind-swept clouds and filaments in observations.

(iii) Regarding the dynamics of wind-swept clouds, we have shown that the self-consistent inclusion of turbulent density, velocity, and magnetic fields in the initial conditions for clouds produces significant effects on the displacement of the centre of mass and the bulk velocity (in the streaming direction) of the filaments. Turbulence aids cloud expansion and effectively increases the cross-sectional area upon which the wind ram-pressure force acts. The enhanced drag force accelerates turbulent clouds more than in uniform cloud models, allowing them to travel distances of $\langle X_{2,\rm filament}\rangle/r_{\rm core} \sim 15$–$20$ and reach bulk speeds of $\langle v_{2,\rm filament}\rangle/v_{\rm w} \sim 0.3 - 0.4$ by $t/t_{\rm cc} = 1.0$, which are both three times larger than the distances and bulk speeds acquired by uniform clouds over the same time-scales.

(iv) Considering the systematic inclusion of turbulent density, velocity, and magnetic fields, we find that a turbulent density profile allows the wind-driven shocks to propagate faster through low-density regions in the cloud, thus producing a rapid development of vortical motions. This results in the formation of more turbulent and less confined filaments than in uniform modes. Filamentary tails in turbulent models consist of a collection of knots and subfilaments, rather than of a single structure as in uniform models. The inclusion of turbulent velocity fields in the clouds has varying effects on the global evolution of filaments. When a subsonically turbulent velocity field is considered, we find no significant effect on the evolution compared to models with null velocity fields. On the other hand, when a supersonically turbulent velocity field is considered, the cloud undergoes a fast expansion phase, as a result of the turbulence-crossing time-scale being lower than the dynamical, cloud-crushing time-scale of the system.

(v) The role of a turbulent magnetic field on the morphology and dynamics of wind-swept clouds highly depends on its initial strength. The stronger the initial magnetic field, the greater the suppression of KH instabilities at wind–cloud interfaces and the enhancement of RT instabilities at the front of the cloud. The presence of turbulent magnetic fields also triggers cloud expansion (thus aiding cloud acceleration) and enhances the internal vorticity of the filamentary tails (thus aiding clumping and subfilamentation), but it also keeps the cloud protected from disruption. Turbulent magnetic fields shield the cloud from the disruptive effects of dynamical instabilities, which prevents the fast stripping of cloud material and reduces the mixing of wind and cloud gas. The ability of cloud gas to radiate its energy away and keep itself cool also produces shielding effects on the resulting filament, as our fully self-consistent model with a softer (nearly isothermal) equation of state shows. In this case, the cloud remains dense and keeps its turbulent magnetic energy density high at all times. The resulting high-density contrast and the strong magnetic tension at wind–cloud interfaces suppress KH instabilities, enhance flow laminarity, and aid cloud survival in the supersonic wind.

(vi) Our simulations reveal that filaments produced in ISM wind–cloud interactions are expected to have similar magnetic field strengths as their progenitor clouds. We have shown that the ratio of magnetic energy density in the filament to the initial magnetic energy density in the cloud remains constant $\sim$1 over the entire evolution of models that include self-consistently strong, turbulent magnetic fields. The regions with the highest magnetic energy densities in turbulent models are the knots and subfilaments (i.e. the anisotropies) along their tails. The fact that filaments arising from turbulent clouds with strong magnetic fields remain highly magnetized as the simulations progress provides a numerical basis for observations of ISM filaments with similar magnetic field strengths as the clouds that potentially originated them.

(vii) Overall, we conclude that introducing turbulence in a self-consistent manner is crucial to understanding entrainment of high density, cold gas in low density, hot winds and outflows. Our simulations show that both the porosity of the turbulent density field and its corresponding turbulent velocity field enhance cloud acceleration via dissipation of supersonic turbulence, while at the same time the strong, turbulent magnetic field prevents cloud ablation by shielding the cloud from dynamical shredding. In other words, turbulent clouds produce filaments with anisotropic substructures that travel faster and reach larger distances than uniform clouds, without being fully disrupted in the process. This is particularly important for explaining the presence of high-latitude dense gas embedded in hot galactic outflows as our simulations show that wind-swept clouds are able to survive disruption aided by turbulence, magnetic fields, and radiative cooling much longer than suggested by previous models.

(viii) Finally, we determine the required numerical resolution and domain size needed to obtain converged results (see Appendices A and B). We find that our chosen resolutions of R_{64} and R_{128} for our computational domain configurations M and S, respectively, adequately capture the evolution of wind-swept uniform and turbulent clouds for the parameter space explored in this series of papers.

ACKNOWLEDGEMENTS

We thank Ross Parkin, Cornelia Lang, Naomi McClure-Griffiths, and Helga Denés for insightful discussions on the numerical setups and on the potential applications of the simulations presented here, and the anonymous referee for their comments which helped improve this work. WBB thanks the National Secretariat of Higher Education, Science, Technology, and Innovation of Ecuador (SENESCYT) for funding this project through a doctoral scholarship (CI:1711298438), and the Ecuadorian Network for Research and Education (RED CEDIA) for providing access to local computational resources. WBB is the recipient of the Olin Eggen Scholarship at Mount Stromlo Observatory. CF acknowledges funding provided by the Australian Research Council's Discovery Projects (grants DP130102078 and DP150104329). RMC is the recipient of an Australian Research Council Future Fellowship (FT110100108). This research was supported by the National Computational Infrastructure at Australian National University and the Pawsey Supercomputing Centre, with funding from the Australian Government and the Government of Western Australia, through grants n72 and ek9. CF thanks for high-performance

computing resources provided by the Leibniz Rechenzentrum and the Gauss Centre for Supercomputing (grants pr32lo, pr48pi, and Gauss Centre for Supercomputing Large-scale project 10391), and the Partnership for Advanced Computing in Europe (PRACE grant pr89mu). The 3D plots and movies reported in this series of papers were generated using the VISIT visualization software (Childs et al. 2012).

REFERENCES

Abramson A., Kenney J. D. P., 2014, AJ, 147, 63
Alūzas R., Pittard J. M., Hartquist T. W., Falle S. A. E. G., Langton R., 2012, MNRAS, 425, 2212
Alūzas R., Pittard J. M., Falle S. A. E. G., Hartquist T. W., 2014, MNRAS, 444, 971
Armillotta L., Fraternali F., Werk J. K., Prochaska J. X., Marinacci F., 2017, MNRAS, 470, 114
Ballone A. et al., 2013, ApJ, 776, 13
Ballone A. et al., 2016, ApJ, 819, L28
Banda-Barragán W. E., 2016, PhD thesis, Research School of Astronomy and Astrophysics, Australian National University
Banda-Barragán W. E., Parkin E. R., Federrath C., Crocker R. M., Bicknell G. V., 2016, MNRAS, 455, 1309
Batchelor G. K., 2000, An Introduction to Fluid Dynamics. Cambridge Univ. Press, Cambridge, UK
Benedettini M. et al., 2015, MNRAS, 453, 2036
Bhat P., Subramanian K., Brandenburg A., 2016, MNRAS, 461, 240
Bicknell G. V., Li J., 2001, PASA, 18, 431
Bland J., Tully B., 1988, Nature, 334, 43
Bland-Hawthorn J., Cohen M., 2003, ApJ, 582, 246
Brandenburg A., Subramanian K., 2005, Phys. Rep., 417, 1
Brüggen M., Scannapieco E., 2016, ApJ, 822, 31
Brunt C. M., Heyer M. H., Mac Low M.-M., 2009, A&A, 504, 883
Burkert A., Schartmann M., Alig C., Gillessen S., Genzel R., Fritz T. K., Eisenhauer F., 2012, ApJ, 750, 58
Calderón D., Ballone A., Cuadra J., Schartmann M., Burkert A., Gillessen S., 2016, MNRAS, 455, 4388
Carlqvist P., Gahm G. F., Kristen H., 2003, A&A, 403, 399
Carral P., Hollenbach D. J., Lord S. D., Colgan S. W. J., Haas M. R., Rubin R. H., Erickson E. F., 1994, ApJ, 423, 223
Cecil G., Bland-Hawthorn J., Veilleux S., 2002, ApJ, 576, 745
Chandrasekhar S., 1961, Hydrodynamic and Hydromagnetic Stability. Clarendon, Oxford
Chevalier R. A., Clegg A. W., 1985, Nature, 317, 44
Childs H. et al., 2012, in Bethel E. W., Childs H., Hansen C., eds, High Performance Visualization–Enabling Extreme-Scale Scientific Insight. CRC Press Taylor & Francis, Boca Raton, FL, p. 357
Chynoweth K. M., Langston G. I., Yun M. S., Lockman F. J., Rubin K. H. R., Scoles S. A., 2008, AJ, 135, 1983
Cooper J. L., Bicknell G. V., Sutherland R. S., Bland-Hawthorn J., 2008, ApJ, 674, 157
Cooper J. L., Bicknell G. V., Sutherland R. S., Bland-Hawthorn J., 2009, ApJ, 703, 330
Cowling T. G., 1976, Magnetohydrodynamics. Hilger, London
Crawford C. S., Hatch N. A., Fabian A. C., Sanders J. S., 2005, MNRAS, 363, 216
Crutcher R. M., Wandelt B., Heiles C., Falgarone E., Troland T. H., 2010, ApJ, 725, 466
Dahlburg R. B., Einaudi G., LaRosa T. N., Shore S. N., 2002, ApJ, 568, 220
Davidson P. A., 2004, Turbulence: An Introduction for Scientists and Engineers. Oxford Univ. Press, Oxford, UK
Dedner A., Kemm F., Kröner D., Munz C.-D., Schnitzer T., Wesenberg M., 2002, J. Comput. Phys., 175, 645
Dgani R., Walder R., Nussbaumer H., 1993, A&A, 267, 155
Drazin P. G., 1970, J. Fluid Mech., 42, 321
Drazin P. G., 2002, Introduction to Hydrodynamic Stability. Cambridge Univ. Press, Cambridge, UK
Drazin P. G., Reid W. H., 2004, Hydrodynamic Stability. Cambridge Univ. Press, Cambridge, UK
Elmegreen B. G., Scalo J., 2004, ARA&A, 42, 211
Enokiya R. et al., 2014, ApJ, 780, 72
Federrath C., 2013, MNRAS, 436, 1245
Federrath C., Banerjee S., 2015, MNRAS, 448, 3297
Federrath C., Klessen R. S., 2012, ApJ, 761, 156
Federrath C., Klessen R. S., Schmidt W., 2008, ApJ, 688, L79
Federrath C., Roman-Duval J., Klessen R. S., Schmidt W., Mac Low M.-M., 2010, A&A, 512, A81
Federrath C., Schober J., Bovino S., Schleicher D. R. G., 2014, ApJ, 797, L19
Ferrière K. M., 2001, Rev. Mod. Phys., 73, 1031
Ferrière K., 2007, in Miville-Deschênes M.-A., Boulanger F., eds, EAS Publ. Ser. Vol. 23, Theoretical Introduction to Galactic Magnetic Fields. Cambridge Univ. Press, Cambridge, p. 3
Ferrière K., 2011, Mem. Soc. Astron. Ital., 82, 824
Field G. B., 1965, ApJ, 142, 531
Fragile P. C., Murray S. D., Anninos P., van Breugel W., 2004, ApJ, 604, 74
Fragile P. C., Anninos P., Gustafson K., Murray S. D., 2005, ApJ, 619, 327
Frank A., Jones T. W., Ryu D., Gaalaas J. B., 1996, ApJ, 460, 777
Gaensler B. M. et al., 2011, Nature, 478, 214
Gardiner T. A., Stone J. M., 2005, J. Comput. Phys., 205, 509
Gardiner T. A., Stone J. M., 2008, J. Comput. Phys., 227, 4123
Gillessen S. et al., 2012, Nature, 481, 51
Gillessen S. et al., 2013, ApJ, 763, 78
Goldsmith K. J. A., Pittard J. M., 2016, MNRAS, 461, 578
Goldsmith K. J. A., Pittard J. M., 2017, MNRAS, 470, 2427
Goodson M. D., Heitsch F., Eklund K., Williams V. A., 2017, MNRAS, 468, 3184
Gregori G., Miniati F., Ryu D., Jones T. W., 1999, ApJ, 527, L113
Gregori G., Miniati F., Ryu D., Jones T. W., 2000, ApJ, 543, 775
Greve A., 2004, A&A, 416, 67
Grønnow A., Tepper-García T., Bland-Hawthorn J., McClure-Griffiths N. M., 2017, ApJ, 845, 69
Heckman T. M., Thompson T. A., 2017, in Alsabti A. W., Murdin P., eds, Handbook of Supernovae, Springer International Publishing, p. 1
Heiles C., 2004, in Johnstone D., Adams F. C., Lin D. N. C., Neufeeld D. A., Ostriker E. C., eds, ASP Conf. Ser. Vol. 323, Star Formation in the Interstellar Medium: In Honor of David Hollenbach. Astron. Soc. Pac., San Francisco, p. 79
Heiles C., Troland T. H., 2003, ApJ, 586, 1067
Hennebelle P., Falgarone E., 2012, A&A Rev., 20, 55
Hester J. J. et al., 1996, ApJ, 456, 225
Higdon J. C., Lingenfelter R. E., Rothschild R. E., 2009, ApJ, 698, 350
Hopkins P. F., 2013, MNRAS, 430, 1880
Inoue T., Inutsuka S.-i., 2012, ApJ, 759, 35
Johansson E. P. G., Ziegler U., 2013, ApJ, 766, 45
Jones T. W., Kang H., Tregillis I. L., 1994, ApJ, 432, 194
Jones T. W., Ryu D., Tregillis I. L., 1996, ApJ, 473, 365
Jun B.-I., Norman M. L., Stone J. M., 1995, ApJ, 453, 332
Kainulainen J., Beuther H., Henning T., Plume R., 2009, A&A, 508, L35
Kainulainen J., Federrath C., Henning T., 2013, A&A, 553, L8
Kainulainen J., Federrath C., Henning T., 2014, Science, 344, 183
Kenney J. D. P., Abramson A., Bravo-Alfaro H., 2015, AJ, 150, 59
Klein R. I., McKee C. F., Colella P., 1994, ApJ, 420, 213
Konstandin L., Girichidis P., Federrath C., Klessen R. S., 2012, ApJ, 761, 149
Koo B.-C., Moon D.-S., Lee H.-G., Lee J.-J., Matthews K., 2007, ApJ, 657, 308
Kornreich P., Scalo J., 2000, ApJ, 531, 366
Kronberger T., Kapferer W., Ferrari C., Unterguggenberger S., Schindler S., 2008, A&A, 481, 337
Krumholz M. R., Kruijssen J. M. D., 2015, MNRAS, 453, 739
Krumholz M. R., Thompson T. A., 2012, ApJ, 760, 155

Krumholz M. R., Thompson T. A., 2013, MNRAS, 434, 2329
Krumholz M. R., Kruijssen J. M. D., Crocker R. M., 2017, MNRAS, 466, 1213
Kuncic Z., Bicknell G. V., 2004, ApJ, 616, 669
Lang C. C., Anantharamaiah K. R., Kassim N. E., Lazio T. J. W., 1999, ApJ, 521, L41
LaRosa T. N., Kassim N. E., Lazio T. J. W., Hyman S. D., 2000, AJ, 119, 207
LaRosa T. N., Nord M. E., Lazio T. J. W., Kassim N. E., 2004, ApJ, 607, 302
Larson R. B., 1981, MNRAS, 194, 809
Lazarian A., 2014, Space Sci. Rev., 181, 1
Lazarian A., Vishniac E. T., 1999, ApJ, 517, 700
Leão M. R. M., de Gouveia Dal Pino E. M., Falceta-Gonçalves D., Melioli C., Geraissate F. G., 2009, MNRAS, 394, 157
Leão M. R. M., de Gouveia Dal Pino E. M., Santos-Lima R., Lazarian A., 2013, ApJ, 777, 46
Lecoanet D. et al., 2016, MNRAS, 455, 4274
Lehnert M. D., Heckman T. M., Weaver K. A., 1999, ApJ, 523, 575
Li S., Frank A., Blackman E. G., 2013, ApJ, 774, 133
Lockman F. J., McClure-Griffiths N. M., 2016, ApJ, 826, 215
Mac Low M.-M., Klessen R. S., 2004, Rev. Mod. Phys., 76, 125
Mac Low M.-M., McKee C. F., Klein R. I., Stone J. M., Norman M. L., 1994, ApJ, 433, 757
Mac Low M.-M., Toraskar J., Oishi J. S., Abel T., 2007, ApJ, 668, 980
Mackey J., Lim A. J., 2010, MNRAS, 403, 714
Marcolini A., Brighenti F., D'Ercole A., 2003, MNRAS, 345, 1329
Martin C. L., 2005, ApJ, 621, 227
Matsubayashi K., Sugai H., Hattori T., Kawai A., Ozaki S., Kosugi G., Ishigaki T., Shimono A., 2009, ApJ, 701, 1636
McClure-Griffiths N. M., Dickey J. M., Gaensler B. M., Green A. J., Green J. A., Haverkorn M., 2012, ApJS, 199, 12
McClure-Griffiths N. M., Green J. A., Hill A. S., Lockman F. J., Dickey J. M., Gaensler B. M., Green A. J., 2013, ApJ, 770, L4
McCourt M., O'Leary R. M., Madigan A.-M., Quataert E., 2015, MNRAS, 449, 2
McCourt M., Oh S. P., O'Leary R. M., Madigan A.-M., 2016, preprint (arXiv:1610.01164)
McEntaffer R. L., Grieves N., DeRoo C., Brantseg T., 2013, ApJ, 774, 120
McKee C. F., Ostriker E. C., 2007, ARA&A, 45, 565
Melioli C., de Gouveia dal Pino E. M., Raga A., 2005, A&A, 443, 495
Melioli C., de Gouveia Dal Pino E. M., de La Reza R., Raga A., 2006, MNRAS, 373, 811
Melioli C., Brighenti F., D'Ercole A., de Gouveia Dal Pino E. M., 2008, MNRAS, 388, 573
Melioli C., Brighenti F., D'Ercole A., de Gouveia Dal Pino E. M., 2009, MNRAS, 399, 1089
Melioli C., de Gouveia Dal Pino E. M., Geraissate F. G., 2013, MNRAS, 430, 3235
Mellema G., Kurk J. D., Röttgering H. J. A., 2002, A&A, 395, L13
Mellema G., Arthur S. J., Henney W. J., Iliev I. T., Shapiro P. R., 2006, ApJ, 647, 397
Mignone A., Tzeferacos P., 2010, J. Comput. Phys., 229, 2117
Mignone A., Bodo G., Massaglia S., Matsakos T., Tesileanu O., Zanni C., Ferrari A., 2007, ApJS, 170, 228
Mignone A., Tzeferacos P., Bodo G., 2010, J. Comput. Phys., 229, 5896
Mignone A., Zanni C., Tzeferacos P., van Straalen B., Colella P., Bodo G., 2012, ApJS, 198, 7
Miniati F., Ryu D., Ferrara A., Jones T. W., 1999a, ApJ, 510, 726
Miniati F., Jones T. W., Ryu D., 1999b, ApJ, 517, 242
Miyoshi T., Kusano K., 2005, J. Chem. Phys., 208, 315
Molina F. Z., Glover S. C. O., Federrath C., Klessen R. S., 2012, MNRAS, 423, 2680
Monceau-Baroux R., Keppens R., 2017, A&A, 600, A134
Morris M., Yusef-Zadeh F., 1985, AJ, 90, 2511
Morris M. R., Zhao J.-H., Goss W. M., 2014, in Sjouwerman L. O., Lang C. C., Ott J., eds, IAU Symp. Vol. 303. The Galactic Center: Feeding and Feedback in a Normal Galactic Nucleus, Santa Fe, United States, p. 369
Mouri H., Takaoka M., Hori A., Kawashima Y., 2002, Phys. Rev. E, 65, 056304
Murray S. D., White S. D. M., Blondin J. M., Lin D. N. C., 1993, ApJ, 407, 588
Murray N., Quataert E., Thompson T. A., 2005, ApJ, 618, 569
Nakamura F., McKee C. F., Klein R. I., Fisher R. T., 2006, ApJS, 164, 477
Niederhaus J. H. J., 2007, PhD thesis, The University of Wisconsin - Madison
Nittmann J., Falle S. A. E. G., Gaskell P. H., 1982, MNRAS, 201, 833
Nolan C. A., Federrath C., Sutherland R. S., 2015, MNRAS, 451, 1380
Nordlund Å. K., Padoan P., 1999, in Franco J., Carraminana A., eds, Interstellar Turbulence. Cambridge Univ. Press, Cambridge, p. 218
Nynka M. et al., 2015, ApJ, 800, 119
Orlando S., Peres G., Reale F., Bocchino F., Rosner R., Plewa T., Siegel A., 2005, A&A, 444, 505
Orlando S., Bocchino F., Peres G., Reale F., Plewa T., Rosner R., 2006, A&A, 457, 545
Orlando S., Bocchino F., Reale F., Peres G., Pagano P., 2008, ApJ, 678, 274
Ossenkopf V., Mac Low M.-M., 2002, A&A, 390, 307
Padoan P., Nordlund Å., 1999, ApJ, 526, 279
Padoan P., Nordlund A., Jones B. J. T., 1997, MNRAS, 288, 145
Padoan P., Federrath C., Chabrier G., Evans II N. J., Johnstone D., Jørgensen J. K., McKee C. F., Nordlund Å., 2014, Protostars and Planets VI. University of Arizona Press, Tucson, AZ, p. 77
Parkin E. R., 2014, MNRAS, 438, 2513
Parkin E. R., Pittard J. M., Corcoran M. F., Hamaguchi K., 2011, ApJ, 726, 105
Passot T., Vázquez-Semadeni E., 1998, Phys. Rev. E, 58, 4501
Patnaude D. J., Fesen R. A., 2009, ApJ, 697, 535
Pfrommer C., Dursi J., 2010, Nat. Phys., 6, 520
Pietarila Graham J., Danilovic S., Schüssler M., 2009, ApJ, 693, 1728
Pittard J. M., 2011, MNRAS, 411, L41
Pittard J. M., Goldsmith K. J. A., 2016, MNRAS, 458, 1139
Pittard J. M., Parkin E. R., 2016, MNRAS, 457, 4470
Pittard J. M., Dyson J. E., Falle S. A. E. G., Hartquist T. W., 2005, MNRAS, 361, 1077
Pittard J. M., Falle S. A. E. G., Hartquist T. W., Dyson J. E., 2009, MNRAS, 394, 1351
Pittard J. M., Hartquist T. W., Falle S. A. E. G., 2010, MNRAS, 405, 821
Pittard J. M., Hartquist T. W., Dyson J. E., Falle S. A. E. G., 2011, Ap&SS, 336, 239
Poludnenko A. Y., Frank A., Blackman E. G., 2002, ApJ, 576, 832
Price D. J., Federrath C., Brunt C. M., 2011, ApJ, 727, L21
Proga D., Waters T., 2015, ApJ, 804, 137
Raga A., Steffen W., González R., 2005, Rev. Mex. Astron. Astrofis., 41, 45
Raga A. C., Esquivel A., Riera A., Velázquez P. F., 2007, ApJ, 668, 310
Raga A. C., Henney W., Vasconcelos J., Cerqueira A., Esquivel A., Rodríguez-González A., 2009, MNRAS, 392, 964
Redfield S., Linsky J. L., 2004, ApJ, 613, 1004
Roberts D. A., 1999, in Falcke H., Cotera A., Duschl W. J., Melia F., Rieke M. J., eds, ASP Conf. Ser. Vol. 186, The Central Parsecs of the Galaxy. Astron. Soc. Pac., San Francisco, p. 483
Rybakin B., Smirnov N., Goryachev V., 2016, in Voevodin V., Sobolev S., eds, Supercomputing: Second Russian Supercomputing Days. Communications in Computer and Information Science, Vol. 687. Springer International Publishing, Switzerland, p. 146
Ryu D., Jones T. W., Frank A., 2000, ApJ, 545, 475
Sahai R., Morris M. R., Claussen M. J., 2012a, ApJ, 751, 69
Sahai R., Güsten R., Morris M. R., 2012b, ApJ, 761, L21
Salim D. M., Federrath C., Kewley L. J., 2015, ApJ, 806, L36
Santos-Lima R., Lazarian A., de Gouveia Dal Pino E. M., Cho J., 2010, ApJ, 714, 442
Santos-Lima R., de Gouveia Dal Pino E. M., Lazarian A., 2012, ApJ, 747, 21

Santos-Lima R., de Gouveia Dal Pino E. M., Kowal G., Falceta-Gonçalves D., Lazarian A., Nakwacki M. S., 2014, ApJ, 781, 84
Saury E., Miville-Deschênes M.-A., Hennebelle P., Audit E., Schmidt W., 2014, A&A, 567, A16
Scalo J., Elmegreen B. G., 2004, ARA&A, 42, 275
Scannapieco E., 2017, ApJ, 837, 28
Scannapieco E., Brüggen M., 2015, ApJ, 805, 158
Schartmann M., Burkert A., Alig C., Gillessen S., Genzel R., Eisenhauer F., Fritz T. K., 2012, ApJ, 755, 155
Schartmann M. et al., 2015, ApJ, 811, 155
Schleicher D. R. G., Schober J., Federrath C., Bovino S., Schmidt W., 2013, New J. Phys., 15, 023017
Schneider E. E., Robertson B. E., 2017, ApJ, 834, 144
Schneider N. et al., 2012, A&A, 540, L11
Schneider N. et al., 2013, ApJ, 766, L17
Schneider N. et al., 2015, A&A, 575, A79
Schneider N. et al., 2016, A&A, 587, A74
Schober J., Schleicher D. R. G., Federrath C., Bovino S., Klessen R. S., 2015, Phys. Rev. E, 92, 023010
Sharp D. H., 1984, Phys. D Nonlinear Phenom., 12, 3
Shin M.-S., Stone J. M., Snyder G. F., 2008, ApJ, 680, 336
Shinn J.-H., Koo B.-C., Burton M. G., Lee H.-G., Moon D.-S., 2009, ApJ, 693, 1883
Shopbell P. L., Bland-Hawthorn J., 1998, ApJ, 493, 129
Shore S. N., LaRosa T. N., 1999, ApJ, 521, 587
Sofue Y., Handa T., 1984, Nature, 310, 568
Sofue Y., Kigure H., Shibata K., 2005, PASJ, 57, L39
Stevens I. R., Blondin J. M., Pollock A. M. T., 1992, ApJ, 386, 265
Stone J. M., Gardiner T., 2007, ApJ, 671, 1726
Stone J. M., Norman M. L., 1992, ApJ, 390, L17
Strickland D. K., Stevens I. R., 2000, MNRAS, 314, 511
Strickland D. K., Ponman T. J., Stevens I. R., 1997, A&A, 320, 378
Su M., Slatyer T. R., Finkbeiner D. P., 2010, ApJ, 724, 1044
Subramanian K., 1999, Phys. Rev. Lett., 83, 2957
Sutherland R. S., Bicknell G. V., 2007, ApJS, 173, 37
Thompson T. A., Quataert E., Zhang D., Weinberg D. H., 2016, MNRAS, 455, 1830
Tombesi F., Meléndez M., Veilleux S., Reeves J. N., González-Alfonso E., Reynolds C. S., 2015, Nature, 519, 436
Torii K., Enokiya R., Morris M. R., Hasegawa K., Kudo N., Fukui Y., 2014, ApJS, 213, 8
Tricco T. S., Price D. J., 2012, J. Comput. Phys., 231, 7214
van Loo S., Falle S. A. E. G., Hartquist T. W., Moore T. J. T., 2007, A&A, 471, 213
van Loo S., Falle S. A. E. G., Hartquist T. W., 2010, MNRAS, 406, 1260
Vazquez-Semadeni E., 1994, ApJ, 423, 681
Veilleux S., Cecil G., Bland-Hawthorn J., 2005, ARA&A, 43, 769
Veilleux S., Bolatto A., Tombesi F., Melendez M., Sturm E., Gonzalez-Alfonso E., Fischer J., Rupke D. S. N., 2017, ApJ, 843, 18
Vieser W., Hensler G., 2007, A&A, 472, 141
Vijayaraghavan R., Ricker P. M., 2015, MNRAS, 449, 2312
Vishniac E. T., 1994, ApJ, 428, 186
Wang B., 1995, ApJ, 444, 590
Warhaft Z., 2000, Annu. Rev. Fluid Mech., 32, 203
Weidl M. S., Jenko F., Teaca B., Schlickeiser R., 2015, ApJ, 811, 8
Williams J., 1999, in Franco J., Carraminana A., eds, Interstellar Turbulence. Cambridge Univ. Press, Cambridge, p. 190
Wolfire M. G., Tielens A. G. G. M., Hollenbach D., 1990, ApJ, 358, 116
Wright N. J., Drake J. J., Drew J. E., Guarcello M. G., Gutermuth R. A., Hora J. L., Kraemer K. E., 2012, ApJ, 746, L21
Xu J., Stone J. M., 1995, ApJ, 454, 172
Yamada M., Nishi R., 2001, ApJ, 547, 99
Yan H., Lazarian A., 2002, Phys. Rev. Lett., 89, 1102
Yirak K., Frank A., Cunningham A. J., 2010, ApJ, 722, 412
Yusef-Zadeh F., Morris M., Chance D., 1984, Nature, 310, 557
Yusef-Zadeh F., Hewitt J. W., Cotton W., 2004, ApJS, 155, 421
Zhang D., Thompson T. A., 2012, MNRAS, 424, 1170
Zhang D., Thompson T. A., Quataert E., Murray N., 2015, MNRAS, 468, 4801

APPENDIX A: EFFECTS OF NUMERICAL RESOLUTION

An important aspect to be investigated when studying wind–cloud systems numerically is the influence of the grid resolution on the results. A resolution study allows us to ascertain if the results are trustworthy and determine how affected they are by numerical diffusion (e.g. see Klein et al. 1994; Xu & Stone 1995; Nakamura et al. 2006; Niederhaus 2007; Yirak et al. 2010; Pittard & Parkin 2016 and sections 4.5 and 5.4 in Banda-Barragán 2016 for previous discussions on the effects of resolution upon wind–/shock–cloud/bubble systems). In this appendix, we investigate if the quantitative results presented in both Paper I and this paper hold for different numerical resolutions. This study is important because even when sophisticated solvers are utilized, capturing the physics of wind–cloud interactions greatly depends on the choice of numerical resolution (mesh spacing). In the models presented in our papers, care should be taken when selecting the resolution as the disruption of clouds occurs as a result of the growth of dynamically unstable perturbations (i.e. KH and RT instabilities). These perturbations grow at different length-scales, so the selected numerical resolution (i.e. the number of grid cells per cloud radius) for a particular simulation should ensure that the range of wavelengths at which these instabilities occur is sufficiently well resolved (see also Pittard & Parkin 2016).

To investigate the effects of the numerical resolution on the results presented in this series of papers, we perform two sets of numerical simulations: one for a model with a uniform cloud embedded in an oblique magnetic field (relevant for model MHD-Ob in Paper I and models UNI-0-0 and Uni-0-0 in this paper), and one for a model with a turbulent cloud that has a lognormal density distribution, a subsonic velocity field ($\mathcal{M}_{\rm w} = 0.33$), and a turbulent magnetic field with $[\beta_{\rm tu}] = 4$ (relevant for model Tur-Sub-Bwk). Figs A1 and A2 show the evolution of the diagnostics presented in Figs 5 and 9, and Figs 6, 7, 10, and 11, respectively, for filament (left-hand side column), tail (middle column), and footpoint (right-hand side column) material in model Uni-0-0. The plots in Fig. A1 indicate that all resolutions (R_{16-128}) capture the overall evolution of the morphological properties of filaments, except for the mean vorticity enhancement where the lowest resolution of R_{16} fails to properly capture small-scale vorticity in the interior of the cloud. Similarly, the plots in Fig. A2 indicate that resolutions $R_{\geq 32}$ capture the magnetic and kinematic properties of the uniform cloud. The transverse velocity dispersion, mean vorticity enhancement, and turbulent magnetic energy density exhibit the largest differences in this set of simulations (over different resolutions) as they depend on small-scale vorticity production. However, the differences between diagnostics at resolutions of R_{64} and R_{128} remain within $\sim$10 per cent up to $t/t_{\rm cc} = 1.0$, without trends with increasing resolution. Thus, if we consider all the diagnostics in Figs A1 and A2, we find that convergence occurs at resolutions of 64 cells per cloud radius, i.e. R_{64}, for this particular setup.

Figs A3 and A4 show the evolution of the diagnostics presented in Figs 5 and 9, and Figs 6, 7, 10, and 11, respectively, for filament (left-hand side column), tail (middle column), and footpoint (right-hand side column) material in the turbulent model, Tur-Sub-Bwk. Similarly to the above case, the plots of Fig. A3 show that convergence of the morphological properties in this model is achieved at a

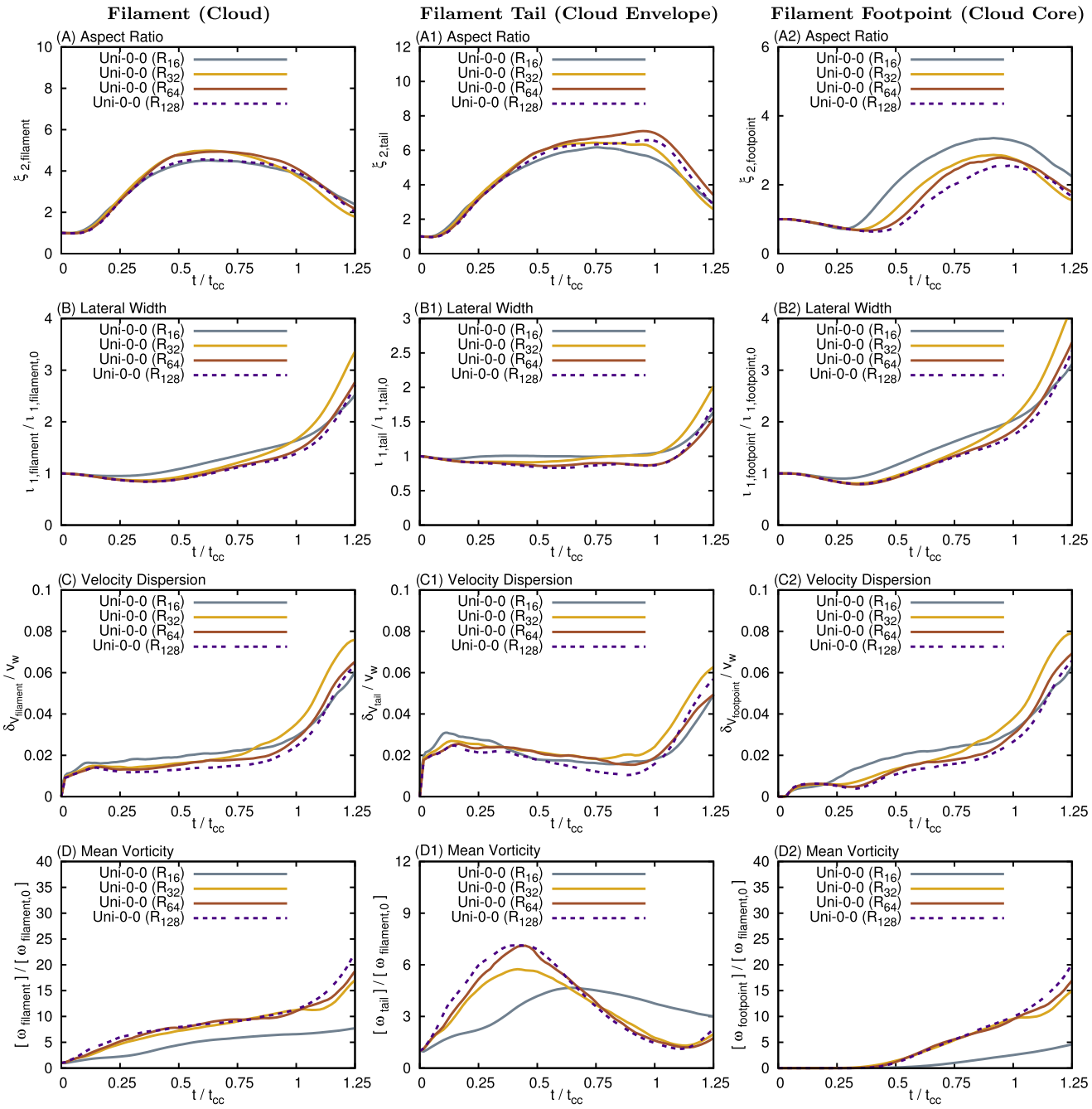

Figure A1. Time evolution of the diagnostics reported in Figs 5 and 9 in model Uni-0-0 at different resolutions (R_{16-128}).

resolution of R_{64}, except for the mean vorticity enhancement, which grows with increasing resolution. The reason for this behaviour is that low-resolution setups do not capture properly the turbulent density, velocity, and magnetic fields in the initial cloud. Thus, as we increase the grid resolution, we also capture more details of the original turbulent distributions and diagnostics that strongly depend on them, such as the vorticity. The plots of Fig. A4 show similar results for R_{64} and R_{128}, with the magnetic and kinematic properties converging to within 10 per cent up to $t/t_{cc} = 1.0$, with the exception of the turbulent magnetic energy, which also shows a mild growth trend with increasing resolutions. Overall, if we consider all the diagnostics in Figs A3 and A4, we find that convergence in turbulent cloud models also occurs at resolutions of 64 cells per cloud radius, i.e. R_{64}, except for the mean vorticity enhancement and the turbulent magnetic energy density. Thus, we conclude that the resolutions utilized for the models presented in both Paper I and this paper, i.e. R_{64} and R_{128} for setups with M and S configurations, respectively, are adequate to capture the morphological properties, energetics, and dynamics of wind-swept uniform and turbulent clouds.

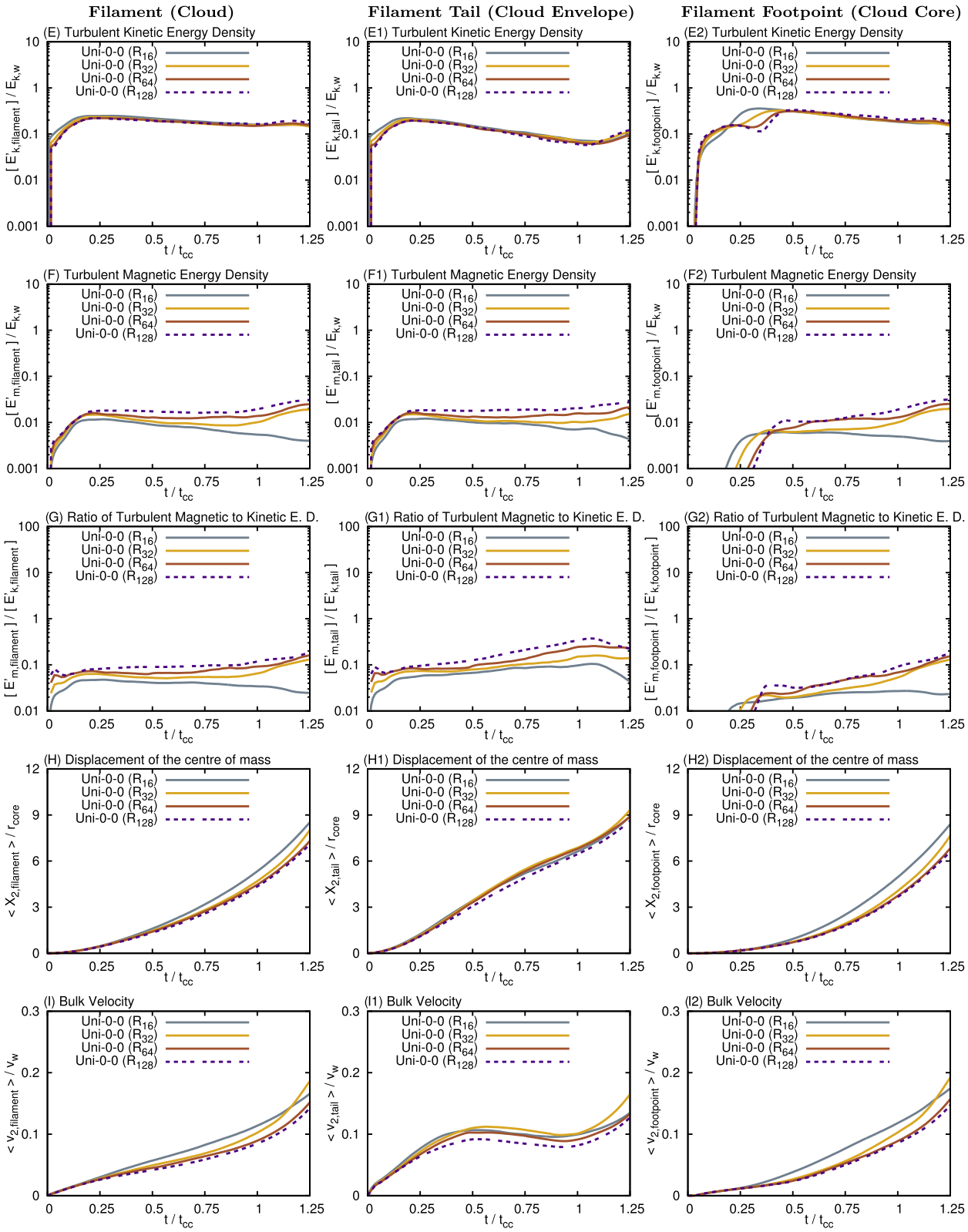

Figure A2. Time evolution of the diagnostics reported in Figs 6, 7, 10, and 11 in model Uni-0-0 at different resolutions (R_{16-128}).

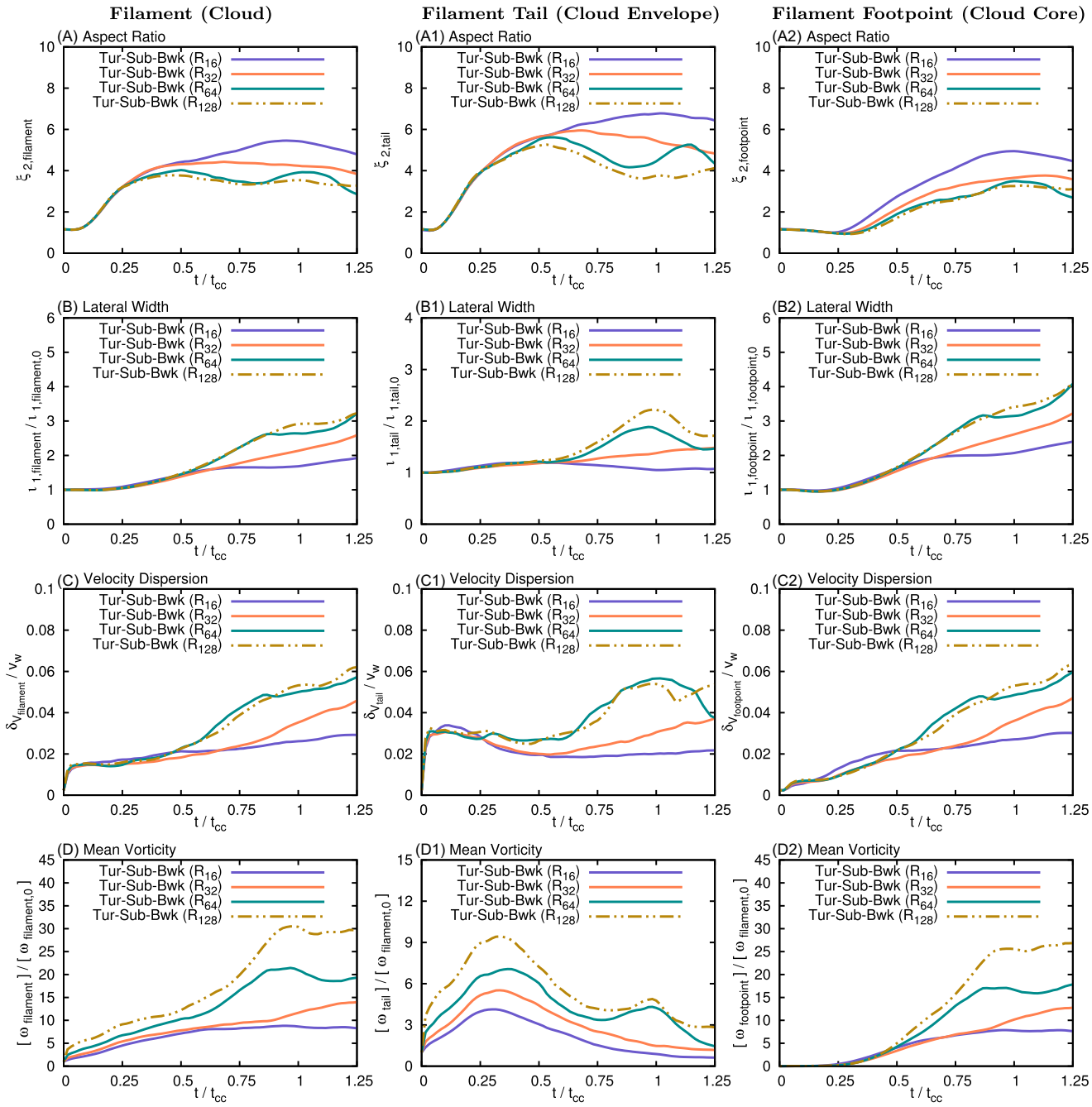

Figure A3. Time evolution of the diagnostics reported in Figs 5 and 9 in model Tur-Sub-Bwk at different resolutions (R_{16-128}).

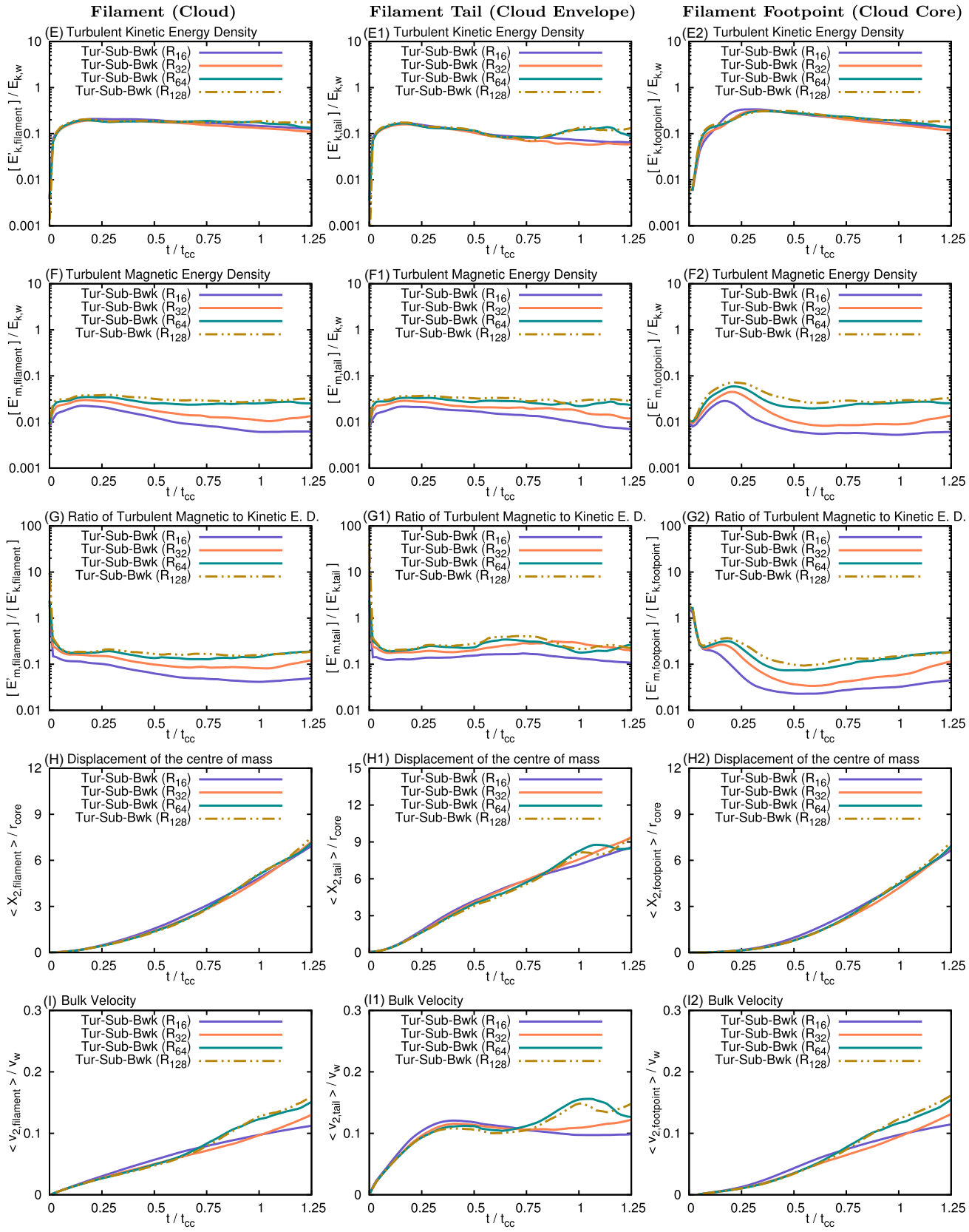

Figure A4. Time evolution of the diagnostics reported in Figs 6, 7, 10, and 11 in model Tur-Sub-Bwk at different resolutions (R_{16-128}).

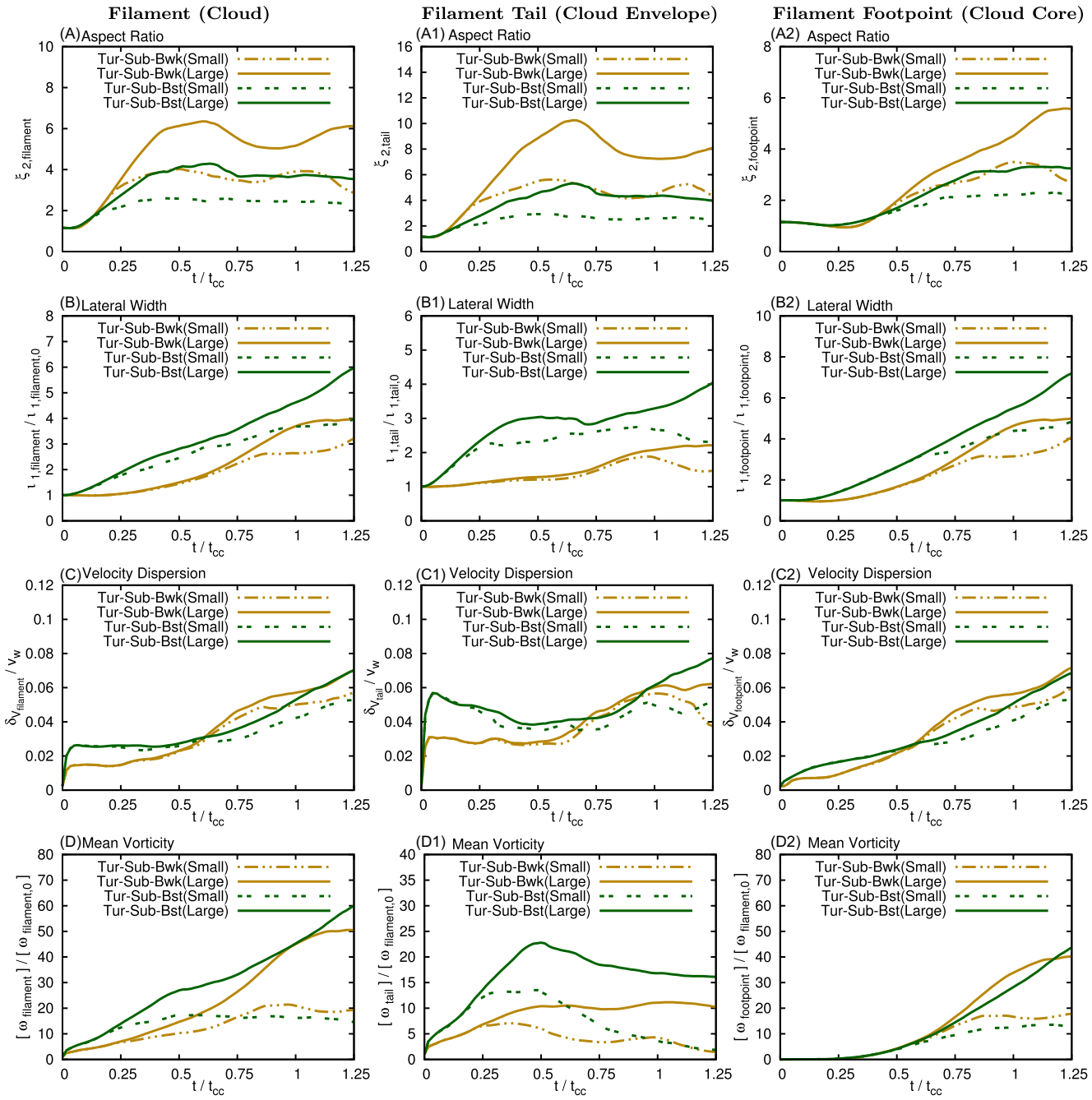

Figure B1. Time evolution of the diagnostics reported in Figs 5 and 9 in two models, Tur-Sub-Bwk and Tur-Sub-Bst, at the same resolution (R_{64}), but different computational domain sizes (S and L configurations).

APPENDIX B: LARGER DOMAIN SIMULATIONS

In this appendix, we discuss the effects of the simulation domain size on the diagnostics presented through this manuscript. In a similar manner to Paper I, we compare two sets of simulations with the same initial conditions (to those of models Tur-Sub-Bwk and Tur-Sub-Bst), the same numerical resolutions of 64 cells per cloud radius (i.e. R_{64}), and different domain sizes (large or L configuration and small or S configuration). The computational domain in models Tur-Sub-Bwk(Large) and Tur-Sub-Bst(Large) is twice the size of the domain in models Tur-Sub-Bwk(Small) and Tur-Sub-Bst(Small), and it covers the spatial range: $-4\,r_c \leq X_1 \leq 4\,r_c$, $-2\,r_c \leq X_2 \leq 22\,r_c$, and $-4\,r_c \leq X_3 \leq 4\,r_c$, where r_c is the radius of the cloud.

Fig. B1 shows the evolution of the parameters presented in Figs 5 and 9 in Section 4 for filament (left-hand side column), tail (middle column), and footpoint (right-hand side column) material, in both models, Tur-Sub-Bwk and Tur-Sub-Bst. The panels of Fig. B1 indicate that the aspect ratio and the mean vorticity enhancement are

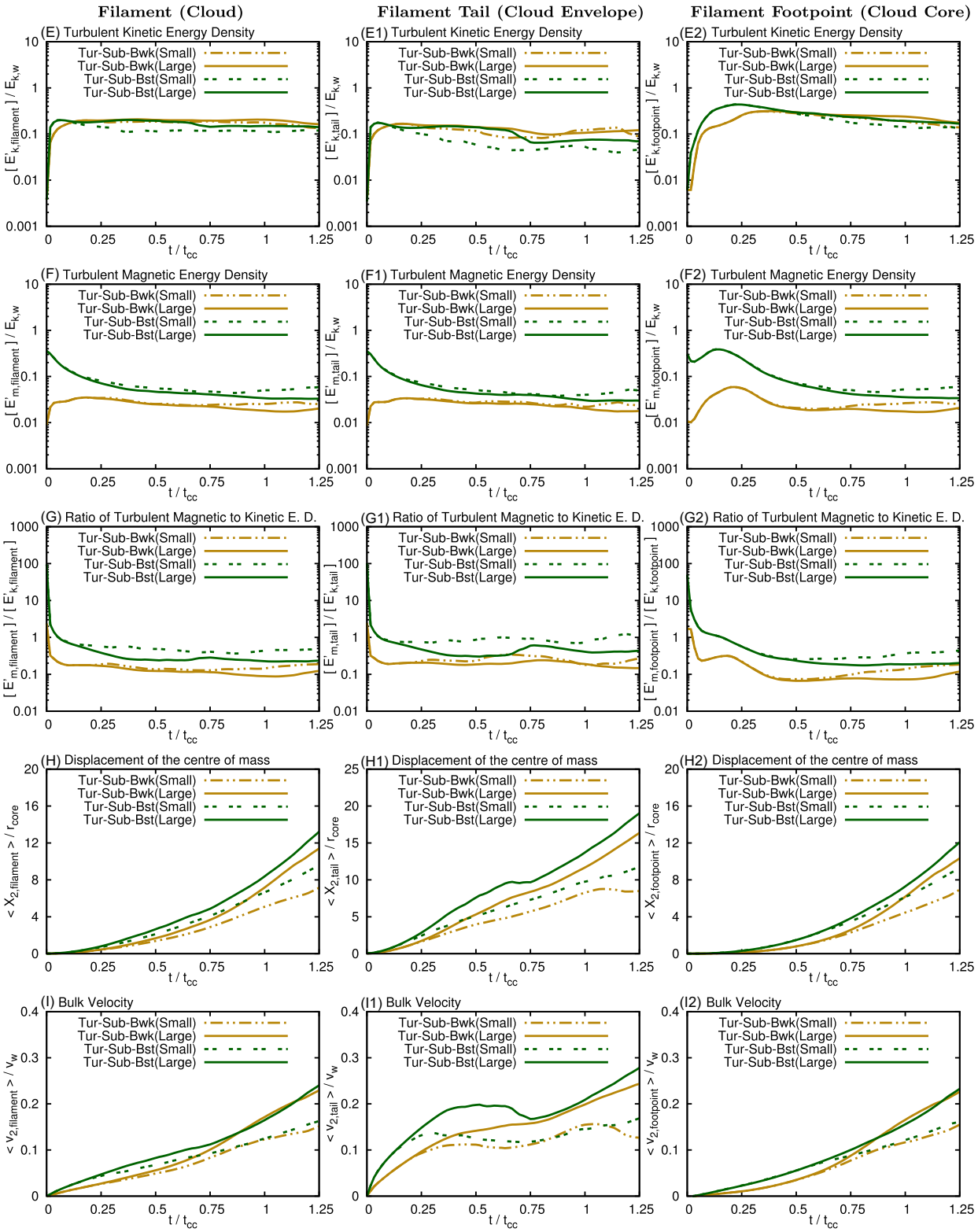

Figure B2. Time evolution of the diagnostics reported in Figs 6, 7, 10, and 11 in two models, Tur-Sub-Bwk and Tur-Sub-Bst, at the same resolution (R_{64}), but different computational domain sizes (S and L configurations).

underestimated in the small-domain simulation, with differences being as large as ∼80 per cent and ∼150 per cent, respectively. The curves in these plots start to diverge when material starts to flow out of the smaller simulation grid, either through the back or the sides of the computational domain. Thus, tail material is affected the most by the choice of domain size as it is the first to be stripped off the cloud by the wind ram pressure and dynamical instabilities. Indeed, divergence of the aspect ratio and the mean vorticity

enhancement in tail material starts at $t/t_{cc} \sim 0.25$ in both models, mainly due to fast, low-density material leaving the domain through the back surface of the domain. In the case of footpoint material, on the other hand, divergence of the aspect ratio and the mean vorticity enhancement only starts to occur at $t/t_{cc} \sim 0.5$–0.6 in both models, due to material leaving through both the back (at $t/t_{cc} \sim 0.5$) and the sides of the domain (at $t/t_{cc} \sim 0.6$). The other two parameters in Fig. B1, i.e. the lateral width and velocity dispersion, are not as affected and errors remain below ∼25 per cent in both models until $t/t_{cc} \sim 1.0$.

Fig. B2 shows the evolution of the parameters presented in Figs 6, 7, 10, and 11 in Section 4 for filament (left-hand side column), tail (middle column), and footpoint (right-hand side column) material, in models Tur-Sub-Bwk and Tur-Sub-Bst. Overall, the trends of the curves presented in this figures are the same, implying that our conclusions with respect to the energetics and dynamics of wind-swept clouds are independent of the computational simulation size. Tail diagnostics are again more affected by the domain size than footpoint diagnostics because tail material leaves the smaller simulation domain earlier. The tail parameters that are most affected by the size of the simulation domain are those related to the kinetic and kinematic properties of the filaments, such as the turbulent kinetic energy density, the displacement of the centre of mass, and the bulk speeds. Differences between large- and small-domain simulations are as large as ∼60 per cent, ∼40 per cent, and 50 per cent in both models for each of these parameters, respectively, up to $t/t_{cc} = 1.0$. In the case of footpoint material, errors are lower and remain below ∼25 per cent for all parameters in both models over the same time-scale.

Another aspect that we highlight here is that smaller domain simulations bias the results towards gas with lower kinetic energy densities and slightly higher magnetic energy densities than larger domain simulations, thus favouring higher ratios of the two turbulent energy densities. This indicates that the actual ratios of turbulent magnetic to kinetic energy densities in the wind–cloud systems studied in this paper are more likely to be on the lower end of the range reported in Section 4.2.3, i.e. $[E'_{m,filament}]/[E'_{k,filament}] \sim 0.1$–$0.4$. In a similar manner, we observe that both the displacement of the centre of mass and the bulk speeds are underestimated in smaller domain simulations. Consequently, the values reported in Section 4.2.4 for these parameters, at $t/t_{cc} = 1.0$, should be regarded as reference lower limits of the travelled distances and bulk velocities of filaments, which are more accurately measured in the larger domain simulations discussed in Section 4.1.4. Therefore, if more precise measurements of these global diagnostics are required (especially after the break-up time), future numerical work on wind–cloud systems should consider computational domains with sizes similar to the M or L configurations discussed in this paper.

Finally, an important remark to make based on the analysis presented in this appendix is that even though we find that the choice of computational domain sizes does have an effect on the evolution of our diagnostics, when we compare different models with the same resolution and domain configuration, we find the same qualitative and quantitative results previously discussed in Section 4. Moreover, the errors are expected to be much lower when the M configuration is utilized as in our self-consistent models UNI-0-0, TUR-SUP-BST, and TUR-SUP-BST-ISO. Thus, we conclude that our domain configurations M and S are adequate for the purpose of comparing different models to one another and also for extracting reliable qualitative and quantitative information from the simulations.

APPENDIX C: PDF OF TURBULENT DENSITIES

In this appendix. we present the evolution of the PDF of the mass density of the cloud/filament in model Tur-0-0 (see Fig. C1). The initial density distribution of the turbulent cloud in this model (and in all the other models with turbulent clouds, i.e. TUR-SUP-BST, TUR-SUP-BST-ISO, Tur-Sub-0, Tur-Sup-0, Tur-Sub-Bwk, and Tur-Sub-Bst) has the following mathematical form:

$$\mathcal{P}(\rho) = \frac{1}{s\sqrt{2\pi}} e^{-\frac{[\ln(\rho)-m]^2}{2s^2}}, \tag{C1}$$

where ρ is the mass density, and m and s are the mean and standard deviation of the natural logarithm of the ISM density field. Accordingly, the mean and variance of the ISM density field are

$$\nu = e^{(m+\frac{s^2}{2})}, \text{ and} \tag{C2}$$

$$\sigma^2 = \nu^2(e^{s^2} - 1), \tag{C3}$$

respectively (see appendices A and B in Sutherland & Bicknell 2007). Fig. C1 shows the density PDF of cloud gas taken from snapshots of model Tur-0-0 at different instances of its evolution (i.e. for $0 \leq t/t_{cc} \leq 1.25$). Three effects are seen in these curves: (i) at the beginning of the interaction the cloud is compressed by wind-driven shocks, thus increasing the variance of the density PDF (see the curve at $t/t_{cc} = 0.25$). Then, (ii) the formation of the filamentary tail by mass stripping, causes cloud and wind gas to mix, thereby causing the cloud density to steadily decrease and the PDF to become skewed towards low-density values (see the high- and low-density ends of curves, respectively, for $t/t_{cc} \geq 0.5$). As time progresses, (iii) the low-density tail in the PDF also starts to flatten as cloud gas is continuously mixed with ambient gas and as the filament is eroded by dynamical instabilities. A complete analysis of the evolution of PDFs of wind-swept turbulent clouds will be the topic of a future paper.

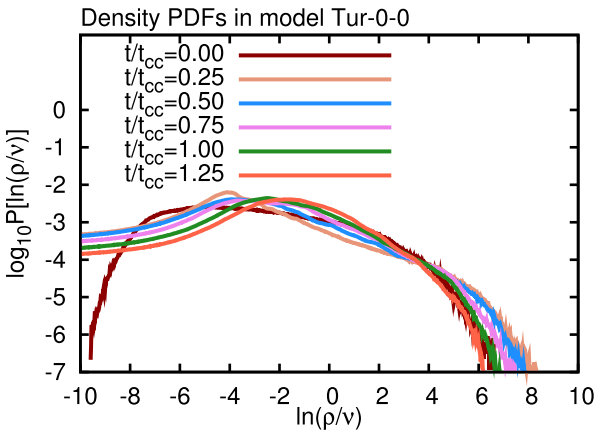

Figure C1. Evolution of the gas density PDF in the turbulent cloud of model Tur-0-0 normalized with respect to the mean density, for $0 \leq t/t_{cc} \leq 1.25$. The initial density field ($t/t_{cc} = 0$) is taken from Federrath & Klessen 2012, representing typical physical conditions of ISM turbulent clouds. An initial compression phase ($t/t_{cc} \sim 0.25$) makes the cloud gas denser at the beginning of the interaction, but mass stripping ($t/t_{cc} \geq 0.5$) and mixing of cloud material with ambient gas make the density decrease and create a heavy and flat tail on the low-density end of the PDF.

APPENDIX D: DIVERGENCE CLEANING ALGORITHM

In this appendix, we provide additional details on the method utilized to pre-process the initial, turbulent magnetic fields in models TUR-SUP-BST, TUR-SUP-BST-ISO, Tur-Sub-Bwk, and Tur-Sub-Bst, so that they comply with the solenoidal condition. As stated in Section 3.2, a direct interpolation of the magnetic field components taken from the simulation of turbulent flows (reported in Federrath & Klessen 2012) into our simulation grids is not possible because the interpolated fields would contain magnetic monopoles at the cloud boundaries. To solve this issue and initialize models TUR-SUP-BST, TUR-SUP-BST-ISO, Tur-Sub-Bwk, and Tur-Sub-Bst with solenoidal magnetic fields, we first clean the divergence errors in them by following the steps below:

(i) The magnetic field components are extracted from a data cube of simulation 21 in Federrath & Klessen (2012).

(ii) These components are then scaled to the desired turbulent plasma beta, [$\beta_{\rm tu}$], for each model and subsequently interpolated into simulation grids with the same resolution of the grids described in Section 3. The resulting magnetic field in each model is then the sum of a uniform oblique field, $\boldsymbol{B}_{\rm ob}$, plus the turbulent field, $\boldsymbol{B}_{\rm tu}$ (see Section 3 for further details).

(iii) The interpolated magnetic fields violate the free-divergence constraint at the boundaries of the cloud, so we clean the divergence errors by using a mixed hyperbolic/parabolic correction technique by Dedner et al. (2002) that introduces a generalized Lagrange multiplier (ψ; hereafter GLM) to couple the divergence constraint, $\boldsymbol{\nabla\cdot B}$, with the MHD conservation laws (see equations 1–4). The induction equation (see equation 4) is then replaced by:

$$\frac{\partial \boldsymbol{B}}{\partial t} + \boldsymbol{\nabla\cdot}(\boldsymbol{vB} - \boldsymbol{Bv}) + \nabla\psi = 0, \tag{D1}$$

while the solenoidal constraint reads:

$$\frac{\partial \psi}{\partial t} + c_{\rm h}^2\, \boldsymbol{\nabla\cdot B} = -\frac{c_{\rm h}^2}{c_{\rm p}^2}\psi, \tag{D2}$$

where $c_{\rm h} = C_{\rm a}\Delta h/\Delta t^n$ is the maximum admissible speed at which divergence errors propagate given the time-step restriction, $c_{\rm p}^2 = \Delta h c_{\rm h}/\alpha$ is a diffusion coefficient, $\Delta h = \min(\Delta X_{\rm j})$ is the minimum cell length, Δt^n is the time increment, and $\alpha = 0.2$ is a dimensionless parameter controlling the optimal rate at which monopoles are damped (see Mignone & Tzeferacos 2010 and Mignone, Tzeferacos & Bodo 2010 for details of the implementation in Godunov-type schemes and high-order schemes, respectively).

(iv) This formulation reconfigures the original magnetic field at wind–cloud interfaces and enforces the zero-divergence condition by transporting the divergence errors towards the domain boundaries and damping the existing magnetic monopoles (Dedner et al. 2002).

(v) We save the components of the divergence-free magnetic fields once the solutions are stable and the divergence errors (Mignone & Tzeferacos 2010),

$$L_1(Q) = \frac{1}{N_{\rm X_1} N_{\rm X_2} N_{\rm X_3}} \Sigma_{\rm i,j,k} |Q_{\rm i,j,k} - Q^{\rm ref}_{\rm i,j,k}|, \tag{D3}$$

where $Q_{\rm i,j,k} = \Delta h|\,\boldsymbol{\nabla\cdot B}|_{\rm i,j,k}/|\boldsymbol{B}|_{\rm i,j,k}$, are below $\sim 10^{-4}$ in models TUR-SUP-BST, TUR-SUP-BST-ISO, Tur-Sub-Bwk, and Tur-Sub-Bst (see e.g. Fig. D1). The divergence errors at these stages are sufficiently small not to cause disturbances in the density and magnetic fields of the simulations. It is necessary to add a parameter $\eta = 0.1$ of the maximum magnetic field ($|\boldsymbol{B}_{\rm max}|$) in the denominator of equation D3 to avoid undefined divisions by zero or the appearance of artificially high values when $|\boldsymbol{B}|_{\rm i,j,k}$ is small. Tricco & Price (2012) followed a similar approach when testing a divergence cleaning algorithm in smoothed-particle magnetohydrodynamics. The main advantage of following this divergence-cleaning process on the magnetic field of the cloud is that the initial magnetic configuration does not contain sheaths of high magnetic tension around the cloud as it would in cases where the cloud magnetic field is merely truncated at the edge of it. This assures a smooth transition from the ambient magnetic field into the cloud magnetic field in the initial conditions (see e.g. the 3D streamline plot at $t/t_{\rm cc} = 0$ of the magnetic field of model MHD-Tu-S in Panel C of fig. 7.6 in Banda-Barragán 2016).

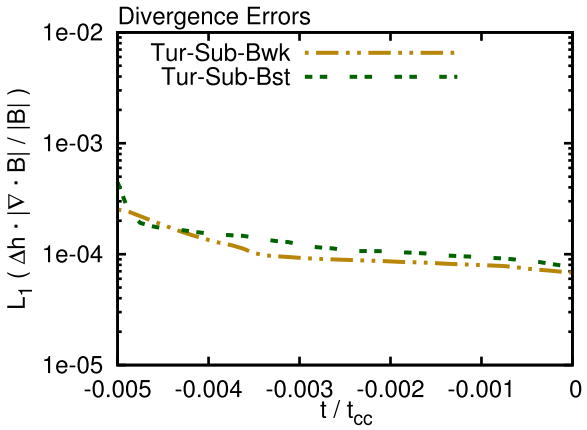

Figure D1. Cleaning of divergence errors in the initial magnetic fields for models Tur-Sub-Bwk (double-dot–dashed line) and Tur-Sub-Bst (two-dashed line; same as for models TUR-SUP-BST and TUR-SUP-BST-ISO). The time on the X-axis is in units of the cloud-crushing time, $t_{\rm cc}$, and it is negative as it corresponds to the pre-processing phase of the magnetic fields, i.e. before the simulations of these models are started and updated with the MHD formulation of Section 3.

(vi) The new solenoidal magnetic fields are interpolated into the grids of models TUR-SUP-BST, TUR-SUP-BST-ISO, Tur-Sub-Bwk, and Tur-Sub-Bst, and then the MHD wind–cloud simulations of these models are initialized with the constrained transport formulation described in Section 3.1.

APPENDIX E: MAGNETIC ENERGY ENHANCEMENT

In this appendix, we show the evolution of the magnetic energy enhancement in nine models with the M and S configurations discussed in Sections 4.1 and 4.2 (see Fig. E1). The ratio of filament to initial cloud magnetic energy or the variation of the magnetic energy contained in filament material at a specific time, t, is calculated by the following equation

$$\Delta E_{M_\alpha} = \frac{E_{M_\alpha} - E_{M_{\alpha,0}}}{E_{M_{\alpha,0}}}, \tag{E1}$$

where $E_{M_\alpha} = \int \frac{1}{2}\, C_\alpha\, |\boldsymbol{B}|^2 {\rm d}V$ is the total magnetic energy in cloud/filament material, $E_{M_{\alpha,0}}$ is the initial magnetic energy in the cloud, and α refers to filament, footpoint, or envelope material (see Section 3 for further details). The evolution of this parameter in Fig. E1 shows two effects. First, the stronger the initial magnetic field in the cloud, the faster its growth reaches saturation. In fact, in models without turbulent magnetic fields (UNI-0-0,

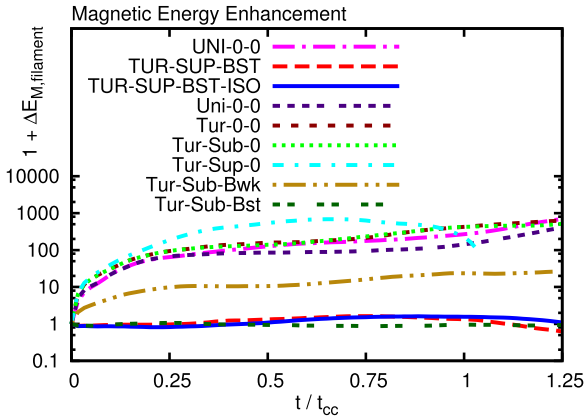

Figure E1. Time evolution of the magnetic energy enhancement in the filaments of nine models with the M and S configurations, namely models UNI-0-0 (dash–dotted line), TUR-SUP-BST (dashed line), TUR-SUP-BST-ISO (solid line), Uni-0-0 (four-dashed line), Tur-0-0 (long-dashed line), Tur-Sub-0 (dotted line), Tur-Sup-0 (short dash–dotted line), Tur-Sub-Bwk (long-dash-two-dotted line), and Tur-Sub-Bst (two-dashed line).

Uni-0-0, Tur-0-0, Tur-Sub-0, and Tur-Sup-0), the magnetic energy grows by a factors of $\Delta E_{\mathrm{M_{filament}}} \sim 100$–$1000$, while in the turbulent scenarios it only grows by factors of $\Delta E_{\mathrm{M_{filament}}} \sim 10$ (in the weak-field case: Tur-Sub-Bwk) or it is already saturated from $t/t_{\mathrm{cc}} = 0$ (in the strong-field cases: TUR-SUP-BST, TUR-SUP-BST-ISO, and Tur-Sub-Bst). Second, the ratio of magnetic energy (and magnetic field strength) in the filament to that in the initial cloud remains nearly constant $\sim$1 throughout the simulations (provided that self-consistent, strong, turbulent magnetic fields are added to the clouds). This has important implications for astrophysical filaments as it indicates that filaments have the same magnetic field strength as their progenitor clouds.

APPENDIX F: MIXING FRACTION

In this appendix, we show the evolution of the mixing fraction in the models with the S configuration discussed in Section 4.2 (see Fig. F1). The degree (percentage) of mixing between cloud and wind gas is calculated by the following equation

$$f_{\mathrm{mix}_\alpha} = \frac{\int \rho C^*_\alpha \mathrm{d}V}{M_{\mathrm{cl},0}} \times 100 \text{ per cent}, \tag{F1}$$

where the numerator is the mass of mixed gas, with $0.1 \leq C^*_\alpha \leq 0.9$ tracking material in mixed cells, and $M_{\mathrm{cl},0}$ represents the mass of the cloud at time $t/t_{\mathrm{cc}} = 0$. The evolution of this parameter in both the tail (top panel of Fig. F1) and footpoint (bottom panel of Fig. F1) of filaments shows the protective effects of strong, turbulent magnetic fields. Magnetic shielding grows as we increase the initial tension of the turbulent magnetic field and this prevents the mixing of cloud/filament and wind gas as it suppresses KH instabilities at fluid interfaces. As a result, the mixing fractions in models Tur-Sub-Bwk and Tur-Sub-Bst become lower than in its counterparts as the simulations progress.

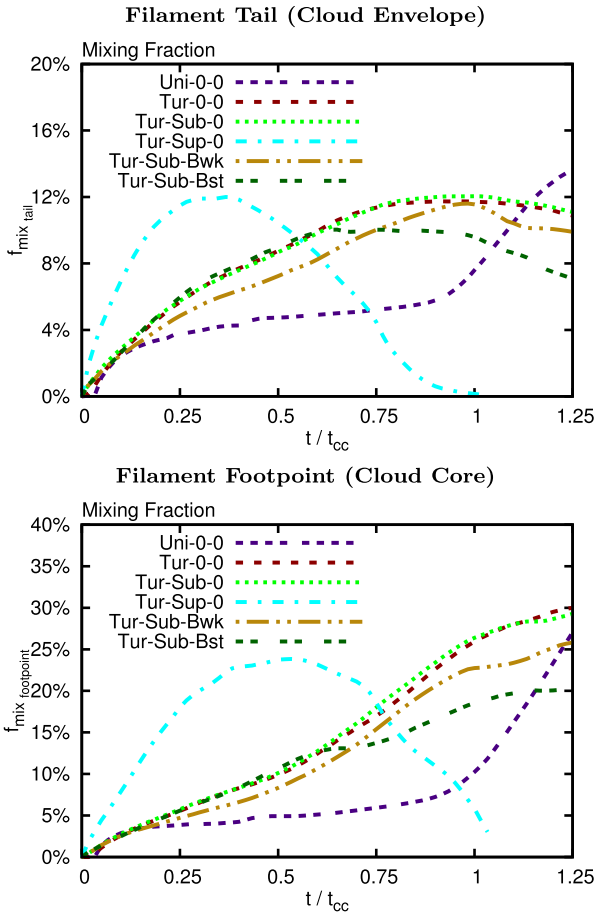

Figure F1. Time evolution of the mixing fractions in the tails (top panel) and footpoints (bottom panel) of filaments in six models with the S configuration, namely models Uni-0-0 (four-dashed line), Tur-0-0 (long-dashed line), Tur-Sub-0 (dotted line), Tur-Sup-0 (short dash–dotted line), Tur-Sub-Bwk (long-dash-two-dotted line), and Tur-Sub-Bst (two-dashed line).

APPENDIX G: CLUMPING FACTOR

In this appendix, we show the evolution of the clumping factor in the models with the S configuration discussed in Section 4.2 (see Fig. G1). The clumping factor of the wind-swept clouds in these models is calculated as follows:

$$\mathrm{c}_\alpha = \frac{[\rho_\alpha^2]}{[\rho_\alpha]^2}, \tag{G1}$$

where the volume-averaged quantities are calculated for cloud material (i.e. for α=cloud/filament) using equation (16). Note that if $\mathrm{c}_\alpha = 1.0$, the cloud has a constant density (i.e. it is not clumpy), while higher values of c_α indicate larger density variations within the cloud (i.e. it is more clumpy). The evolution of this parameter shows that including turbulent magnetic fields (see the evolution of models Tur-Sub-Bwk and Tur-Sub-Bst) favours the clumping of cloud material into dense knots (cloudlets) and subfilaments, which are able to survive for long times. This is in agreement with our

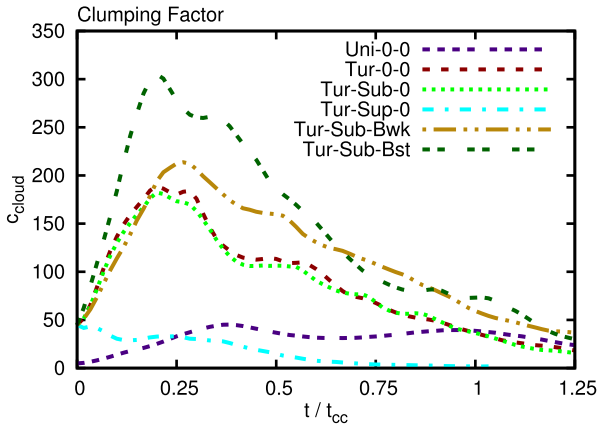

Figure G1. Time evolution of the clumping factor in six models with the S configuration, namely models Uni-0-0 (four-dashed line), Tur-0-0 (long-dashed line), Tur-Sub-0 (dotted line), Tur-Sup-0 (short dash–dotted line), Tur-Sub-Bwk (long-dash-two-dotted line), and Tur-Sub-Bst (two-dashed line).

discussion in the main body of the paper and in Appendix F, and it also confirms the key role of magnetic fields in preventing cloud destruction and facilitating its entrainment into the hot wind.

This paper has been typeset from a TEX/LATEX file prepared by the author.